ABSTRACT

Title of Dissertation:	INTERFACE AND STRUCTURES IN LITHIUM-GARNET QUASI-SOLID-STATE BATTERIES
	Jack Evans Gritton III, Doctor of Philosophy in Materials Science and Engineering, 2024
Dissertation directed by:	Professor Eric D Wachsman, Materials Science and Engineering Department

A confluence of adoption of the internet of things, mobile electronics, electric vehicles, and shift towards adoption of intermittent green energy sources has led to a need for rapid improvement in battery technology in metrics ranging from rate capability and energy density to safety. While significant strides have been made through traditional liquid-based lithium-ion batteries, these oft-conflicting demands require fundamental shifts in battery chemistry, especially enabling safe incorporation of lithium metal anodes. Given their high conductivity, non-flammability, wide electrochemical stability window, and stability to lithium metal, lithium-stuffed garnets of the family LLZO provide one of the most promising alternative electrolytes to replace traditional flammable electrolytes. Two of the largest factors holding back these ceramic electrolytes are interfacial compatibilities and the interplay between processing and electrolyte mass.

While drastic improvements have been made in the interface between garnet and lithium metal to improve rate capability, similar jumps in full cells have not been observed for rate and capacity. Using a varied cathode loading and a combination of EIS and DRT, we showed that garnet-catholyte interface was the main contributor to resistance in quasi-solid-state batteries of reasonable cathode loadings utilizing Pyr_{14}TFSI based catholyte. Two methods were then used to improve this interface: modification of the garnet structure interfacing with catholyte, and modification of catholyte composition. Through the use of these methods, rate capabilities and capacity were drastically improved from the baseline system, both at elevated and room temperature.

In addition to reducing interfacial resistance, cell polarization can be reduced through using thinner electrolytes. Given its higher mass density and lower conductivity in comparison to liquid electrolytes, garnet has historically had to rely on its greater stability to higher energy density electrodes to maintain competitive energy densities or utilize thin-film procedures that reduce mass but result in orders of magnitude lower conductivity than bulk produced garnets. To balance conductivity, ease of processing, and cell mass, a new combination of bulk-derived processing has been developed that allows for thin free-standing cubic garnet and thin, flexible, porous garnet. Cells using these new thin garnets achieved high cycling rates, and significant capacities.

INTERFACE AND STRUCTRURES IN LITHIUM-GARNET QUASI-SOLID-STATE BATTERIES

by

Jack Evans Gritton III

Dissertation submitted to the Faculty of the Graduate School of the
University of Maryland, College Park, in partial fulfillment
of the requirements for the degree of
Doctor of Philosophy
2024

Advisory Committee:
Professor Eric D. Wachsman, Chair
Professor Paul Albertus
Professor Shenqiang Ren
Professor Yifei Mo
Professor Chunsheng Wang, Dean's Representative

Acknowledgements

I would like to thank my advisor, Professor Eric Wachsman, for guidance during my time as a PhD student. I have learned so very much from you and in my time working in your laboratory.

I would like to thank Dennis McOwen and Yi-Lin Huang for their mentorship, and guidance in my research.

Thank you to my committee members for your time and input on my dissertation: Dr Paul Albertus, Dr Yifei Mo, Dr Shenqiang Ren, and Dr Chunsheng Wang.

For their help and collaboration, I thank other current and past members of Dr Wachsman's group: Ian Robinson, Sam Horlick, Patrick Stanley, Matthew Limpert, Tanner Haman, Griffin Godbey, Zhezhen Fu, Gibson Scisco, George Alexander, William Schubert, and all the others I have worked with in Dr Wachsman's group. Similarly, I would like to thank Dr Jan Allen, Dr Dat Tran, Dr Liangbing Hu, and Dr Venkataraman Thangadurai for collaborations with their groups.

For their help in my research, I would like to thank the undergraduate and high school students: Tyler Rae, Felix Forcho, and Jason Hsu.

I would also like to thank Amit Naskar, all those I worked with previously in the Carbon and Composites group at ORNL, and Sachin Nibalkar for their encouragement in pursuing this degree and mentorship.

I would especially like to thank my family and friends, both back home and those in the DMV area. I would particularly like to thank my parents Jack and Judy, as well as my sister Kallie and brother-in-law Chris. Thank you for all of the love and

support you've given over the years. I wouldn't have made it here without you, and especially your forbearance for all my science experiments when I was younger. Neil, Rebecca, Bo, Anderson, and Laine Chatterjee, thank you for making me feel like I was at home in the DMV and all of the time with your wonderful family. Thank you to Cougar Garcia, Megan Kimicata, Michael Parente, Brad Allen, Jim Carpenter, John Lewis, Aaron Lewis, Tim and Priya Kohler, Quinn and Kayla Matthew, Adam Zander, Alex Contreras, Dan and Katie Antinori, Greg Hitz, Heather Delbridge, Tucker Plunkett, Kelsey Naish, Ryan Wendt, Seth Naish, and Ryan Stroh.

Table of Contents

List of Tables

List of Figures

List of Abbreviations

ACN - Acetonitrile

ALD – Atomic Layer Deposition

BBP – Benzyl Butyl Phthalate

BTFE - Bis(2,2,2-trifluoroethyl) ether

CAI – Cathode Aluminum Interface

CAM – Cathode Active Material

CEI – Cathode Electrolyte Interface

CV – Cyclic Voltammetry

DEC – Diethyl Carbonate

DSC – Differential Scanning Calorimetry

DRT – Distribution of Relaxation Times

EC – Ethylene Carbonate

EDS – Energy Dispersive X-Ray Spectroscopy

EIS – Electrochemical Impedance Spectroscopy

EMC – Ethyl Methyl Carbonate

HOMO – Highest Occupied Molecular Orbital

IL – ionic liquid

LATP – Lithium Aluminum Titanium Phosphate

LCO – Lithium Cobalt Oxide $LiCoO_2$

LFP – Lithium Iron Phosphate $LiFePO_4$

LGLZ – Gallium-doped LLZ

LGPZC - $Li_{6.4}Ga_{0.2}Pr_3Zr_{1.8}Ce_{0.2}O_{12}$

LGPZN - $Li_{6.4}Ga_{0.2}Pr_3Zr_{1.8}Nb_{0.2}O_{12}$

LiFSI – Lithium bis(fluorosulfonyl)imide

LiPAA – Lithium PolyAcrylate

$LiPF_6$ – Lithium Hexafluorophosphate

LiPON – Lithium Phosphorous Oxynitride

LiTFSI – Lithium bis(trifluoromethanesulfonyl)imide

LLCZT – Calcium, Tantalum co-doped LLZ

LLTO – Lithium Lanthanum Titanium Oxide

LLZ –Lithium stuffed garnet of the family $Li_7La_3Zr_2O_{12}$

LLZT – Tantalum -doped LLZ

LTO – Lithium Titanium Oxide

LUMO – Lowest Unoccupied Molecular Orbital

MIEC – Mixed Ionic Electronic Conductor

NMC – Lithium Nickel Manganese Cobalt Oxide $LiNi_xMn_yCo_zO_2$

NMCr - $Li_{1.075}Ni_{0.35}Mn_{1.5}Cr_{0.075}O_4$

OFPTFE - 1H,1H,5H,5H-octafluoropethyl 1,1,2,2-tetraflyoroethyl ether

PAG – Poly Alkyl Glycols

PC – Propylene Carbonate

PLD – Pulsed Laser Deposition

PVB – Poly Vinyl Butyrol

PVDF – Polyvylidene fluoride

rtIL – room temperature ionic liquid

SEM – Scanning Electron Microscopy

SEI – Solid Electrolyte Interphase

SLEI – Solid-Liquid-Electrolyte Interface

TEP – Triethyl Phosphate

$TFSI^-$ - bis(trifluoromethanesulfonyl)imide

TGA – Thermogravimetric analysis

TTFETFE - 1,1,2,2-Tetrafluoroethyl 2,2,2-trifluoroethyl ether

XRD – X-ray Diffraction

Chapter 1: Introduction and Background

1.1 Motivation

Demand to reduce green-house gas emissions to combat climate change has become an increasingly important topic. The largest contributor to these emissions is the burning of fossil-fuel for energy needs. In the United States emissions from burning fossil fuels for only the transportation sector exceeds 25% of the nation's total emissions, with a majority of electricity generation, industrial, commercial, and residential sectors emissions also attributable to fossil fuels[2]. Various forms of renewable energy sources have seen increasing adoption in recent years to reduce these emissions from electricity generation. In fact, renewable energy output in the Unites States more than doubled between 2000 to 2019 from 356 billion kwh to 720 billion kwh. This increase in renewable power to 17% of total power generation has been led by the rapid adoption of solar and wind generation, with most of the other sources remaining roughly stable.[3] While wind and solar energy drastically reduce the dependance on fossil fuels, the intermittent nature of many of these sources typically require generators to stabilize the electrical output, especially during hours of peak energy demand. Energy storage facilities have been proposed to address the issue of intermittent power generation and remove the need for additional energy generators. Large battery facilities, such as the Hornsdale Power Reserve and Gateway Energy Storage, have been constructed and implemented to store energy from the grid during off hours to be used during peak hours.

Beyond stationary facilities to reduce intermittency of renewable power, batteries are seeing increased adoption in the transportation sector. In the next ten years, there is an expected ten-fold increase in energy storage demand in the transportation sector as electric vehicles replace their gasoline and diesel-powered counterparts[4]. However modern commercial batteries remain at a significant disadvantage in both energy density and down-time in charging in comparison to gasoline. Increased adoption and reduced greenhouse gas emissions are in part dependent upon improvements in rate-capability and energy density.

Finally, the improvements in battery technology in recent years have, in conjunction with improvements in the semiconductor industry, also led to further electrification of devices. Increases in energy density, for instance, has helped drive widespread adoption of portable electronics such as cell phones and wearable devices. Similar to the automotive field, large growth in demand is expected with most estimates of continual annual growth of over 15% for the next several years[5], [6], [7].

This confluence of increasingly electrified devices, transport, and grid storage for intermittent renewable energy sources has created rapid growth in battery demand. This dramatic increase has created wide interest in addressing the issues holding batteries back from higher rate capabilities, higher energy density, and increased safety.

The wide range of settings that these batteries may be deployed, from electric cars and mobile electronics to industrial and electric grid deployment to potential use in aviation, requires different thermal capabilities. Electric vehicles often operate between -20 and 60 ℃ [8], in part due to thermal instabilities in lithium-ion batteries discussed later. Batteries capable of higher temperature stability could reduce or

outright eliminate the need for thermal management systems used in battery packs. Elimination of this additional mass could further enable electric vehicle adoption and possibly make aviation applications viable.

1.2 Battery Basics

Before addressing the issues presented with modern batteries, it is necessary to discuss how a battery functions. A battery is a series of electrochemical cells composed of cathode, anode, electrolyte, and separator, as depicted in Figure 1. The energy stored in a cell is a combination of the electrochemical potential difference between the reactions at the electrodes, known as voltage, and the amount of charge transferred, known as capacity. During discharge in a lithium-ion cell, lithium ions will travel from the anode, through the electrolyte-separator system, to the cathode, while an electron travels through an external circuit in the same direction. One of the best examples of this is the common LCO-graphite cell which can be simplified to the following electrochemical reactions:

$$LiC_6 \rightarrow C_6 + Li^+ + e^-$$

$$Li_{0.5}CoO_2 + 0.5Li^+ + 0.5e^- \rightarrow LiCoO_2$$

During battery discharge, the graphite of the anode is delithiated at the LCO becomes lithiated, with the cobalt charge state changing from Co^{4+} to Co^{3+} to accept the electron. The voltage range of graphite de/lithiation relative to lithium metal is approximately 0.3-0.05 V, while the usable range of LCO de/lithiation is approximately 3-4.2 V, resulting in nominal cell voltage under 4 V. In secondary cells, such as the

LCO-graphite cell discussed, the reactions are reversible, meaning the cell can be charged and discharged repeatedly.

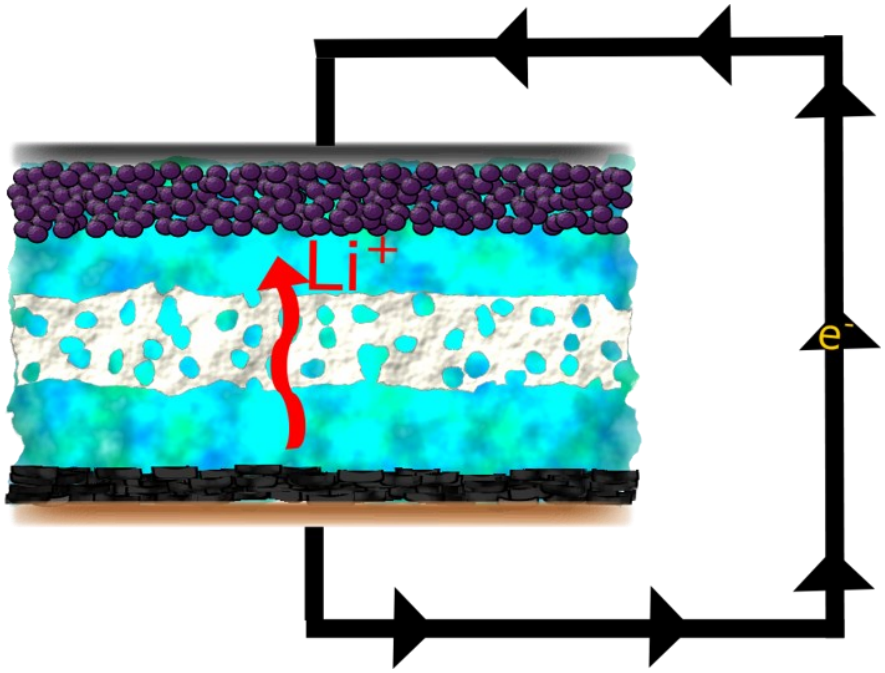

Figure 1. Lithium flow through cell and electron through external circuit in discharge of a cell.

While this seems relatively simple, side reactions occur during charge, discharge, and even when the cell is not in active use that consume cell energy and usable mass. Two of the most notable of these reactions being those creating solid-electrolyte interfaces (SEI), which consumes some of the electrolyte and creates a film of breakdown products, and dendrite formation, where an electronically conductive bridge is formed between the electrodes that short circuits the cell. The nature of these reactions is affected by virtually every component of the cell. SEI is formed largely through decomposition of electrolyte solvents and salts onto the surface of electrode materials. To minimize resistance and capacity loss, a thin relatively conducive layer

is desired, which requires balancing organic and inorganic species formed at these surfaces. However, upon charging or discharging a cell to too extreme of a voltage the electrolyte decomposition reaction will compete with the desired electrode reaction and reduce the efficiency of the cell. This limits the range of voltages a given electrolyte can be used in to what is called the electrochemical stability window. One of the best-known examples of this is water splitting to H_2 and O_2 outside of a set voltage range called the electrochemical stability window. The exact voltage at which this occurs however can be changed via salt and additives present in the system. This shift in breakdown voltage has been related to shifts in the electronic bands around the Highest Occupied Molecular Orbital (HOMO) and Lowest Unoccupied Molecular Orbital (LUMO) of the materials from bonding energies. As this changes the stability of the electrolyte components, there also tends to be a shift in composition of SEI formed.

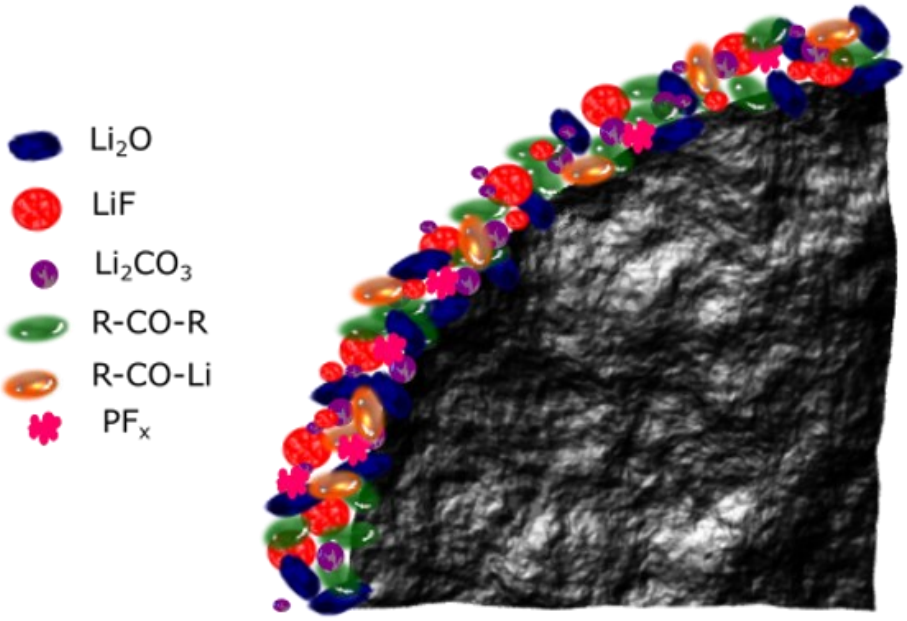

Figure 2. Example of SEI buildup on an electrode particle.

Dendrites on the other hand usually begin from lithium metal plating at the anode. The separator, usually a non-conductive porous polymer, is meant to separate the electrodes and inhibit dendrites through its tortuous porous network. However as a dendrite grows, the distance between it and the cathode decreases resulting in easier lithium deposition to the dendrite. The preferential plating becomes a feedback loop and eventually bridges the anode and cathode, short circuiting the cell.

In addition to these reactions it is important to discuss one other major reaction of commercial lithium ion batteries: combustion. Commercial liquid electrolytes are largely mixtures of organic carbonates such as ethylene carbonate (EC), propylene carbonate (PC), dimethyl carbonate (DMC), diethyl carbonate (DEC), ethyl methyl carbonate (EMC), vinylene carbonate (VC), and fluoroethylene carbonate (FEC) with lithium hexafluorophosphate ($LiPF_6$). All of these components are quite flammable in the presence of oxygen and are especially problematic at elevated temperatures. The flammability of the organic carbonates is exacerbated by the presence of $LiPF_6$, as the anion hexafluorophosphate can react with trace water to form hydrofluoric acid. Thermal decomposition can create phosphorous pentafluoride that catalyze a runaway reaction which results in auto-ignition of the cell. These fires can be particularly difficult for first responders to extinguish and are even capable of re-ignition under certain circumstances.

1.2.1Electrodes

Two basic types of battery electrode exist: intercalation and conversion. Figure 3 shows an expanded view of the two intercalation-type electrodes from Figure 1. In

these electrodes the basic structure of the active material largely remains the same, while ions are hosted and extracted in the material's structure. Some of these materials may experience small, difficult to detect, phase transitions but are still considered intercalation. Graphite undergoes transitions to intermediary species like LiC_{18} between C_6 and LiC_6. Similarly, when delithiated significantly, LCO suffers from irreversible phase change to a rock salt structure. Physical effects of this expansion and contraction can lead to crack-initiation and breakdown of active material particles which lose contact and become electrochemically dead mass.

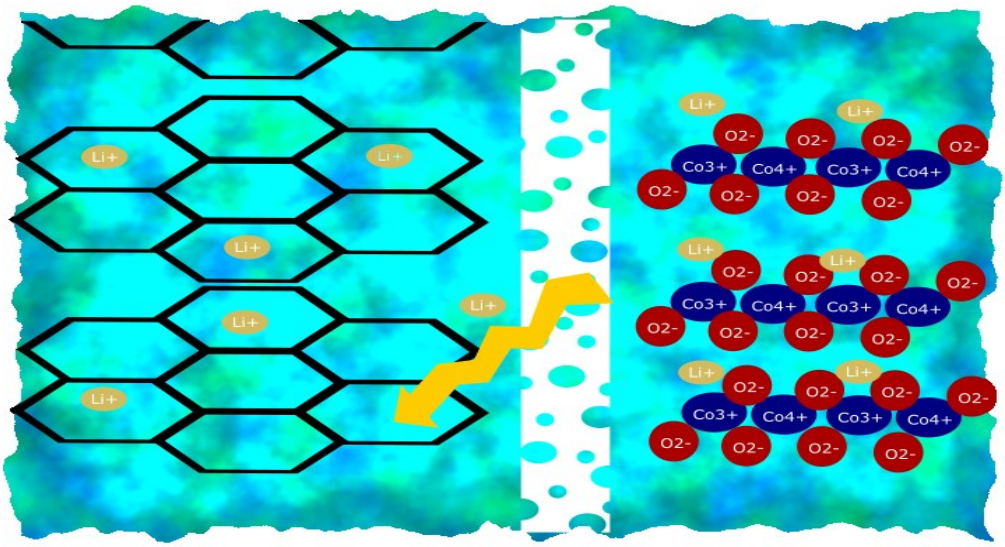

Figure 3. Example of lithium moving within a cell using two intercalation electrodes in a rocking chair setup.

Many of the commercially relevant cathodes, such as $LiNi_xCo_yAl_zO_2$ (NCA) or $LiNi_xMn_yCo_zO_2$ (NMC) where x+y+z=1, build upon the same or similar layered or spinel structures. These cathodes accomplish two major goals: improved performance, both in rate and energy density, and a reduced consumption of cobalt which has a problematic supply chain. Unfortunately, these improvements come with the tradeoffs of inherent issues related to both capacity and voltage decay[9], [10], [11], [12], [13].

One of the mechanisms for this decay, oxygen release, ties into a larger safety issue suffered by layered transition metal oxide structures. Oxygen release occurs as a result of electrochemical reactions, or upon heating of cells. The production of oxygen during heating contributes significantly to thermal runaway[14], [15]. $LiFePO_4$ (LFP) cells on the other hand, have shown not only higher onset temperatures for thermal runaway, but lower temperatures reached during runaway when compared to their layered counterparts[16]. This significant safety improvement along with its lower cost has led to LFP replacing NMC and NCA in many commercial batteries despite lower energy density.

Whereas intercalation-type cathodes may undergo small phase transitions, conversion-type electrodes utilize phase changes to accommodate active ions, such as Li^+, resulting in significantly higher theoretical capacities than intercalation. While graphite can only intercalate one lithium for every six carbon atoms, silicon can accept more than four lithium ions, theoretically. However, the tradeoff for higher capacity is extreme volume expansion which exacerbates CAM pulverization. Some conversion electrodes can minimize this effect by generating intermediary species that can dissolve in the electrolyte used. Sulfur, for instance, can form a series of lithium polysulfides such as Li_2S_8 or Li_2S_6, as depicted in Figure 4, which easily dissolve in commonly ether-based electrolyte. Further lithiation to species such as Li_2S can precipitate back onto the conductive backbone of the electrode. Solubility of active material however creates its own issues such as the polysulfide shuttle, wherein the soluble species diffuse to the opposite anode causing loss of active material and potential parasitic reactions.

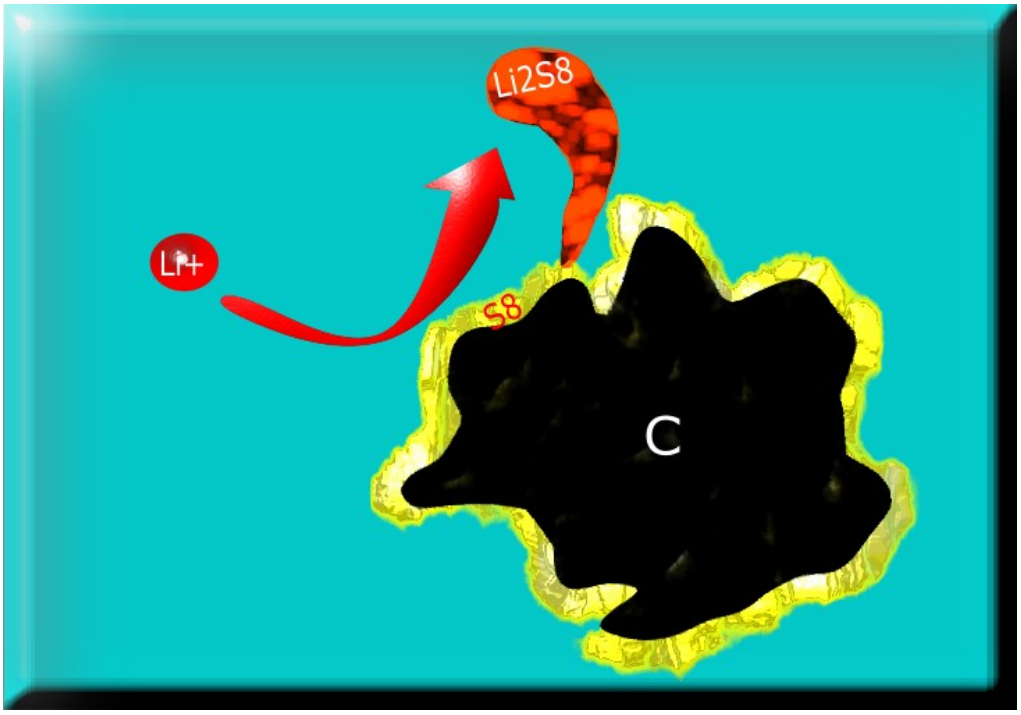

Figure 4. Lithium ions reacting with elemental sulfur to form lithium polysulfides on carbon surface.

1.2.2 Electrolytes

While most electrode materials have some degree of lithium conductivity, the need for conductivity through the separator layer and between electrode particles in cells with appreciable capacity requires a lithium conductive electrolyte. When the previously mentioned LCO-graphite system was being developed, organic carbonate systems were found compatible and have largely remained the backbone of lithium electrolyte systems since. Most "standard" liquid electrolytes are 1M $LiPF_6$ in a solvent system containing either cyclic EC with one of the linear carbonates DEC/EMC/DMC or cyclic PC.

Lithium salts, $LiPF_6$ in the example above, are required to have sufficient availability of lithium ions in the electrolyte to allow conduction and avoid rapid

polarization. The anion, here PF_6^-, plays a key role in determining several factors that affect battery performance: from viscosity and interfacial resistances to stability window and interfacial layer compositions. As previously discussed, PF_6^- is critical in the thermal instability of common lithium-ion batteries through its dissociation and decomposition into a series of highly reactive fluorophosphates, oxyfluorophosphates, and hydrofluoric acid. Alternative lithium salts to $LiPF_6$ include lithium bis(trifluoromethanesulfonyl)imide (LiTFSI) and lithium bis(fluorosulfonyl)imide (LiFSI). LiTFSI containing electrolytes tend to be more thermally stable than LiFSI or $LiPF_6$, while also being more viscous and lower conductivity. While more stable than $LiPF_6$, LiFSI usually has somewhat lower conductivity. However, both LiTFSI and LiFSI salts have corrosion issues when used in conjunction with traditional carbonate solvents at elevated voltages[17], [18], [19], [20].

Cyclic carbonates EC and PC have good solubility for commonly used lithium salts and good thermal stability, with boiling points well above room temperatures. Graphite's instability with PC has historically negated its lower viscosity than EC as it led to drastic capacity decay[21], [22]. Linear carbonates began to be added to EC as a method to stabilize EC-based electrolytes as a liquid at room temperature[23], [24], [25], [26].

1.2.3 Separator

Given the need for good electronic conductivity through electrodes in order to perform electrochemical reactions, physical separation is a necessity to avoid shorting so that energy may be stored. While electrolytes allow lithium transport between

electrodes, the liquid electrolytes traditionally used are incapable of also providing the required physical separation, necessitating an independent separator. To create this separation while allowing the liquid electrolyte to transport lithium microporous structures of insulating materials which can absorb electrolyte are implemented. Both material choice and exact microstructure of the separator affect both performance and longevity for cells created. For traditional carbonate electrolyte systems polymeric blends of polypropylene and polyethylene, such as many Celgard separators, have been used. Many other liquid electrolytes cannot sufficiently wet these polymer blends, preventing their ability to infiltrate into these separators and are thus incompatible. Many ionic liquids, for instance, have traditionally used glass fiber separators due to such issues.

While the chemical composition plays a large role in determining compatibility between electrolyte and separator, separator microstructure plays a significant role in cell performance. One of the most studied measures of this microstructural impact is that of tortuosity, or the ratio of the length of the path travelled to that of the straight-line distance between the two points. In the context of separators in a lithium battery this is the path a lithium ion travels through the separator relative to the thickness of the separator. The less tortuous the pathway, the quicker a lithium ion can diffuse through the separator resulting in higher conductivity within the cell. A more straightforward path for lithium ions also makes for more linear paths for lithium dendrites to travel. The size of these pathways affects numerous properties, such as wettability and dendrite blocking properties of the separator[27], [28], [29], [30], [31]. Consider the four simplified separator examples in Figure 5, assuming the same

porosity, and the ease with which a particle could travel through them from top to bottom. Samples A and B both provide straightforward paths, assuming the particle is sufficiently smaller than the openings, as the paths are non-tortuous. Sample C, however, provides no pathway through in this direction despite the same amount of pore space. By effectively combining these two types of pathways, sample D introduces some tortuosity to the particle's path while still providing a way through.

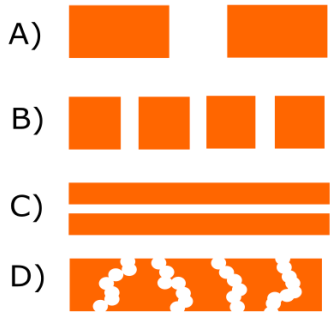

Figure 5. Simplified cross-sectional depictions of some possible porous structures.

One standardized method used to compare many of these factors across separators of different materials and microstructures is the MacMullen number. While this factor can be calculated if given enough microstructural data, through the equation below where τ is effective tortuosity and ε is porosity[32], the ease of experimental determination enables quick comparison, as it can also be calculated as the simple ratio of the measured conductivity of the separator-liquid electrolyte system to that of the liquid electrolyte itself.

$$N_M = \frac{\sigma_{total}}{\sigma_{LE}} = \frac{\tau}{\epsilon}$$

1.3 Advanced Lithium Electrolytes

1.3.1 Additives

As with all electrochemical systems, battery chemistry can highly be sensitive to even small addition or modifications. This has led researchers to create several series of electrolyte additives from interfacial modifiers to fire retardants to viscosity additives and more. While interfacial modifiers can be further subdivided into salts and solvents, their basic purpose and broad methods remain the same. These additives should be more or at least equally likely to break down at the voltages present at one or more electrode allowing for a shift SEI or CEI chemistries. When properly selected, this allows for thinner, more robust, and more conductive interfacial layers, usually resulting from boron or fluorine-rich compounds or otherwise capable of crosslinking. As most common lithium salts are already fluorine rich, additive salts are more commonly boron related such as LiBOB or LiDFOB. Alteration of existing solvent will often incorporate more fluorine or improved crosslinking capability, such as EC into FEC or VC respectively.

Some of these same additives have been shown to help another key issue with traditional liquid electrolytes: flammability. Chemicals can be added which either act as fire retardants or themselves have low flammability. Certain additives, namely phosphates, phosphites and certain fluorinated organics, can remove reactive free radicals from solution that would otherwise propagate fires[33], [34]. These phosphorous based solvents have further been shown to help reduce oxygen pressure that can be released from oxide cathodes under high temperatures, further reducing cell flammability[35].

1.3.2 Ionic Liquids

One of the most interesting topics related to liquid batteries in recent years has been inclusion of ionic liquids (ILs), particularly room temperature ionic liquids (rtILs). These are salts systems that remain liquid at room temperature, which provide the ability to easily tailor properties through cation/anions choice or substitution. By utilizing the same anions from traditional liquid electrolytes' lithium salts wide electrochemical stabilities have been attained. Furthermore, many of these rtILs have attained high electrochemical stability windows in addition to extremely low flammability[7], [36] . While conductivity is typically below that of a traditional carbonate electrolyte in part leading to lower initial capacity, the interfacial layers formed are often highly fluorinated and compact leading to more stable cycling in with many electrodes.

1.3.3 High Concentration Electrolytes

Most liquid electrolyte systems, such as the mentioned "standard" carbonate electrolytes, utilize salts in concentrations of roughly 1 M or less as increasing concentration above this tends to significantly increase viscosity and lower conductivity. However, when this concentration sufficiently increased, new local maximums in conductivity appear and display altered electrochemical properties. In normal dilute concentrations, carbonate electrolytes with LiTFSI salt will corrode aluminum current collectors within the normal operating voltages of most commercial

cathodes[19], [20], [37], [38]. Once pushed to high concentrations of 3-1 molar ration of solvent to salt, EC and DEC displayed negligible corrosion currents among the same voltage regime[17]. Similarly, PC with high concentration of LiTFSI was shown to no longer exfoliate graphite anodes[39]. This stabilizing effect is not limited only to organic carbonate electrolytes but has shown promising results in disparate solvents ranging from non-traditional battery solvents such as ethyl acetate and acetonitrile to extending the usable range of water-based electrolyte well beyond the traditional 1.3 V range to turning glymes into ionic liquid systems[40], [41], [42], [43], [44].

Many of these effects are possible due to the inherent change in bonding structures that occurs once concentration shifts significantly enough. As this bonding amongst lithium and solvent and the salt's anion is rearranged, the internal electronic structure is altered and HOMO and LUMO of the system is shifted. In the aforementioned LiTFSI-EC at aluminum current collector, the increase in LiTFSI results in a removal of uncoordinated EC which minimizes its reaction with the current collector and allows a fluorine-rich passivation layer to form from the now more vulnerable TFSI anion[17].

Recently, these electrolytes have been paired with fluoroether dilutants to form Localized High Concentration Electrolytes (LHCE). The fluoroethers display negligible interaction with lithium salts, allowing for the localized bonding of salt and solvent to remain the same while the viscosity of the system to be lowered[45], [46], [47], [48], [49], [50].

1.3.4 Lithium Conductive Ceramics

One path suggested to address issues with lithium-ion batteries is to switch to solid-state electrolyte-based systems. By replacing high volatility organics with either solid polymer or ceramic based electrolyte systems cell flammability is drastically reduced. Of these two options, ceramic electrolyte will be focused upon in this work due to higher thermal stability, wider electrochemical stability, and greater resistance to dendrite formation. Some of the early lithium ceramic electrolyte work was with the perovskite lithium lanthanum titanate (LLTO) and lithium phosphorous oxynitride (LiPON). LLTO exhibited exceptional conductivity but, upon contact with lithium metal the titanium reduces and causing electronic conductivity through the electrolyte thus shorting the cell[36], [51]. LiPON has shown good interface with lithium metal, but much lower conductivity than other ceramics, largely limiting its application to micro batteries[52]. Of the other common ceramics electrolytes, including LATP, thio-LiSICON, and LLZO, garnet exhibits some of the most promise with good lithium conductivity (10^{-3}-10^{-4} S/cm), wide electrochemical stability window (>5V from CV studies), and lowest theoretical driving forces to reaction with lithium metal[52], [53].

1.4 Lithium Garnet Electrolyte based Batteries

1.4.1 Crystal Structure and Site Dopants

As previously stated, lithium-stuffed garnet is one of the most promising lithium electrolytes materials due to stability to lithium, wide electrochemical stability window, high conductivity, and nonflammability. One of the key issues tackled early

with garnet was stabilizing the more conductive cubic phase over its tetragonal polymorph, unit cells of which can be seen in Figure 6B and A respectively. This was largely addressed, along with achieving higher conductivity, through doping the crystal structure. Aluminum doping, even from contact with alumina crucibles used in calcination and sintering, has been one of the most widely used for this purpose[54], [55]. In the garnet structure, it occupies tetrahedral lithium sites which blocks some of the lithium pathways, but by stabilizing the cubic phase produces a net conductivity increase[56], [57], [58]. The cause of this can be observed by inspection of the lithium sublattices in these structures. Figure 6C and D show that the lithium sublattice becomes far more interconnected in the cubic phase than the tetragonal. The formation of this interconnected 3-D hexagonal network more than compensates for the loss of some of the tetragonal lithium sites, the darker orange lithium in Figure 6D. However, aluminum, as well as magnesium, has been shown to self-segregate to grain boundaries creating inhomogeneity in the system[59], [60]. Niobium and tantalum, both of which substitute on the zirconium site, have been two of the most popular cubic phase-stabilizer dopants. Recent simulations by Zhu et al have shown that aluminum and niobium are more likely to reduce and cause the garnet to short circuit than tantalum[61]. Some lanthanum-site dopants of note are alkali-earth elements, such as calcium and barium, which have been noted to improve density and ionic conductivity [62], [63], [64]. Additionally, praseodymium replacement of lanthanum has recently been shown to enable garnet to function as a mixed ionic electronic conductor (MIEC)[65].

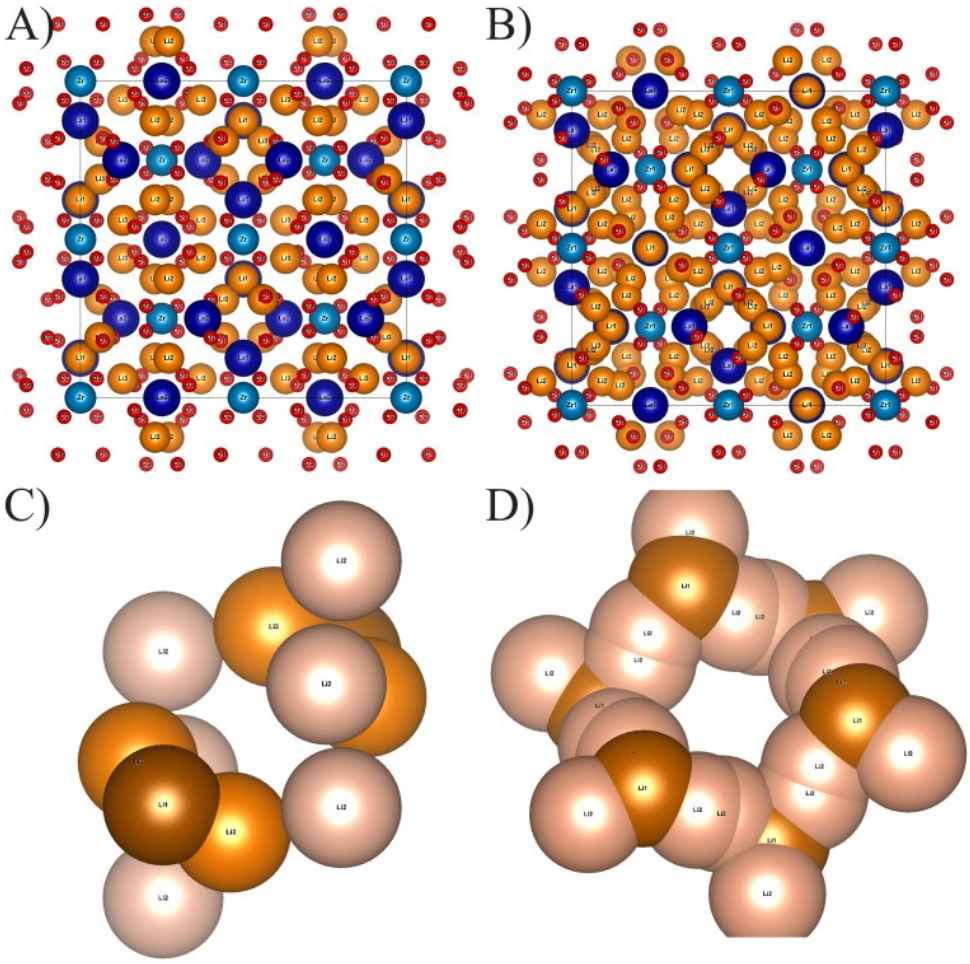

Figure 6. Unit cell for A) tetragonal and B) cubic phase garnet, with lithium, oxygen, lanthanum, and zirconium depicted using orange, red, royal blue, and light blue. Lithium sublattice for $1/8^{th}$ of a unit cell for C) tetragonal and D) cubic garnet with different lithium sites using different shades of orange. Images made using Vesta[1].

1.4.2 Reactive Surface and Microstructure

Many other difficulties in ceramic electrolyte systems stem from various interfacial properties, from the rigid nature of ceramics limiting interfacial area with electrodes to their reactivity. While garnet is considered stable with lithium metal[52], [66], [67] it has had other compatibility with this anode due to the lithiophobic surface presented by garnet. Formation of surface lithium carbonate, spontaneously formed

through interaction with moisture and CO_2, has been shown to be the main cause of this lithiophobicity[68], [69]. To combat the effect of this surface carbonate, three main methods have been utilized: additional anolyte, thermal annealing, or application of interfacial layer[70], [71], [72], [73], [74], [75], [76], [77]. Measured largely through EIS and cycling of symmetric lithium cells, these approaches show reduced resistance and allow for increased areal current through garnet. Another method used to increase achievable areal current has been modification of garnet to create increased surface area between garnet and lithium metal, thus increasing the available sites for charge transfer and lithium deposition. As discussed in previous work from our group, porous garnet scaffold can be sintered with dense solid electrolyte layer to provide volume for lithium plating and stripping to minimize cell-level expansion and contraction observed in typical of lithium metal cells[78], [79], [80], [81].

1.4.3 Ceramic Processing

Traditional solid-state ceramic processing requires an initial mixing and calcination process to achieve phase-pure powders. These powders are then pressed and sintered into solid pellets of the same final phase. The final sintered pellets can then be polished down to a more reasonable thickness, however this does induce scratches to the garnet surface from the polishing process. This has historically dominated the field given its repeatability and simplicity. Several groups have adopted various other bulk processes to improve energy density of cells by reducing the mass of the electrolyte. Tape casting has been one of the main ones with variants such as freeze-casting also employed[79], [82], [83], [84].

To further reduce garnet's mass contribution, several groups have synthesized thin-film garnet electrolytes. Some methods that have successfully created thin-film garnets are sol-gel deposition, spray deposition, pulsed laser deposition (PLD), chemical vapor deposition, sputtering, and atomic layer deposition (ALD)[85], [86], [87], [88], [89], [90]. However, the lithium conductivity in all of these structures was closer to that of LiPON than that of bulk cubic phase garnet. Furthermore, these methods tend to utilize even more reactive and expensive precursors than the oxides, carbonates, and even hydroxides common to solid-state bulk synthesis. Importantly, these methods do not produce free-standing structures, instead being deposited onto a substrate. Given garnet is not thermally stable to most cathode materials [91], [92], and the general chemical instability of lithium metal, this has meant that substrate materials have not been electrode material. This makes the use of parallel electrodes, as depicted in Figure 1, very difficult with only a few, such as Sastre et al's micro-batteries[93], [94], achieving full cell cycling.

1.4.4 Added Electrolyte Systems

One of the easiest ways to increase conduction between ceramic cathode particles and ceramic electrolyte is the introduction of a catholyte to ionically bridge the surfaces of the two materials. This has been done by numerous groups using traditional cathode sheets being wetted to garnet, or other solid-state electrolytes, using liquid electrolytes[95], [96], [97], [98], [99]. The resistance at these solid-liquid junctions have traditionally been related to the difference in energy states of the lithium

ion in the solid and liquid and whatever intermediaries occur. Many early works on this topic, while disagreeing on the symmetric nature, have shown the rate limiting step to be solvation/desolvation of the lithium ion at the interface[100], [101]. Many have linked the activation energy of this resistance to the donor number of the liquid present, largely regardless of concentration, and its ability to solvate lithium salts present[99]. More recently works have also been looking at the reactivity between the electrolytes and films formed between the two[102], [103], [104]. Similar to SEI, a solid-liquid electrolyte interface (SLEI) layer can form on the surface of solid electrolytes through breakdown of the liquid and salt at the surface of the ceramic[99], [102], [103].

In addition to reaction, standard liquid electrolytes (i.e. carbonates for oxide cathodes and ethers for sulfur) reintroduce flammability back into the system, though lessened as the anode is shielded by the ceramic. One promising method of increasing interfacial contact while avoiding reintroduction of flammability is using ionic liquids (IL) electrolytes. While not as conductive as standard organic liquid electrolytes, ionic liquids are still capable of good lithium conduction and wetting cathode and solid electrolyte interfaces.

Ionic liquid electrolytes display a similar balancing act as is required in standard liquid electrolytes with regards to salt concentration. Low lithium salt concentrations have desirable viscosity and total conduction while lithium transference number, the ratio of lithium conductivity to that of total conductivity, is low. Increasing salt concentration reverses this trend tending towards high transference number with very high viscosities[105], [106]. To help balance these properties, many groups have used liquid electrolytes combining ionic liquid with more traditional electrolytes, such as

carbonates or ethers depending upon the cell chemistry[107], [108], [109]. These hybrid organic-ionic liquid systems even maintain nonflammability dependent upon the ratio used.

1.4.5 Aging related issues in select advance electrolytes

Cell aging, especially under enhanced conditions, is one of the biggest tests for real-worlds viability. In lithium-ion cells calendar aging, where cathode active material is slowly dissolved and deposited elsewhere, is a major issue. Sulfide electrolytes have been shown to react with the cathodes over time as well[110]. Ionic liquids, as shown in capacitors, show loss via leakage current[111]. Despite the importance of degradation studies of cathodes in traditional organic liquid electrolyte, most all degradation studies involving garnet focus on hydration of garnet and formation surface lithium carbonate prior to cycling, reaction with cathode during sintering, and dendritic growth. While these topics are of great import, deeper understanding of cell-level breakdown from all components and potential crosstalk is essential to moving garnet-based cells to realistic market adoption.

Chapter 2: Methods

2.1 Garnet Synthesis

2.1.1 Powder Synthesis

Garnet powders of the composition $Li_{6.75}La_3Zr_{1.75}Ta_{0.25}O_{12}$ were produced via solid state synthesis involving precursor milling in high density polyethylene bottles with isopropanol with YSZ milling media using $LiOH*H_2O$ (Alfa Aesar), La_2O_3(GFS Chemicals), ZrO_2(Inframat Advanced Materials), and Ta_2O_5(Alfa Aesar) as precursor powders. The slurry of precursor powders were then sieved into a stainless-steel pan to dry at 105 °C. This powder was then pressed and calcined at 900 °C for 10 hours. Resultant powders would then be milled high density polyethylene bottles with isopropanol for either one day with mostly 5 mm YSZ media, to be used in porous tapes, or two days with 5 mm YSZ media and five days with 2 mm YSZ media, to be used in dense tapes. Powder that would be used for reactive phase sintering underwent only an extended precursor milling and drying prior to tapecasting.

2.1.2 Tape casting, Green Body Handling, and Sintering

Bilayer, trilayer, and laminated dense garnet structures were created via a tapecasting, lamination, and sintering process similar to the methods described in other works[77], [79] as detailed below. Powders slurries were made by allowing ethanol, fish oil, and the appropriate powder to mill for a minimum of 12 hours. Dense tapes for traditional garnet pellets, bilayers, and trilayers used a highly milled garnet of approximately 300 nm diameter as measured via Malvern Zetasizer Nano ZS dynamic

light scattering. Traditional porous tapes used the more lightly milled garnet powders of around 500 nm diameter, occasionally incorporating precursor powders to modulate the shrinkage rate of the tapes. Modified interlayer, thin flexible garnet separator, and thin dense garnet utilized either in-house milled precursor powder or nano-sized precursors mixed only in the dispersal phase of casting. Tapes of all types often incorporated additional lithium carbonate to minimize lithium loss and aid sintering. A binder-plasticizer slurry of polyvinyl butyrol, benzyl butyl phthalate, and polyalkyl glycols (tapecasting warehouse) in ethanol would then be mixed in an AER-310 Centrifugal Thinky mixer. An hour before the introduction of powder slurry to binder-plasticizer slurry, porous tapes would have PMMA spheres to the powder slurry to function as pore former. Upon uniform mixing, the powder slurry was sieved into the binder-plasticizer slurry vessel and mixed in the same Thinky mixer. After uniform slurry was achieved, the lid was removed from the vessel and the sample spun an additional 30 seconds to allow final the slurry to degas. The final slurry was cast at 120˚F in a tape caster from Pro-cast using a doctor blade at set heights, dependent upon the desired final thickness.

Lamination of tapes was performed interchangeably in a hot press at 180 ˚F or roll laminator. Powderbed was then applied to magnesia plates: garnet powderbed of the same composition for traditional garnet structures and a range of powderbeds for thin garnets from MgO/Li_2CO_3 to graphite and graphite mixed with Li_2CO_3 as indicated in the work. Thin dense garnets utilized presintering in air at 550 ℃ followed by designated temperatures under argon. More traditional garnets were sintered under O_2 flow, except where indicated otherwise.

The resultant slurry was tape-cast and laminated to desired thickness, and the final green-bodies sintered. Tapes of LCO, LTO, and LLTO, were synthesized similarly: precursors were mixed in the dispersion milling Co_3O_4 (Inframat), TiO_2 (Sigma Aldrich), and the same lanthanum and lithium precursors previously mentioned, cast, and laminated where necessary.

Sintered pressed pellets, used only in the hydrophobing section of this work, were made using the same powder used for porous tapes described above. The powder was placed in ¼'' die and pressed at 2 tons for 1 minute, before burying in the same mother powder. Pellets were then sintered for 16 hours at 1050 °C, before using a series of polishing pads with isopropyl alcohol to achieve uniform smooth surfaces.

2.1.3 Coatings

Lithium polyacrylate (LiPAA) was synthesized through acid neutralization of dissolved poly(acrylic acid) as discussed by Loho et al and Piekzonka[112], [113]. After synthesis, LiPAA was redissolved in water and infiltrated into porous garnet network and allowed to dry under atmospheric conditions overnight.

In preparation for ALD coatings, sintered garnet structures were heated to 850 °C to remove lithium carbonate from the surface. The samples were then transferred to the glovebox, which was under argon atmosphere, and then into ALD chamber. Alumina or zinc oxide layers were then deposited on the garnet using trimethyl aluminum or diethyl zinc and deionized water in a custom Forge Nano ALD chamber similar work described in other works[77], [114].

Fatty acids were added to toluene heated to 60 ℃ and stirred in a beaker with a watch glass. Once thoroughly dissolved and dispersed, garnet powder was added into the beaker and allowed to dry. Alternatively, pellets would be lowered into solution in aluminum boats for specified times before drying at 105℃.

2.2 Electrode Sheet and Liquid Electrolyte Preparation

2.2.1 Drying

1-butyl 1-methyl pyrrolidinium bis(trifluoromethylsulfonyl)imide ($Pyr_{14}TFSI$) (Iolitec), lithium bis(trifluoromethylsulfonyl)imide (LiTFSI) (Sigma-Aldrich), lithium iron phosphate (LFP) (MTI), super-P carbon, polyvinylidene fluoride (PVDF) (Alfa Aesar), glass fiber separators (Whatman), and glass slides were dried in a heated vacuum chamber at 115°C for 20 hours. Acetonitrile (ACN) and triethyl phosphate (TEP) used in the catholytes were dried using 3 Å molecular sieves. The fluoroether dilutants, Bis(2,2,2-trifluoroethyl) ether (BTFE) (Synquest Laboratories), 1H,1H,5H,5H-octafluoropethyl 1,1,2,2-tetraflyoroethyl ether (OFPTFE) (Fisher Scientific), and 1,1,2,2-Tetrafluoroethyl 2,2,2-trifluoroethyl ether (TTFETFE) (TCI Chemicals), were used as received. Karl-Fischer titration was performed using a Hanna instruments HI904 Karl Fischer Coulometric Titrator to ensure water concentration in the solvents used in the electrolyte remained below 20ppm.

2.2.2 Electrode Sheet Preparation

LFP particles were mixed with PVDF and Super-P carbon in a 91:4.5:4.5 ratio in methylpyrrolidone (NMP) using first a Vortex mixer in an argon filled glovebox, then sealed and mixed in an ARE-310 Centrifugal Thinky Mixer. The resultant slurry was cast via tape caster and doctor blade onto carbon-coated aluminum foil (MTI Coproration). Loading was controlled via solvent concentration and blade height. Cathodes for chapter 3 had loading between 5-15 mg/cm^2 while those used for Chapter 4 were between 10-13 mg/cm^2. After drying overnight at low temperature, these cathode tapes were cut and vacuum dried in the same manner as the powder to remove residual NMP and any newly adsorbed water.

NMC cathodes were ordered through NEI with 11 mg/cm^2 active coating. Cathode sheets were then vacuum dried before use at 115°C for 16 hours while graphite electrodes were provided via CAMP and the Department of Energy. All cast electrodes were vacuum dried at 115°C for 16 hours before use in cells.

Stand-alone reactive-sintered electrodes were adhered to current collectors though application of dilute Super P carbon/PVDF/NMP solutions of appropriate aluminum or copper foils followed by drying at 115°C.

2.2.3 Liquid Electrolyte preparation

Liquid electrolytes were stoichiometrically weighed and allowed to mix overnight on stir plates. Unless otherwise stated, the amount of co-solvent used was 10% by volume. The stated lithium molarity includes the co-solvent volume except for the fluoroether dilutants where molarity is considering only salt and ionic liquid.

2.3 Cell Assembly

2.3.1 Lithium Wetting and Infiltration

Lithium metal was wetted onto stainless steel discs on a hotplate at 215°C inside of a glovebox with argon atmosphere. Tweezers and razor blades were then used to clean the lithium surface to a mirror finish and wetted to nickel or titanium foils to serve as current collectors. The lithium metal was then introduced to garnet to wet onto/into the garnet surface/pore structure. Actual temperature was determined using a laser thermometer and subsequent work was performed at the same temperature setting.

2.3.2 Electrode Sheet Application and Cell Assembly for Quasi-Solid-state cells

Liquid electrolyte was applied to the cathode via micropipette. Catholytes were allowed to wet the cathode sheets for 15 minutes before introduction to garnet surfaces. For cells in chapter 3, this was at a ratio of approximately 1 μL:1 mg cathode active material (CAM) in full cells, approximately 1.5 μL:1 mg ACM in chapter 4 for LFP full cells, 3 μL:1 mg CAM for symmetric cathode cells and most other full cells. Liquid electrolyte used was based on 0.5 M LiTFSI $Pyr_{14}TFSI$ in Chapters 3 and 4 and 1 M $LiPF_6$ EC/DEC in later chapters (Sigma Aldrich). Full cells using thin dense LLZT incorporated Celgard in between cathode tapes and thin ceramic to provide mechanical support. Coin cells assembled in MTI press in 316 stainless steel coin cells. Pouch cells assembled in MTI pouch sealer.

2.4 Structure, Bonding, and Thermal Analysis

2.4.1 SEM and XRD

Hitachi S-3400 Variable Pressure SEM and Tescan XEIA FEG SEM and Hitachi SU-70 FEG SEM used in Fablab and Aimlab facilities. Microstructure was observed via normal scanning and backscatter mode. Grain-grain boundary bonding and density/porosity was observed in scanning mode. Backscatter and/or top-down viewing of dense layers better enabled observation of secondary phases present, with EDS identifying the rough composition of these phases. Images often analyzed using IMAGEJ software[115].

XRD was performed using D8 diffractometer. Phases identified using EVA software. Rietveld Refinement was performed using GSAS-II[116].

2.4.2 Raman Spectroscopy and TGA/DSC

Raman spectroscopy was performed on Horiba Jobin Yvon-Labram Aramis confocal Raman microscopy using a 532 nm laser. Samples for Raman were sandwiched between two dried glass slides using a double seal of vacuum grease and an epoxy under argon to avoid introduction of atmospheric contaminates.

TGA/DSC was performed in a TA Instruments SDT 650 Simultaneous Thermal Analyzer in alumina boats.

2.5 Electrochemical Testing

2.5.1 EIS and DRT

EIS performed using Biologic VMP-3 impedance analyzer. Electrochemical impedance spectroscopy uses alternating current or potential at given frequencies and observe the response. Distribution of relaxation Times performed using DRTtools through MATLAB[117]. DRT shifts frequency into time domain and then uses Fourier fast transformations to help delineate phenomena in EIS data. This by itself does not assign physical meaning to individual peaks but through proper experimentation meaning can be assigned. Cincinnati Sub-Zero and Thermal Product Solutions Tenney environmental chambers were used for elevated temperature testing.

2.5.2 Cycling

Cells were cycled on Arbin and Biologic VMP-3 systems. Most cycling profiles were symmetric galvanostatic charge-discharge profiles. Porous separator and thin dense garnet full cells were cycled using constant-current-constant-voltage profiles. For Calendar aging tests, cells were cycled under galvanostatic conditions followed by leaving the cell under open circuit for specified times before galvanostatic discharge. Cyclic voltammetry (CV) was performed to determine electrochemical stability of select catholytes using aluminum and either copper or lithium current collectors with glass fiber separators.

2.5.3 MacMullen Testing

Cells were constructed of specified number of separator layers infiltrated standard liquid electrolyte (1M $LiPF_6$ EC/DEC) using 316 stainless steel as electrodes. Conductivity was determined via x-intercept from EIS of the cells and plotted as a function of total separator thickness, which was used to calculate MacMullen Number.

Chapter 3: Understanding Limitation of Quasi-solid state lithium garnet-ionic liquid cells and addressing resistance

3.1 Effects of Cathode Loading on Full Cell Performance

Figure 7, Figure 8, and Figure 9 display the discharge capacity and coulombic efficiency for varied loading of LFP cathode at approximately A) 5 mg/cm^2, B) 10 mg/cm^2, and C) 15 mg/cm^2. Figure 7A shows that after 50 cycles at C/1.6 (520 μA/cm^2) and 90°C the low loading LFP cathode (4.9mg/cm^2) cell anomalously long charging was observed by the presence of cycles with large coulombic efficiency drops without corresponding discharge capacity loss. 137 cycles under these conditions the cell retained 83% of its maximum capacity, before the voltage window was shrunk to limit the long-charge issue. While decreasing the initial discharge capacity, limiting voltage window to 3.75-3V drastically reduced the frequency of observed long-charge, and decreased the rate of capacity decay. Further limiting the window to 3.6-3.2V, however, did not result in similar improvements. Thus, the voltage window was limited in subsequent cycling along with the allowed charge time. However, this issue would still occur in subsequent cells upon sufficiently high charge rates and used as an indicator of cell instability.

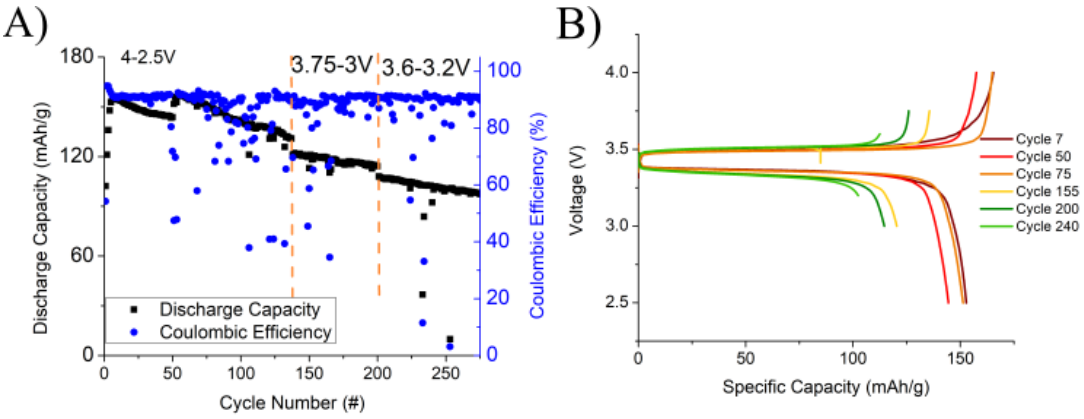

Figure 7. Galvanostatic cycling A) discharge-coulombic efficiency and B) voltage profile with cathode loadings of approximately 5 mg/cm^2. Unless stated otherwise all cycling is performed at 90°C.

Figure 8A shows that the initial cycling of the medium (9.8 mg/cm^2) loading cell had similarly noisy data when cycling between 4 and 2.5V, though 150 mAh/g was achieved. Reducing voltage window to 3.75-3.25C and cycling at C/15 (108 µA/cm^2), C/5 (324 µA/cm^2), C/3 (540 µA/cm^2), and C/2 (830 µA/cm2) resulted in capacities of 128, 107, 91, and 64 mAh/g respectively, with the long-charge issue first appearing in C/3 (540 µA/cm^2) cycling. While unstable due to the long-charge issue, upon returning to C/15 cycling 118 mAh/g discharge capacity was achieved.

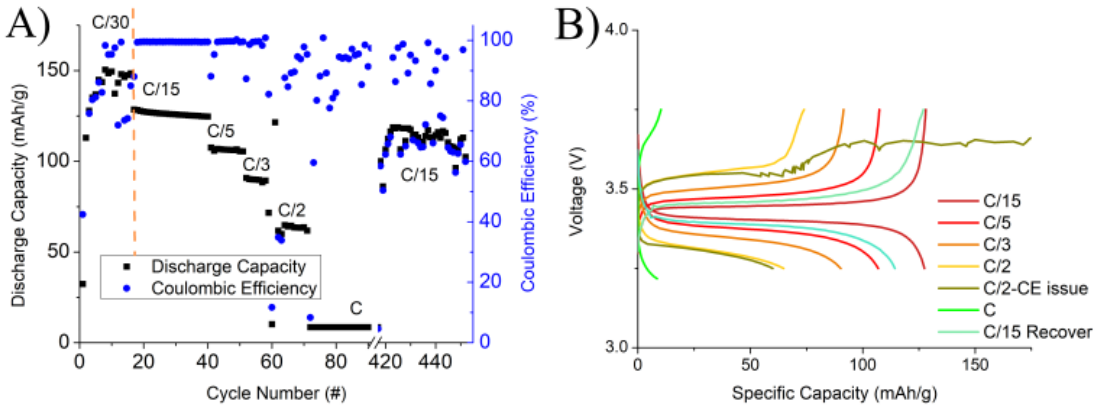

Figure 8. Galvanostatic cycling A) discharge-coulombic efficiency and B) voltage profile with cathode loadings of approximately 10 mg/cm^2. Unless stated otherwise all cycling is performed at 90°C.

Cycling between 3.75 and 2.75V, Figure 9A shows the cell with the highest loading cathode (14.6 mg/cm^2) tested achieved capacities of 82 and 145 mAh/g at room temperature and 90°C respectively at C/50 (50 μA/cm^2). The cell maintained capacity of 133 and 119 mAh/g after increasing rate to C/20 (125 μA/cm^2) and C/10 (250 μA/cm^2) when at 90°C before long charging became an issue. Upon returning to C/50, capacity increased back to 128 mAh/g. Comparing the voltage-capacity behavior of this cell in Figure 9B, the reduction of resistance is observed through the reduced overpotential of 90°C cycling relative to room temperature cycles. Furthermore, these voltage profiles help display some of what occurs during the long-charge issue observed after the LFP charge plateau, where the voltage profile has a sudden outward inflection post-plateau in a C/10 charge.

Despite long-charge related issues, garnet bilayer cells showed high capacities of 157, 150, and 145 mAh/g at 90°C for the respective loadings of 5, 10, and 15 mg/cm^2. However, the C-rate at which useful capacity was achievable, and at which instability was noted, varied greatly upon the loading utilized, instead showing a closer relation to the areal capacity. This becomes especially apparent as the cell 10 mg/cm^2 began long charge issue around 0.5 mA/cm^2 -the same areal current as the lower loading cell. Interestingly, the high loading cell was not able to reach this areal current, achieving 0.25 instead of 0.5 mA/cm^2. Taken together, this seems indicative of a planar interface dominating resistance, likely that of garnet-ionic liquid, until loadings increase enough to sufficiently contribute.

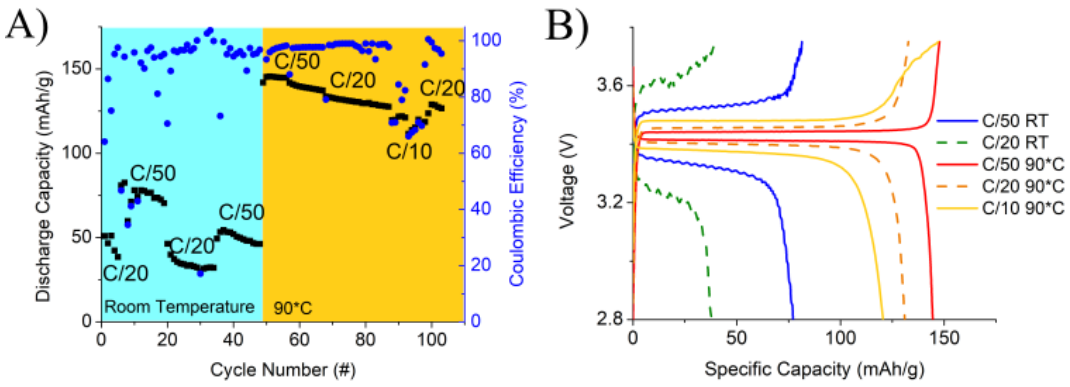

Figure 9. Galvanostatic cycling A) discharge-coulombic efficiency and B) voltage profile with cathode loadings of approximately 15 mg/cm^2. Unless stated otherwise all cycling is performed at 90°C.

3.2 Calendar Aging

To ensure normal leakage currents were not at fault for the issues described above, calendar aging was employed. This is used for understanding long-term stability of electrolyte systems, in which cells are charged and degradation, normally via open circuit voltage, is observed. As LFP has highly stable flat charge and discharge plateaus, a modified version of calendar aging is employed here where, though voltage decay is noted, discharge capacity is the key metric after periods of open circuit at 90 °C. While this loses the in-situ diagnostic ability of understanding expected discharge from voltage decay, it still provides insight into any leakage current and stability. Figure 10 displays 90 °C voltage profile, discharge capacity, coulombic efficiency, and voltage undergoing a series of open circuit potential times were performed ranging from 5 minutes, to one, two, and three day holds between charge and discharge cycles at a rate of C/20 and one open circuit 34-day hold during C/50 cycling. Discharge

capacity and coulombic efficiency quickly leveled off using the 5-minute hold, which was the standard hold time during cell cycling in this work. Extending hold time to a full 24 hours resulted in a small drop in capacity and coulombic efficiency which both leveled off quickly, and the 48-hour hold only further decreased the capacity and coulombic efficiency. Consecutive 72-hour holds resulted in much faster capacity decay per cycle than any of the previous hold-times. The large departure of 72-hour holds can be seen especially well when normalizing discharge capacity to that of the previous cycle under the same cycling profile.

Interestingly, the majority of this capacity loss was observed to be recoverable upon return to 5-minute holds. The recoverability of capacity indicates that the loss mechanism occurring during charged open current is not structural degradation of cathode, catholyte, garnet, or lithium. In fact, after a 34-day hold between C/50 cycling, which retained an impressive 87% of its charge, the following cycle had nearly the same capacity as the cycle before the over month-long hold. This charge stability at elevated temperature exceeds those of related systems using similar ionic liquid systems which have shown charge losses as high as 42% in 70 hours at 30°C or even a charge decay rate of 4.68% per hour at room temperature[111], [118] thanks to garnet blocking much of the leakage current.

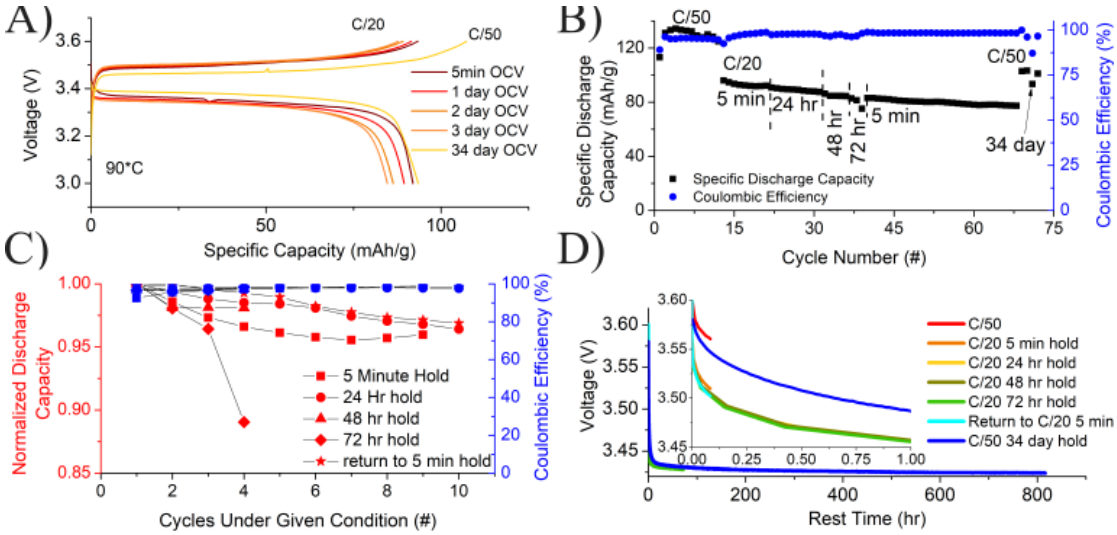

Figure 10. A) Voltage profile for bilayer cell cycling using 0.5 M LiTFSI in $Pyr_{14}TFSI$ with LFP loading in slight excess of 10 mg/cm^2 incorporating calendar aging tests, B) cycle life of said bilayer cell denoting the different holds, C) discharge capacity normalized to the previous cycle under the same conditions compared to Coulombic efficiency, and D) decay of open current voltage after charge. All cycling and open current experiments were performed at 90 °C.

3.3 I Utilizing EIS/DRT and SEM to Understand Internal Resistances and Cell Performance

Using references [119], [120] peaks around 10^1-10^2, 10^3-10^4, and 10^{-1}-10^1, can be attributed to Cathode-Electrolyte Interface (CEI), Cathode-Aluminum Interface (CAI), and cathode-electrolyte charge transfer, though these were using liquid electrolyte systems than reference. Furthermore, Bucshe et al identified peaks between 10^2-10^4 Hz to be related to the charge-transfer through Solid-Liquid Electrolyte Interface (SLEI) while using a different lithium ceramic electrolyte [102] [121]. Peaks around 0.1 Hz can be ignored in this work as Warburg tails were not removed before DRT analysis was performed. We can thus attribute the large peak around 1-2 kHz to be SLEI, while the peaks at 10^2, 3, and between 10^4-10^5 Hz can be attributed to CEI,

LFP-IL charge-transfer, and CAI respectively. This corroborates the interpretation from cycling data relating of resistance, and thus capacity and rate-performance, being tied with a relatively planar interface, namely that between garnet and the ionic liquid. The additional interface coming into play at higher loadings seems tied to either CEI or cathode-catholyte charge-transfer.

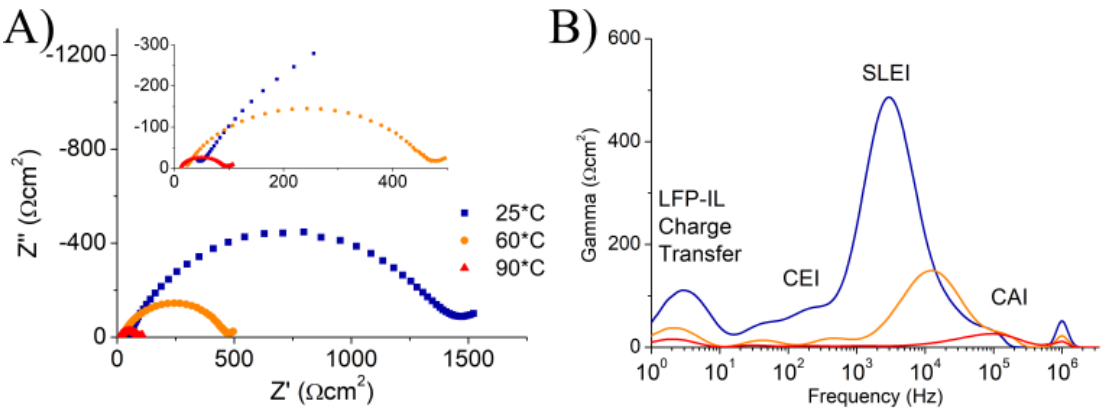

Figure 11. A) EIS and B) DRT of an LFP-0.5M LiTFSI Pyr_{14}TFSI-garnet bilayer-lithium metal infiltrated cell. Peaks identified via literature data.

A symmetric cell using 0.5 M LiTFSI in Pyr_{14}TFSI anolyte between lithium metal anodes and garnet surfaces was cycled. A step pattern was utilized with either time or voltage cutoff in place, where following the plating/stripping EIS was performed under the same current bias as the preceding cycling step. Figure 12A shows voltage response to current remains proportional through 0.5 mA/cm2 in the forward sweep where the voltage spiked to the cutoff voltage of 1.5 V. The resultant Nyquist plots in Figure 12B show high frequency regions remained largely static through this sweep while the middle frequency range appeared to expand and contract, with the EIS under 0.5 mA/cm^2 appeared to be little more than a Warburg tail. Interestingly, the subsequent reverse cycling showed a significant drop in resistance that is most apparent in the middle frequency range, as the data points were closer together than during the

forward cycle. Cycling in the reverse direction had issues at the same current as the forward, with a massive drop to near 0 volts indicating that lithium was no longer transported via ionic liquid. EIS further confirmed shorting as the subsequent Nyquist plot for 0.5 mA/cm^2 was far smaller and of a different shape than previous plots from the cell. The lithium-LFP cells of approximately 5 and 10 mg/cm^2 show similar behavior to the lithium symmetric cell, where issues begin around 0.5 mA/cm^2, further confirming the same interface, garnet-ionic liquid, as the main contributor to resistance.

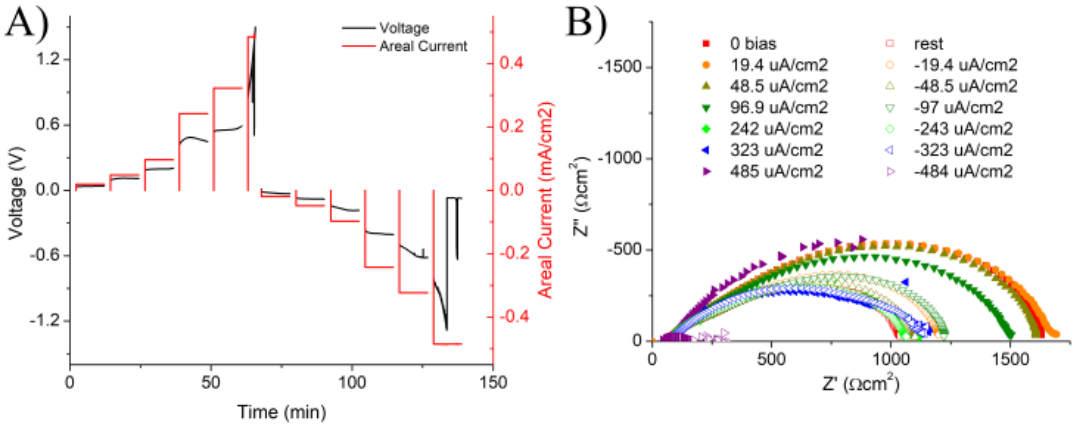

Figure 12. A) Cycling and B) EIS response to a set of currents in a symmetric cell with lithium electrodes, 0.5 M LiTFSI-Pyr$_{14}$TFSI intermediary, and dense garnet pellets.

In addition to the above impedance-derived understanding for cycling issues, greater understanding may be achieved through microstructural observation. Figure 13A displays the surface image of the dense layer in garnet bilayers similar to those used in the cells above; on the left side of this image one singularly large grain can be observed while the right side is composed of an array of grains both significantly above and below 10 µm. This non-uniformity in microstructure likely causes applied current to be unevenly distributed through the cell causing premature cell failure.

Furthermore, backscatter imaging of the same surface, as seen in Figure 13B, reveals that some of these large grains are a secondary phase, discernable through the brightness of these grains which lie on top of the darker dense layer. The EDS spectra from this secondary phase, in Figure 13C, indicates the secondary phase to be overwhelmingly lanthanum and oxygen rich. Some carbon and a small amount of zirconium also appear to be present in the secondary phase. Beyond further disrupting the uniformity of current through the cell, these materials could prove harmful to cell performance through additional avenues. Most studies report the band gap for La_2O_3 within a range in excess 5 eV, though Gu et al have measured values as low as 3.61 eV [122], [123], [124], [125], [126], the latter of which is similar to the voltage in Figure 9D where the polarization of the cell was interrupted. More troubling still is that certain dopants, and explicitly zirconium, have been shown to decrease band gap as has incorporation of carbon in the form of La_2CO_5 [122], [124], [125]. If formed into a sufficiently continuous network through the dense garnet, and not only on top of the cathode-side, an electronically conductive network could create significant leakage current at the proper voltage. Furthermore, La_2CO_5 has been shown to catalyze a number of reactions and could catalyze degradation reactions of the catholyte[124], [127], [128], [129], [130]

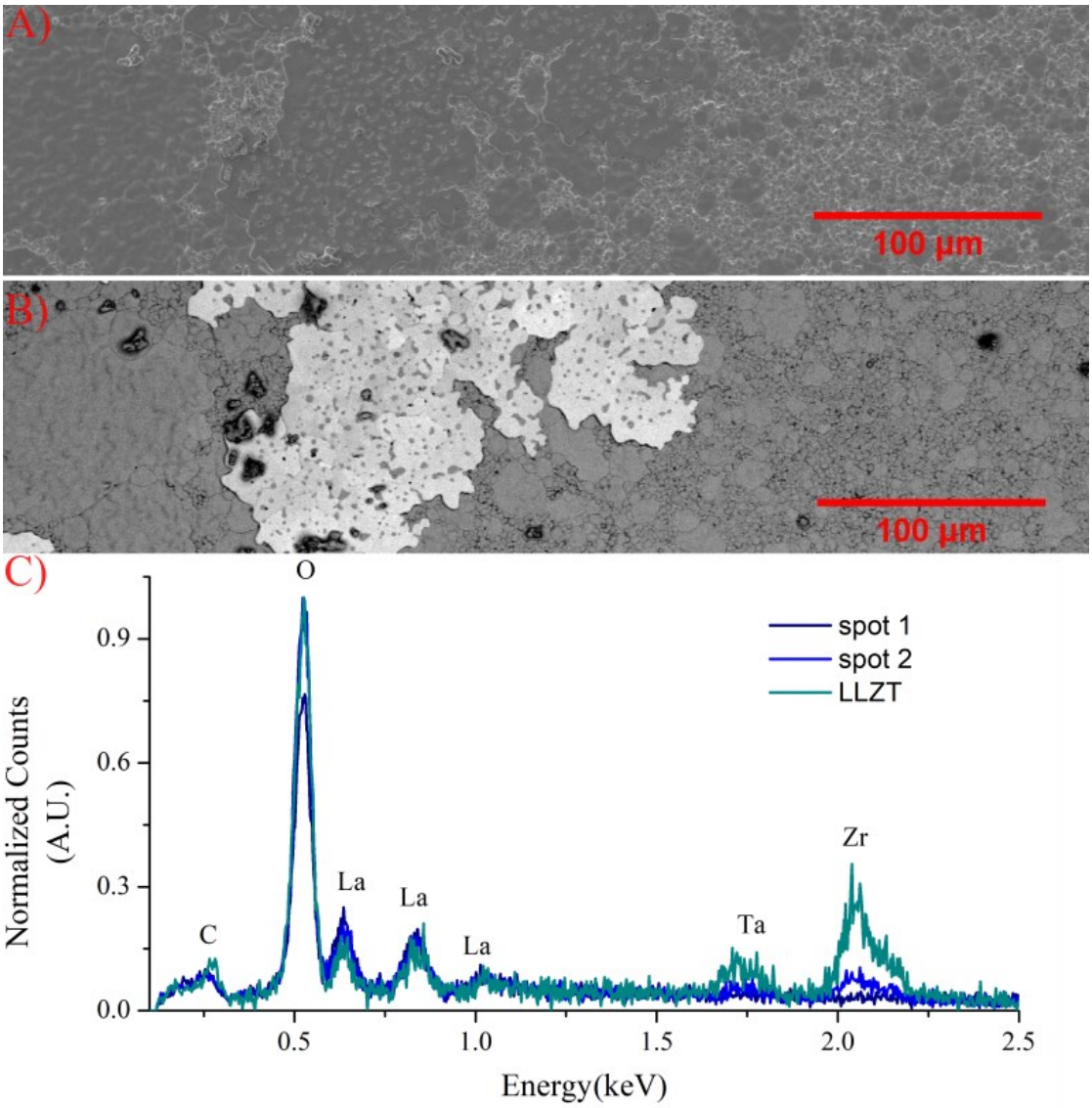

Figure 13. SEM surface-images of LLZT bilayer using A) scanning electron and B) back-scatter modes, with C) EDS from the brighter phase observed in backscatter.

3.4 Interfacial Modification

3.4.1 Microstructure

Figure 14A shows common garnet bilayer structure previously used in this work, where strong intergranular bonding is observed in the dense layer via the

prevalence of intragranular fracture. Similarly, Figure 14B shows that most of the dense layer in the modified bilayer retains this strong intergranular bonding. On top of this layer an approximately 3 µm layer of grains, as measured by ImageJ [115], is observed where fracture occurs between grains. [25]As the surface SEM shows in Figure 14C and D, the interlayer created a more uniform interface of smaller grain size which in turn should increase surface area.

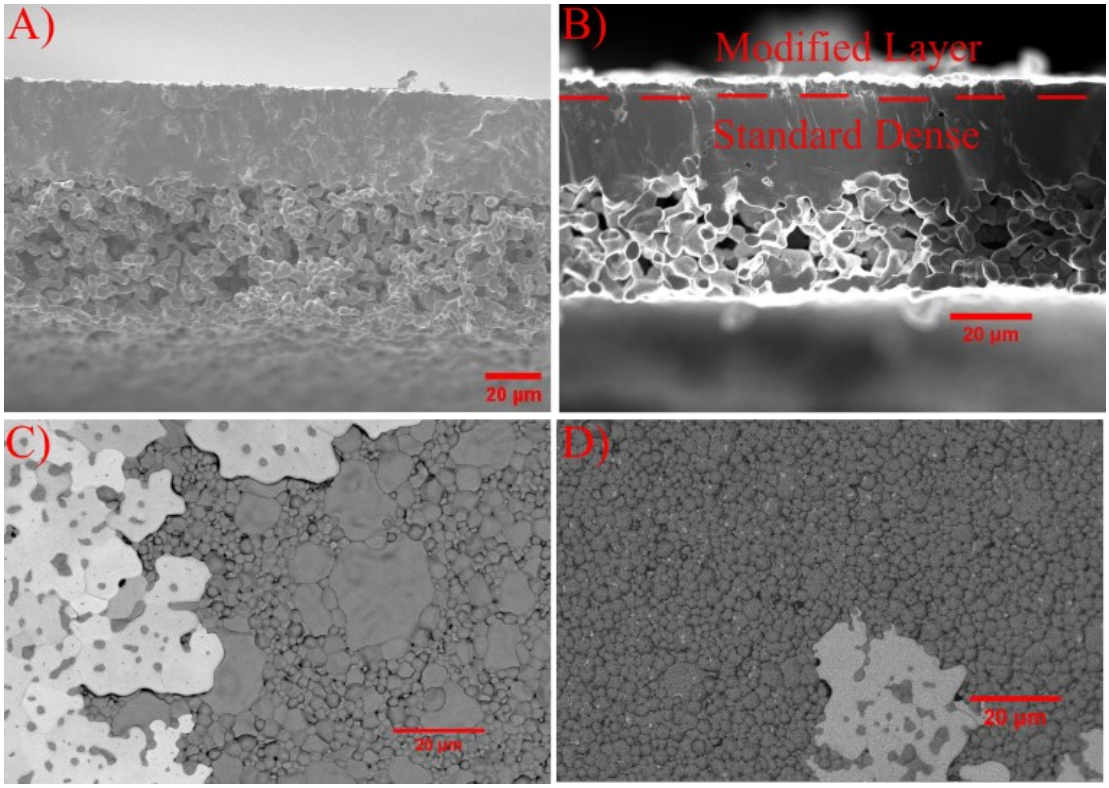

Figure 14. Profile SEM of A) standard garnet bilayer and B) with the modified garnet interface. Top-down SEM of dense layer surfaces for C) standard garnet bilayer and D) modified bilayer. Scalebar for all images is for 20 µm.

3.4.2 Impedance and Cell Performance

Comparing the Nyquist plots of EIS for the non-modified and surface-modified garnet in Figure 11A and Figure 15A respectively, a visibly clearer separation of

impedance arcs exists in the middle-frequency region: a region previously correlated with the time domain of SLEI. Initially, at room temperature, this normalized peak is also of a similar height as the other cell. Upon heating of the cells to 60°C, normalized cell resistance drops by a factor of three for the bilayer garnet cell, while the modified garnet results in a 10x reduction. This is accompanied by a much more drastic reduction in SLEI DRT peak, along with blue-shifting of the peak to higher frequency. Further increasing cell temperatures to 90°C, further 5x reductions in resistance are observed, with continued blue-shifting of resistance arcs.

Cycling for the modified cell displays higher specific discharge capacity than observed in any of the previous cells with 162 and 157 mAh/g at C/50 and C/20 respectively. Interestingly, the capacity at C/50 continued to increase for several cycles, possibly indicating a continued wetting of interfaces or slow change of interfacial composition. At increased rates, this performance boost continues as at C/5 the modified-bilayer cell has >15% higher capacity, increasing from 107 to 125 mAh/g, than the unmodified electrolyte of similar cathode loading of approximately 10 mg/cm^2. After further widening of the voltage window to 4.25-2.75 V, the cell regularly maintains >100 mAh/g despite cycling at 0.49 mAh/cm^2 (C/3). Upon returning to initial voltage window and C/20 cycling, the cell returned to discharge capacity of 120 mAh/g and stable coulombic efficiency of 96.7%. This stabilization of coulombic efficiency post high-rate cycling is a significant departure from cells with unmodified interface, which were unable to restabilize coulombic efficiency.

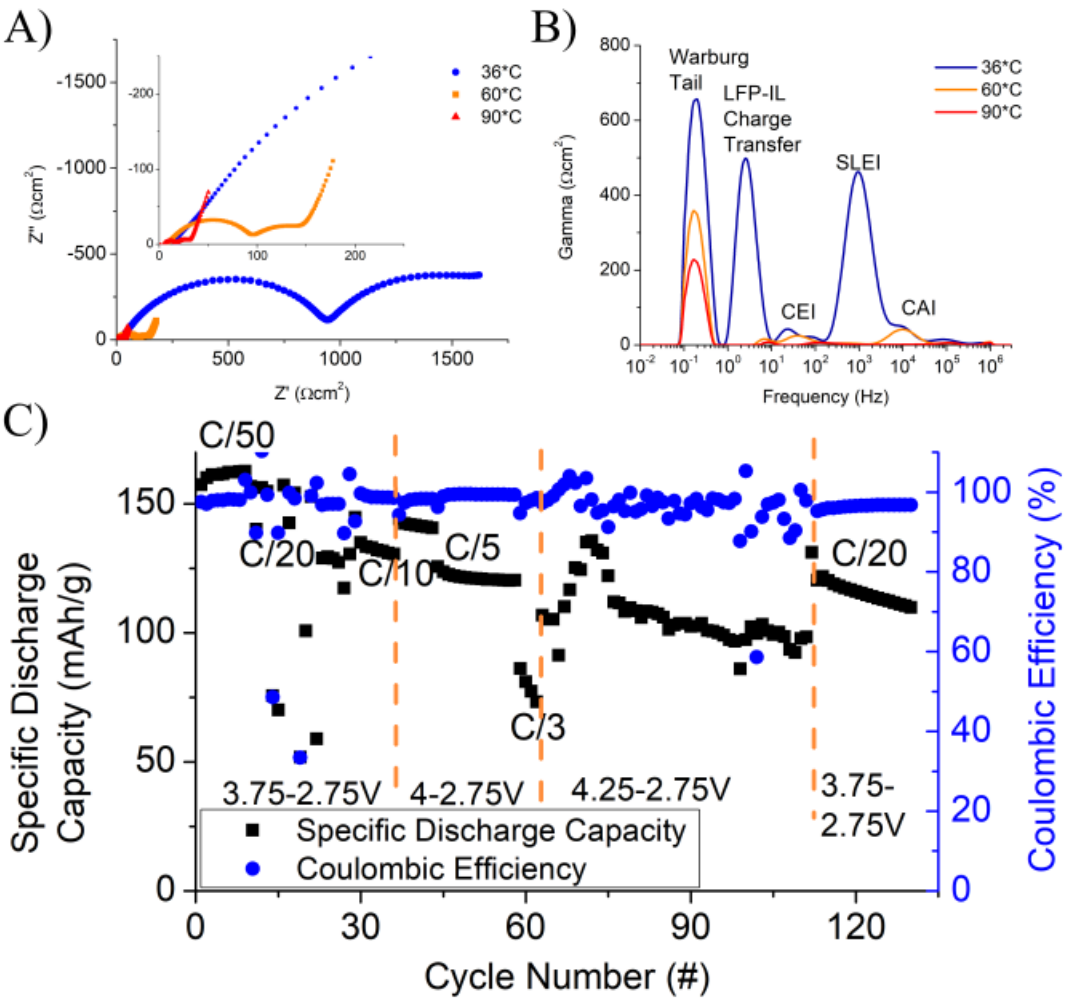

Figure 15. A) EIS, B) DRT, and C) cell cycling for an LFP-0.5 M LiTFSI $Pyr_{14}TFSI$-modified garnet bilayer-lithium metal infiltrated cell.

C-rates achieved in this work are notably lower than most garnet-based cells with LFP cathodes from literature in Table 1. However, the areal rate reached in this work was equal or greater than most of those same cells while largely maintaining the same capacities seen for similar areal rates. This discrepancy between areal and C-rate largely falls in line with previously mentioned observations in this work: the strong effect of cathode loading on cell resistances and thus rate capability. Two papers did achieve significantly higher areal rate through the combination of differing catholytes changing solvent-surface interfaces and reactions and much lower cathode loadings

resulting in lower resistance and less time under highly polarizing environments. Notably both of these papers featured catholytes of much higher lithium salt concentrations.

Table 1. Garnet batteries of various catholytes and modifications and the metrics, such as rate, loading, and capacities, achieved for various with LFP cathodes found in literature and this work. All values were either given in the papers referenced, their supplemental information, or back-calculated from informaiton given.

Reference	Active loading (mg/cm^2)	Maximum C-rate-Areal Rate (mA/cm^2)	Highest Capacity/ High-rate Capacity (mAh/g)/ High rate total capacity (mAh/cm^2)	Temperature (°C)	Catholyte/ garnet modifications
[131]	3-3.5	2C-1	144/110/0.3575	Room Temperature	2M LiFSI in $Pyr_{13}FSI/SnF_2$
[132]	1.17	C-0.2 8C-1.6	150/100/0.117 126/78/0.09126	60 100	LiTFSI-PVDF (40:15:10:35 LFP: ketjen black: PVDF: LiTFSI)
[133]	2	C/2-0.17	161.4/153.6/0.3072	80	PEO-PVDF-LiTFSI/ Polydopamine coating
[134]	8.8	C/10.7-0.14	158/158/1.3904	Room Temperature	1M $LiPF_6$ EC and DMC (40µL)/Glass fiber separator
[135]	1.2	3C-0.61	118/47.8/0.05736	25	1M $LIPF_6$ EC and DEC (10µL)/Co_3O_4
[136]	5	C/5-0.17	150/149.5/0.7475	Room Temperature	3uL "Carbonate electrolyte"/NH_4F
[137]	2.45	C/2-0.21	148/148/0.3626	Room Temperature	1M $LiPF_6$ EC and DEC (10µL)

					Mxene reacted Li
[138]	1.17	C-0.2	147/118/0.13806	60	PVDF/PEO/LiTFSI
[71]	2.5	C/1.7-0.25	145/112/0.28	25	0.2 LiTFSI-0.8Pyr_{14}FSI 2μL/cm^2
This work	4.9	C/1.6-0.52	157/157/0.769	90	0.5M LiTFSI in Pyr14TFSI, 1μL:1mg LFP/ALD coating
This work	9.8	C/3-0.54	150/91/0.892	90	0.5M LiTFSI in Pyr14TFSI, 1μL:1mg LFP/ALD coating
This work	8.6	C/3-0.49	162/135/1.16	90	0.5M LiTFSI in Pyr14TFSI, 1μL:1mg LFP/Small grain interface and ALD coating
This work	14.6	C/20-0.125 C/10-0.25	82/50/0.73 145/119/1.737	22 90	0.5M LiTFSI in Pyr14TFSI, 1μL:1mg LFP/ALD coating

3.5 Conclusions

Hybrid solid-ionic liquid lithium metal-LFP cells were assembled and tested by wetting the cathode and planar garnet with ionic liquid as a catholyte, while porous layers in garnet bilayers were infiltrated with lithium. By varying cathode loading and cell temperature and cross-comparing with lithium symmetric cells of similar hybrid electrolyte, the catholyte-garnet interface was determined as a main contributor to cell resistance through EIS and DRT, especially up to 10 mg/cm^2 loading above which

cathode-catholyte interfaces also contribute significantly to cell resistance. High utilization of LFP was achievable at elevated temperature, though rate-capability remained constricted by the aforementioned interface. Garnet microstructure on this interface was successfully modified to create smaller, more uniform garnet grains resulting in improved capacity, rate performance, and coulombic efficiency. The high room temperature resistance of these modified cells seems to indicate increased wetting issue between ionic liquid and garnet due to the rougher surface, while at elevated temperature this issue was rapidly reduced.

Chapter 4: Leveraging Bonding-Interface Relationship in ionic liquid-lithium garnet quasi solid state batteries to improve rate capability

4.1 Symmetric Cell EIS-DRT

The ionic liquid 0.5M LiTFSI in $Pyr_{14}TFSI$ system was used as a baseline catholyte in a symmetric LFP-Catholyte-LLZTO-Catholyte-LFP cell. The EIS shows a slow decrease in resistance over the first 90 hours which then stabilizes, as seen in Figure 16. This likely indicates a slow continued wetting process of the garnet related to the high viscosity of ionic liquids.

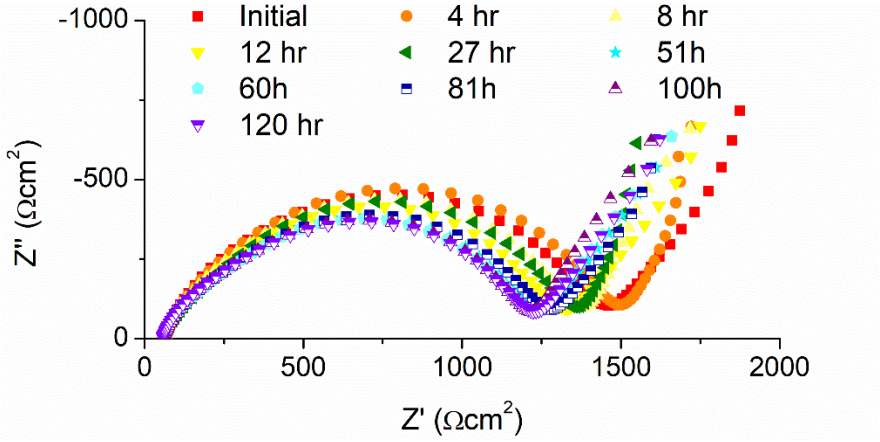

Figure 16. EIS taken of symmetric LFP-0.5M LiTFSI-$Pyr_{14}TFSI$-LLZ cell for 120 hours.

Peak frequencies from the DRT in Figure 17C were assigned based on those observed in literature in related systems: with Cathode-Aluminum Interface (CAI) around 10^4 Hz, Solid-Liquid Electrolyte Interface (SLEI) 10^2-10^4 Hz, Cathode-Electrolyte interface (CEI) 10^1-10^2 Hz, and cathode-electrolyte charge transfer 10^{-1}-10^1 Hz [102], [104], [119], [120]. In line with our work from the previous chapter, the solid-

liquid electrolyte interphase (SLEI) is the largest contributing peak observed in DRT as the extreme low frequency peak observed is attributed to Warburg diffusion.

Addition of triethyl phosphate (TEP) significantly increased the initial resistance of the cell compared to the baseline system, though after aging for 93 h its resistance decreased as seen in Figure 17. A slight red-shift is observed in the SLEI peak when adding TEP as a co-solvent, however there is a blue-shift for the IL-LFP charge transfer peak. Cathode electrolyte interface (CEI) for TEP co-solvent appears roughly at the same frequency as observed in Figure 17C where the peak is well resolved for the standard liquid.

The symmetric cell with acetonitrile (ACN) co-solvent initially has lower resistance than the standard IL as seen in Figure 17A. However this value more than doubled over the course of testing when compared to Figure 17B. After aging 81 h, a new high frequency loop is observed in the Nyquist plot, indicating a new electrochemical process. The increase in ohmic impedance possibly indicates instability resulting from the acetonitrile itself or its contact with garnet. Resolving the peaks using DRT in Figure 17C, a red-shift of all major liquid-related interfacial peaks is observed for the final EIS compared to the sample with no ACN co-solvent.

LiTFSI concentration similarly led to large shifts observed via EIS and DRT, with lower concentrations resulting in significantly higher resistance. Comparing the EIS spectra for 0.5M vs 1M from Figure 17A and B, it is quickly apparent that in addition to the reduced total impedance a significant amount of blue-shifting must occur as a result of the increased lithium concentration from the much longer Warburg tail given its density of data points. DRT largely confirms this, as most peaks displayed

significant blue shifting. The SLEI peak, while of lower magnitude, was slightly red-shifted.

To further simulate real cell interfaces, samples using 0.5 M LiTFSI in Pyr14TFSI with and without TEP co-solvent were chosen to compare carbonate free, ALD coated garnet due to the apparent instability ACN co-solvent displayed in symmetric testing. EIS in Figure 17A and B displays for these samples far less change than their uncoated counterparts, with resistances only slightly higher than the final values for the uncoated samples. This likely indicates faster wetting of the garnet on ALD coated surfaces with increased resistance from the additional region at the solid-liquid interface for the lithium ion to traverse. Slight red-shifting is observed via DRT for both ALD coated samples in comparison with their uncoated counterparts, again unsurprising given the additional interlayer from ALD.

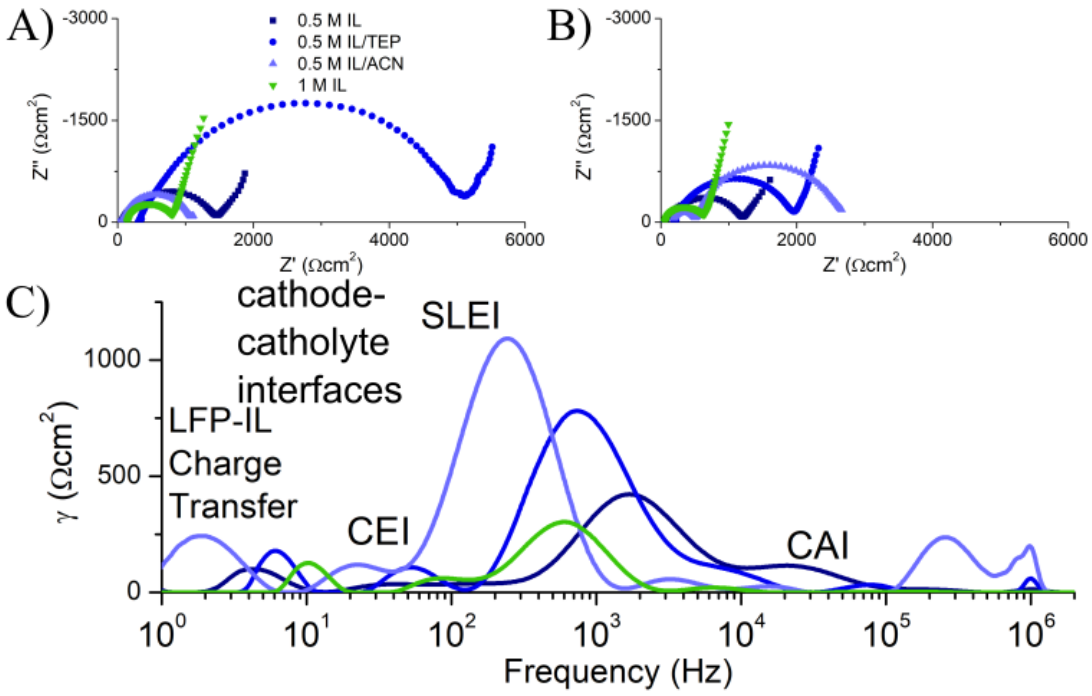

Figure 17. Nyquist plots from symmetric cells using LFP electrodes, garnet middle electrolyte, and catholytes specified at A) initial and B) final EIS and C) DRT of the same.

Closer examination of the high frequency regime, such as displayed in Figure 18, grant insight into the liquid catholytes themselves in addition to the interfaces previously discussed. X-intercept from this plot was taken to be the catholyte conductivity and complied in Table 2. The baseline catholyte displays no change in conductivity over the test. Catholytes with added TEP, ACN, and increased lithium concentration displayed conductivity loss during testing, as did the baseline catholyte

with ALD coated garnet. Interestingly, the sample with both ALD coated garnet and TEP additive did not lose conductivity loss.

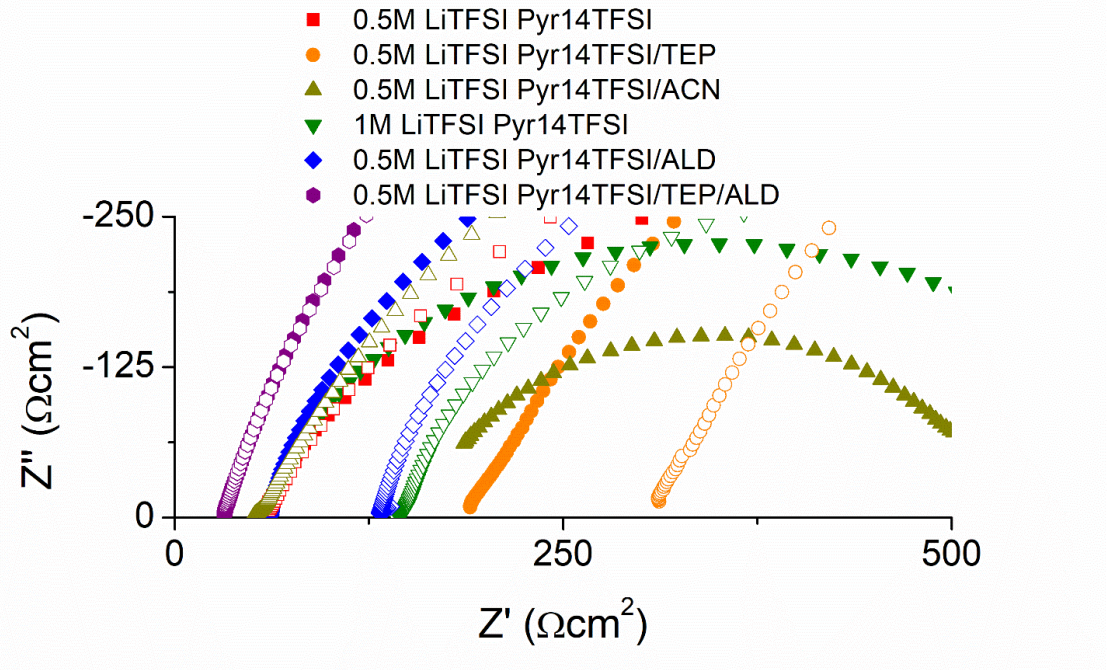

Figure 18. Expanded view of EIS comparison for LFP symmetric cells, filled in markers indicate initial scan while hollow markers indicate final scan. Inductive data points a high frequency removed.

Table 2. Initial and final x-intercept values for catholytes tested in LFP symmetric cells.

Baseline Catholyte	Modification	X-intercept initial (Ωcm^2)	X-intercept Final (Ωcm^2)
0.5 M LiTFSI Pyr14TFSI		65	65
0.5 M LiTFSI Pyr14TFSI	Triethyl phosphate 10%	190	310
0.5 M LiTFSI Pyr14TFSI	Acetonitrile 10%	65	185
1 M LiTFSI Pyr14TFSI		65	150
0.5 M LiTFSI Pyr14TFSI	ALD coated garnet	65	130
0.5 M LiTFSI Pyr14TFSI	Triethyl phosphate 10%, ALD coated garnet	50	50

Comparing NMC to LFP cathodes in symmetric cells with 0.5M LiTFSI Pyr_{14}TFSI catholyte results in dramatic shifts in both shape and magnitude of the observed impedance, with the NMC cell in Figure 19 having significantly lower total impedance than its LFP counterpart. SLEI peak position, compared in Figure 19C, has small frequency red-shift when changing to NMC cathode. However, the CEI dramatically blue-shifts for the NMC sample to the point that peak overlap between SLEI and CEI becomes very significant. A similar significant blue-shift occurs for the ionic liquid-cathode charge transfer peak. Introduction of the fluoro-ethers BTFE and OFPTFE, at the same Li:Pyr_{14} ratio as the reference catholyte system, returned the SLEI peak position to the frequency observed for the baseline IL-LFP sample in Figure 19C, indicating that the apparent red-shift for NMC could have been related to its convolution with CEI. Increasing lithium concentration for OFPTFE diluted catholyte resulted in similar blue-shifting as observed previously in the LFP DRT. Changing dilutant from OFPTFE to BTFE at the same concentrations resulted in even greater CEI-SLEI peak convolution.

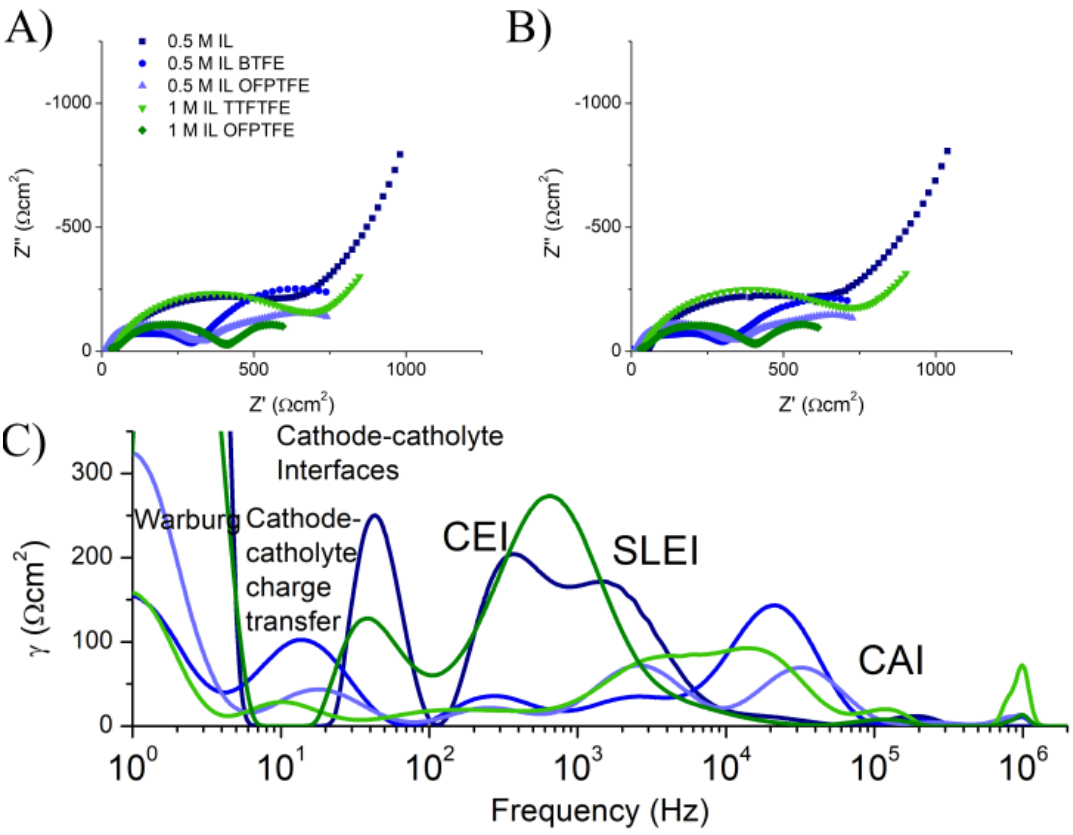

Figure 19. A) initial EIS, B) final EIS, and C) DRT from symmetric NMC-catholyte-garnet cells.

Focusing on x-axis for fluoroether diluted catholyte with gives similarly useful insight as the co-solvents with LFP. The baseline catholyte, again 0.5 M LiTFSI in $Pyr_{14}TFSI$, initially had an x-intercept of 48 Ωcm^2 which had decreased to 38 Ωcm^2 by the end of testing. All of the tested fluoro-ether diluted catholytes displayed initial resistances less than this with BTFE and OFPTFE at 18 and 12 Ωcm^2. The BTFE sample did not show significant change in this value while the OFPTFE sample underwent a slight reduction of resistance to 10 Ωcm^2. T As seen previously in the LFP experiments, higher lithium concentration to 1 M from 0.5 M often led to larger x-intercept values, with TTFTFE having the lowest observed diluted catholyte conductivity, around the same final value, 40Ωcm^2, as that of the

non-diluted 0.5 M LiTFSI sample. OFPTFE x-intercept is not directly observed at this salt concentration, though it would be less than the baseline catholyte tested as seen in Figure 20.

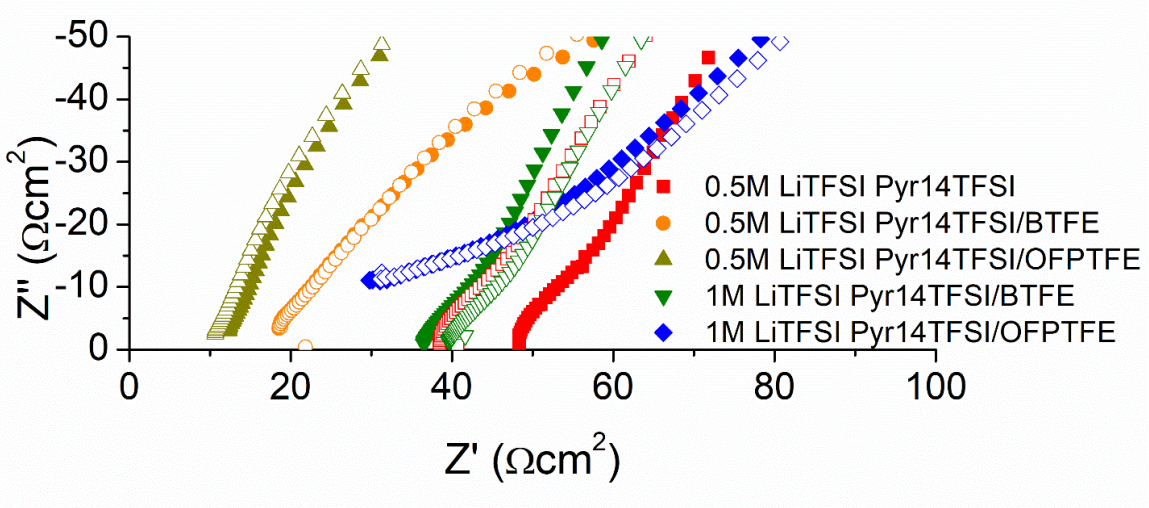

Figure 20. Expanded view of EIS comparison of catholytes for NMC symmetric cells, filled in markers indicate initial scan while hollow markers indicate final scan.

Table 3. Initial and final x-intercept for catholytes tested in NMC622 symmetric cells.

Baseline Catholyte	Modification	X-intercept initial (Ωcm^2)	X-intercept Final (Ωcm^2)
0.5 M LiTFSI Pyr14TFSI		48	38
0.5 M LiTFSI Pyr14TFSI	BTFE 10%	18	18
0.5 M LiTFSI Pyr14TFSI	OFPTFE 10%	12	10
1 M LiTFSI Pyr14TFSI	BTFE 10%	37	40
1M LiTFSI Pyr14TFSI	OFPTFE 10%	25	25

4.2 Raman and CV

To better understand the physical changes occurring to catholyte with varied salt or co-solvent addition, Raman spectroscopy was used to observe the Li coordination states. Figure 21 shows the peaks around 740-705 cm^{-1} which is related

to $TFSI^-$ bonding state through a series of internal bonds[139], [140], [141], [142]. As the LiTFSI concentration increases, a shift from "free" $TFSI^-$ to Li^+ bound $TFSI^-$ can be observed. At 0.5 M LiTFSI, the electrolyte displays a splitting of this peak, which by 1 M becomes a nearly even split. However, introduction of TEP results in only the "free" $TFSI^-$, indicating a preferred coordination of Li^+ with TEP over $TFSI^-$. Similarly, increasing the salt concentration of this co-solvent system to 2 M LiTFSI from 0.5 M, a Raman spectrum nearly identical to the 1.5 M LiTFSI system without co-solvent is observed. Comparing this to the EIS observed, high levels of Li^+-$TFSI^-$ coordination resulted in lowered resistances of cells. Thus, introducing co-solvents offers competing bonding states which most often result in more difficult charge transfers within the system. Addition of fluoro-ether however did not result in Raman peak shifting as expected.

A trend can be observed between the interfacial resistances of IL systems with the solvation within these catholytes. With increasing Li^+ concentration, the peak shifts from the lower wavenumber peak to high the one at higher wavenumber, indicating that $TFSI^-$ is bound more strongly to Li^+ than Pyr_{14}^+. The introduction of TEP and ACN offered competing solvation states for Li^+ that shift the $TFSI^-$ bonding away from Li^+, indicating that the co-solvent bonds offer lower energy state for Li^+ coordination. Similarly, these additions caused the solid-liquid electrolyte interface to shift significantly to lower frequencies. It would thus seem that these solvents, more strongly bonded to the lithium ion, were thus inhibiting transfer at the solid-liquid electrolyte interface.

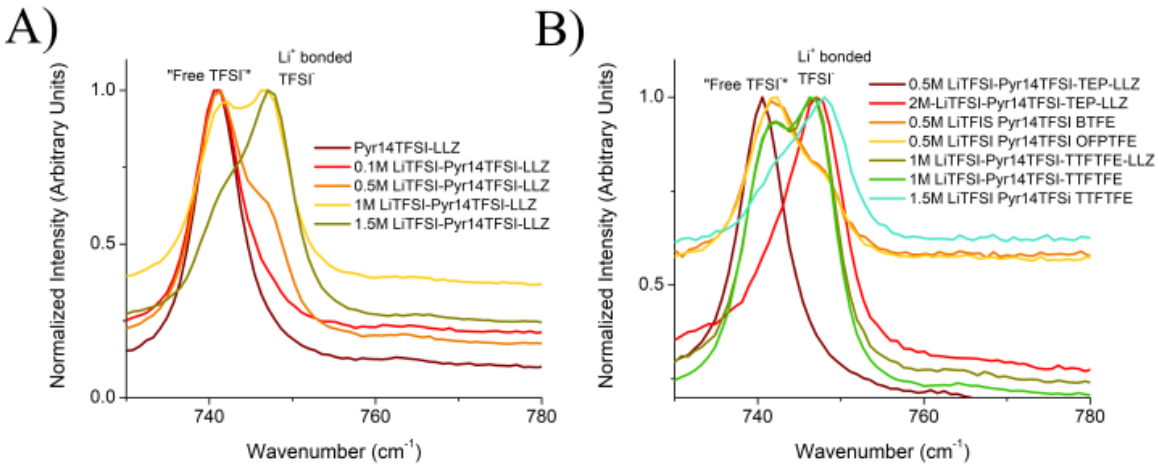

Figure 21. Raman spectroscopy for the peaks around 740-750cm-1 related to TFSI- bonding for select electrolytes, with LLZ denoting presence of garnet for A) changing salt concentration with no solvent additives and B) with solvent additives.

Cyclic voltammetry (CV) of these electrolytes produced particularly interesting results during the anodic portion of the voltage sweep. The standard 0.5 M LiTFSI in $Pyr_{14}TFSI$ displayed an elevated current response above ~3.5 V before the more obvious breakdown voltage between 4.5-5 V. Introduction of TEP delayed the initial current increase to ~3.7 V, though its breakdown voltage response occurs slightly before that of the standard ionic liquid. BTFE, the most commonly used fluoroether for localized high concentration electrolytes, displayed similar voltage response to the standard ionic liquid while OFPTFE actually appears to have suppressed the initial voltage increase. Similarly, increased LiTFSI concentration suppressed the lower voltage response with 1.5M not displaying any increased response until 4.7 V. At 1 M LiTFSI the lower voltage response in suppressed completely with TTFE, while a small remnant of this response remains with TEP at 1M. Similar results can be observed for the cathodic sweep of the CV; higher LiTFSI concentration decreases the voltage at which breakdown is observed with minimal change from fluoroether addition. Cathodic sweeps for TEP co-solvents did display additional peaks indicating less

stability to lithium metal. This should have minimal impact in the full cells to be tested as garnet should largely shield electrolyte from much of the lower voltages.

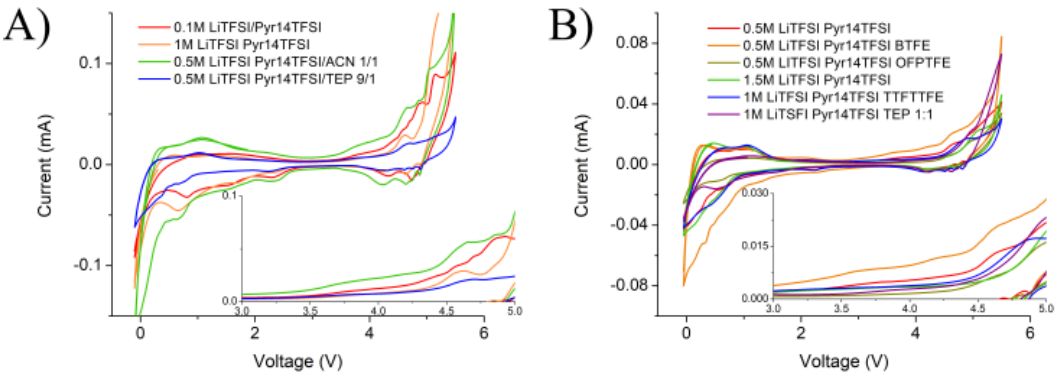

Figure 22. Cyclic voltametric for various electrolytes using glass fiber separator, aluminum current collector and A) lithium or B) copper counter electrode.

Introduction of LiTFSI into $Pyr_{14}TFSI$ results in significant increase in viscosity: from 94 cP, as reported by the manufacturer, to 190-170 cP at 0.5 M LiTFSI, and 199-196 cP at 1 M (Figure 23). Addition of 10 volume percent TEP significantly reduced the viscosity to 54-38 cP at 0.5 M LiTFSI. Addition of fluoroethers resulted in similar viscosities at the same concentration, with BTFE and OFPTFE at 115 cP and 113 cP, respectively, at 3 RPM. Increasing lithium concentration to 1 M with TTFTFE raised viscosity to 140-132 cP, well above the 0.5 M samples with co-solvent or dilutant but significantly less than the undiluted electrolyte of the same concentration.

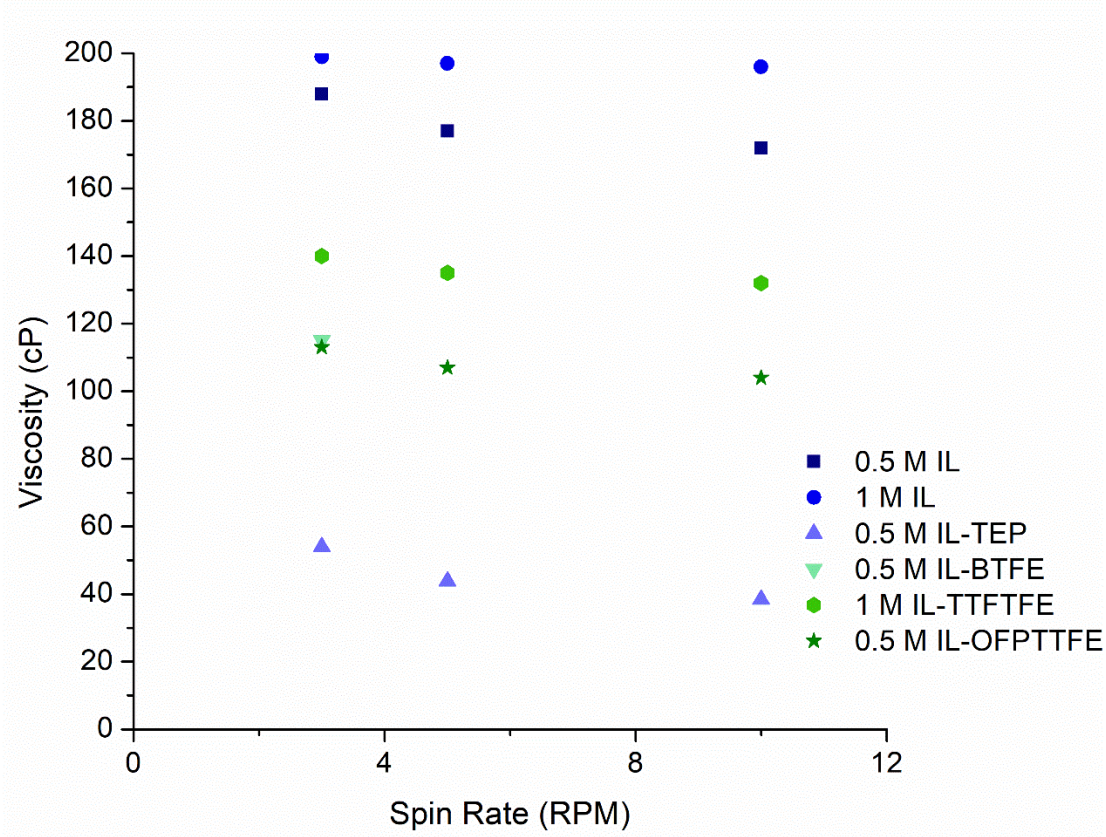

Figure 23. Viscosity of ionic-liquid based catholytes tested (0.5 M Pyr14TFSI, 1 M Pyr14TFSI, 0.5 M Pyr14TFSI-TEP, 0.5 M Pyr14TFSI-BTFE, 1 M Pyr14TFSI TTFTFE, and 0.5 M Pyr14TFSI-OFPTTFTFE) over a series of spin rates.

4.3 Full Cells

Full cells with LFP cathodes and Li metal anodes were made using ALD-coated trilayer garnet and 0.5 M LiTFSI electrolyte with TEP co-solvent. These cells benefited from the fast electrolyte wetting observed from ALD coated garnet and lower viscosity of TEP cosolvent catholyte. Figure 24A and B shows the high capacity, 158 and 160 mAh/g at 60°C and 90°C respectively, and high-rate capability in Figure 24E, tested to 1 C or 2.26 mA/cm^2. Even at a high rate of C/2 (1.13 mA/cm^2) the cell maintained >100 mAh/g. Interestingly, while displaying slightly higher initial capacity at 90°C than 60°C the performance became slightly less stable over the tested range. While resulting in temporary large loss of capacity, the cell was cycled all the way to 2.26 mA/cm^2

corresponding to 1 C. Even after pushing to this extremely high areal rate for a garnet-based cell, capacity was able to recover immediately to 140 mAh/g at C/20 cycling, and again to 130 mAh/g even after cycling again at room temperature and 60°C. In the voltage profiles from Figure 24D the effect of polarization, especially on the discharge, can be seen as the plateau becomes more curved until the plateau virtually disappears around C/1.5 (1.5 mA/cm^2). The difference in cycles with low coulombic efficiencies can also be observed through the charge profile. The initial C/3 (0.75 mA/cm^2) cycle looks similar to previous cycles with a clear plateau before the cell polarizes, but the final C/3 cycle shows this knee with a second inflection point causing the voltage to level back out.

Comparing the voltage profiles and EIS from Figure 24A and C at the three temperatures tested can help explain cycling behavior. The combination of increased surface area with lower viscosity and easier wetting is immediately apparent from the cells much lower room temperature resistance. However, room temperature cycling displayed much higher overpotential than the elevated temperature cycling, as it had 3x and 6x the resistance observed at 60°C and 90°C. This higher resistance in combination with the catholyte viscosity and added diffusive length through the garnet's porous layer contribute to the cell's quick polarization at room temperature. For the elevated temperature disparity of higher capacity decay at lower resistance, a possible answer can be found in comparing the charge cycles. While overpotential is slightly lower at 90°C than 60°C, the polarization dominated portion of cycling appears to be the domain where the extra capacity is derived. Thus the cells spend longer times

at more extreme voltages, where the cyclic voltammetry previously displayed a slight current response.

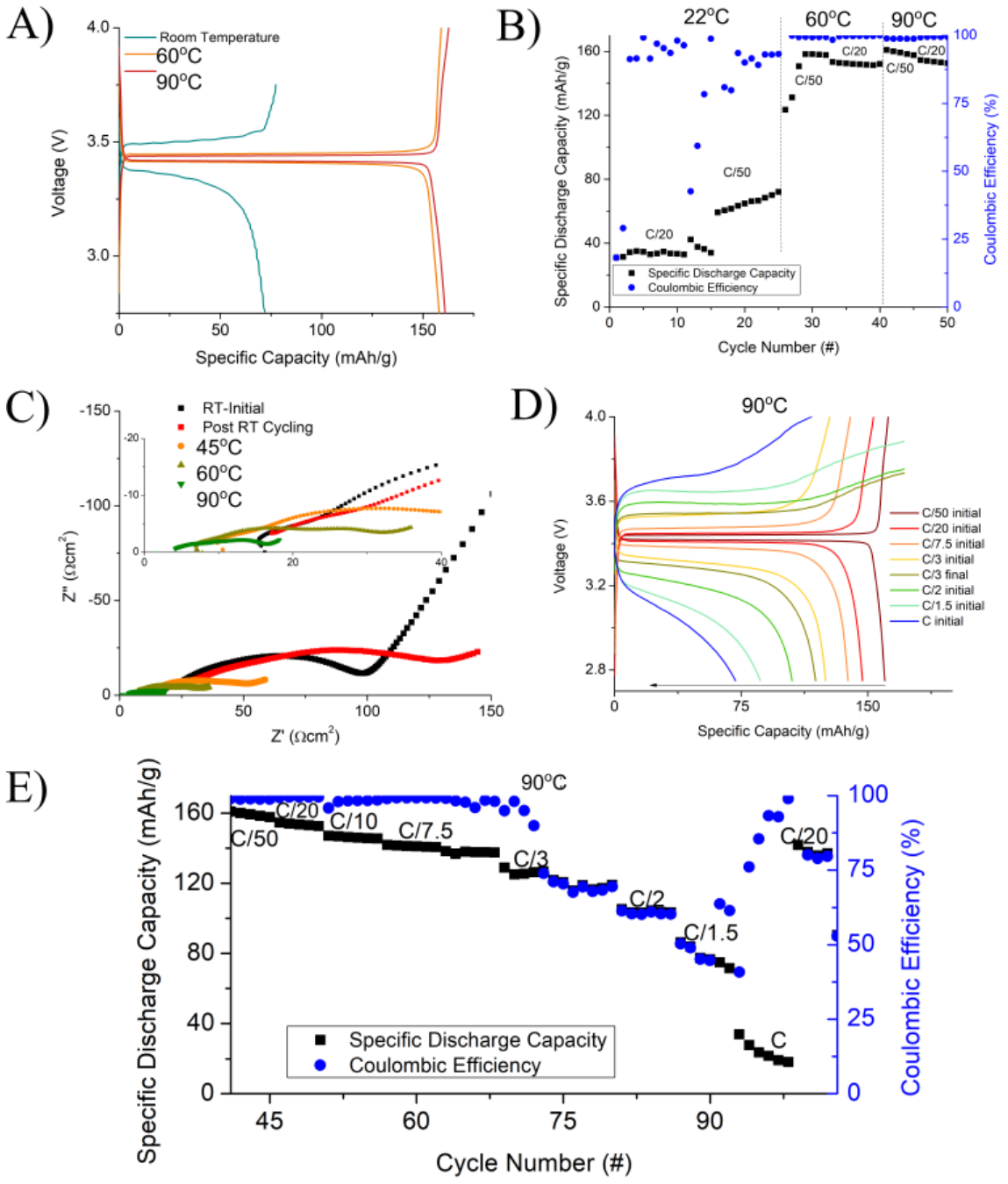

Figure 24. A) EIS over a series of temperatures, B) voltage profile at varied temperature for C/50 rate, C) discharge-coulombic efficiency for Li-trilayer garnet-IL/TEP-LFP cell for varied temperature cycling at C/50 and C/20 D) voltage profile

at varied cycling rates at 90℃, and E) discharge-coulombic efficiency cycling for the same cell at 90℃.

The shape of the Nyquist plots, aside from the total resistance, from trilayer garnet with 0.5 M LiTFSI-Pyr14TFSI-OFPTFE catholyte and NMC catholyte remained largely similar throughout a temperature sweep from room temperature in Figure 25A. One exception occurs at the higher frequencies tested, where before cycling and again upon reaching 40℃ and above, the beginnings of a Warburg tail appears to start that absent post room temperature cycling and at 30℃. This taken along with the wider separation of data points in this regime indicate that this cell's resistance is no longer dominated by garnet-catholyte interface, but those around catholyte-cathode interaction. As shown in Figure 25B, DRT confirms this interpretation of EIS showing major peaks in the frequency ranges previously attributed to CEI and catholyte-cathode charge transfer.

Room temperature cycling of this cell displayed respectable capacity in Figure 25 C&D, nearly 120 mAh/g on discharge for the first cycle, for garnet-NMC cells with a relatively high loading of 11 mg/cm^2. Unfortunately, both the coulombic efficiency and capacity at room temperature were unstable. Increasing temperature to 45℃ and lowering the discharge window to 2.7 V from 3 V resulted in the cell displaying highly stable coulombic efficiency and achieving the cathode manufacturer's expected capacity of 170 mAh/g. Increasing rate to C/20 (~0.1 mA/cm^2) decreased capacity to ~160 mAh/g but remained fairly stable. Further pushing to rates to C/10 and C/5 (approximately 0.2 and 0.4 mA/cm^2) resulted in more significant capacity losses, though initial capacities of 138 and 87 mAh/g were still achieved on respective initial cycles. During the C/5 cycling an instability in coulombic efficiency was observed,

though this instability was largely removed when slowing rate back to C/20 despite a more significant capacity decay than previously seen at this rate.

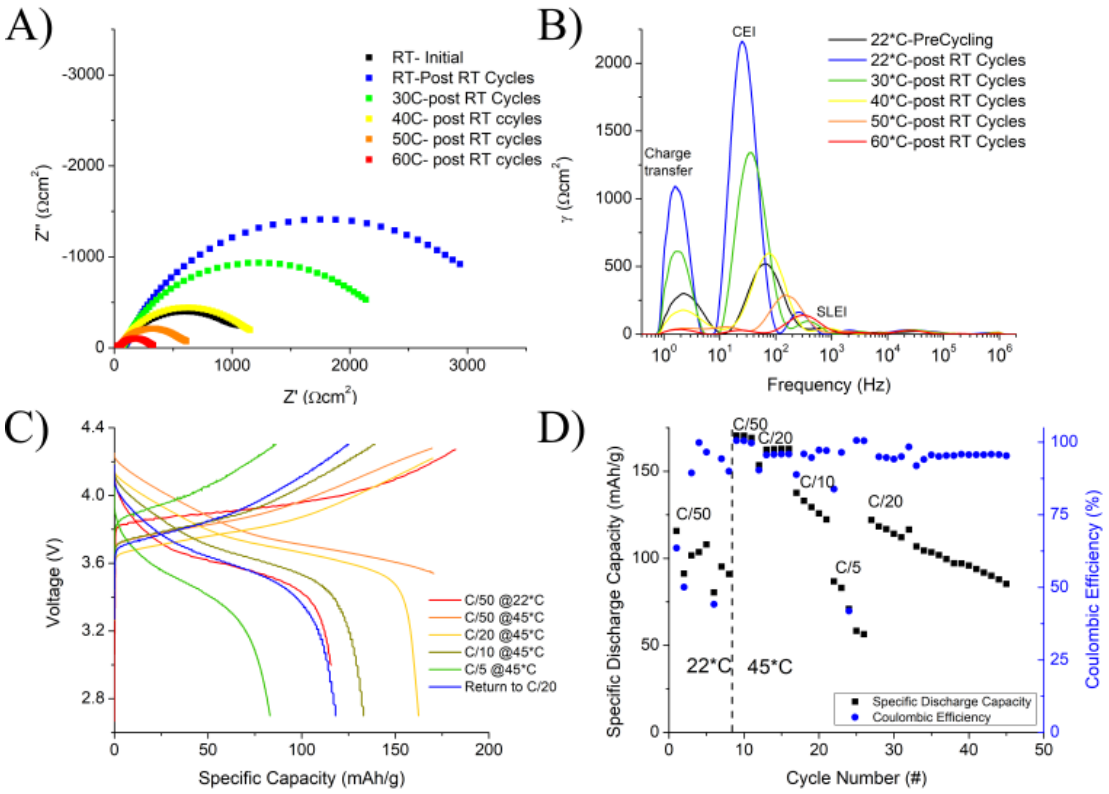

Figure 25. A) EIS temperature sweep, B) DRT temperature sweep, C) voltage profile, and D) cycle life of lithium-NMC cell using trilayer garnet and 0.5 M LiTFSI-Pyr_{14}TFSI-OFPTFE catholyte

.

In addition to improving with temperature, widening voltage range to 4.4-2.7 V from 4.3-3 V was also shown to improve both capacity and previously noted coulombic efficiency issue at room temperature. Low rate cycling using OFPTFE diluted catholyte at C/50 using the voltage range of 4.3 to 3 V, as recommended by the cathode sheet manufacturer, achieved only a little over 100 mAh/g discharge capacity in Figure 26. Widening cycling window to 4.4 to 2.7 V resulted in a slow but consistent capacity increase to 157 mAh/g where the voltage began to plateau. Moreover, in comparing cycles 4 and 12 in Figure 26 the overpotential required for cycling appears to increase

as initial cycling had nearly no discharge capacity above 3.75 V while cycle 12 had around 60 mAh/g by the same voltage. Increasing rate to C/20 (~0.1m A/cm^2) resulted not only in an initial drop to 120 mAh/g discharge capacity but also rapid capacity loss.

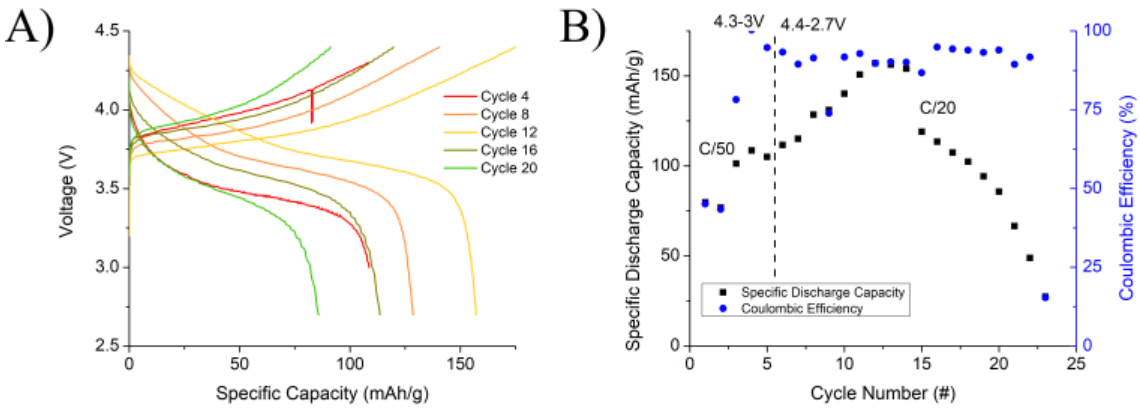

Figure 26. Room Temperature A) voltage profile and B) cycle life of OFPTFE diluted catholyte cell for lithium metal-garnet trilayer-NMC622 cell.

Table 4. Information on fluoro-ether dilutants used in this study.

Name	Abreviation	Boiling Point (°C)
Bis(2,2,2-trifluoroethyl) ether	BTFE	62-63
1,1,2,2-Tetrafluoroethyl 2,2,2-trifluoroethyl ether	TTFTFE	56
1H,1H,5H-octafluoropetyl 1,1,2,2-tetrafluoroethyl ether	OFPTFE	133

Initial cycling for trilayer garnet using 1.5 M LiTFSI-Pyr14TFSI with TTFTFE dilutant displayed low discharge capacity of only 30 mAh/g with high overpotential, as seen in Figure 27A and B. Lowering rate to C/50 improved capacity, but only to 85 mAh/g while the overpotential remained significant. Widening the cycling window did not result in the same large capacity increase seen for OFPTFE cell, resulting in a small, temporary increase instead of a significant and prolonged capacity increase. From EIS

and DRT performed before cycling and between rate changes in Figure 27C and D, we can see massive resistance growth in the mid to high frequency range. Initial resistance shows high resistances related to interfacing cathode with catholyte along with a not insignificant contribution from the catholyte's interface with garnet. However, the cathode-catholyte interfacial resistances grow much more significantly, as its post room temperature cycling DRT shows.

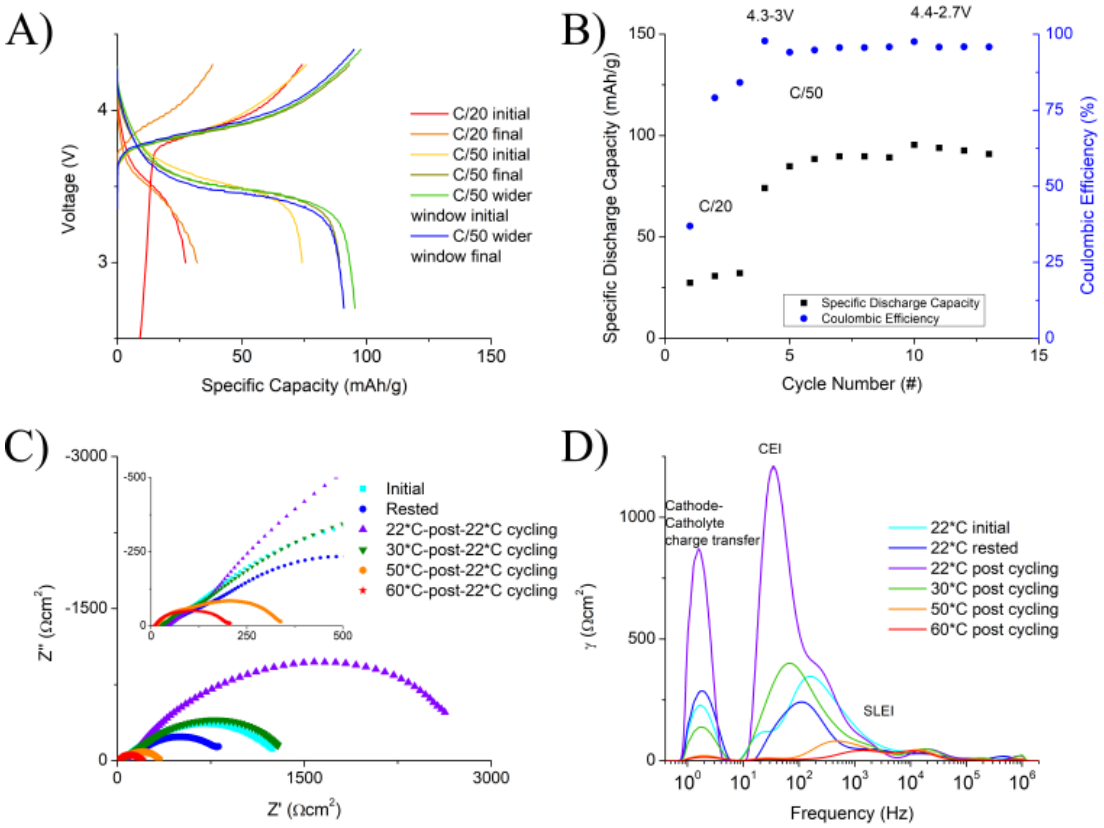

Figure 27. A) voltage profile, B) cycle life, C) EIS temperature sweep, and D) DRT temperature sweep for trilayer garnet, lithium-NMC622 cell with TTFTFE diluted catholyte.

Room temperature cycling of lithium metal-NMC cells using garnet and 1 M LiTFSI $Pyr_{14}TFSI$ with TTFTFE displayed initially high capacity (170 mAh/g) at C/50

(37 μA/cm^2) in Figure 28. After a slight initial drop cycling under these conditions leveled off around 160 mAh/g. Upon increased rate, a rapid decay in capacity was observed, dropping from an initial capacity greater than 130 mAh/g to just over 60 mAh/g after six cycles. Returning the discharge rate to C/50 while continuing a charge rate of C/20 resulted in a brief return to discharge capacity ~140 mAh/g but decayed nearly identically to what was observed with symmetric C/20 cycling. Increased cycling temperature to 45°C similarly returned capacity at C/50 to ~130 mAh/g, but this proved too close to the fluoro-ether's boiling point of 56°C and the capacity again decayed quickly. The lack of capacity recoverability along with the continued increase in potential drop between charge and discharge observed in Figure 28 indicate a lack of growing interfacial resistances possibly from TTFTFE breakdown.

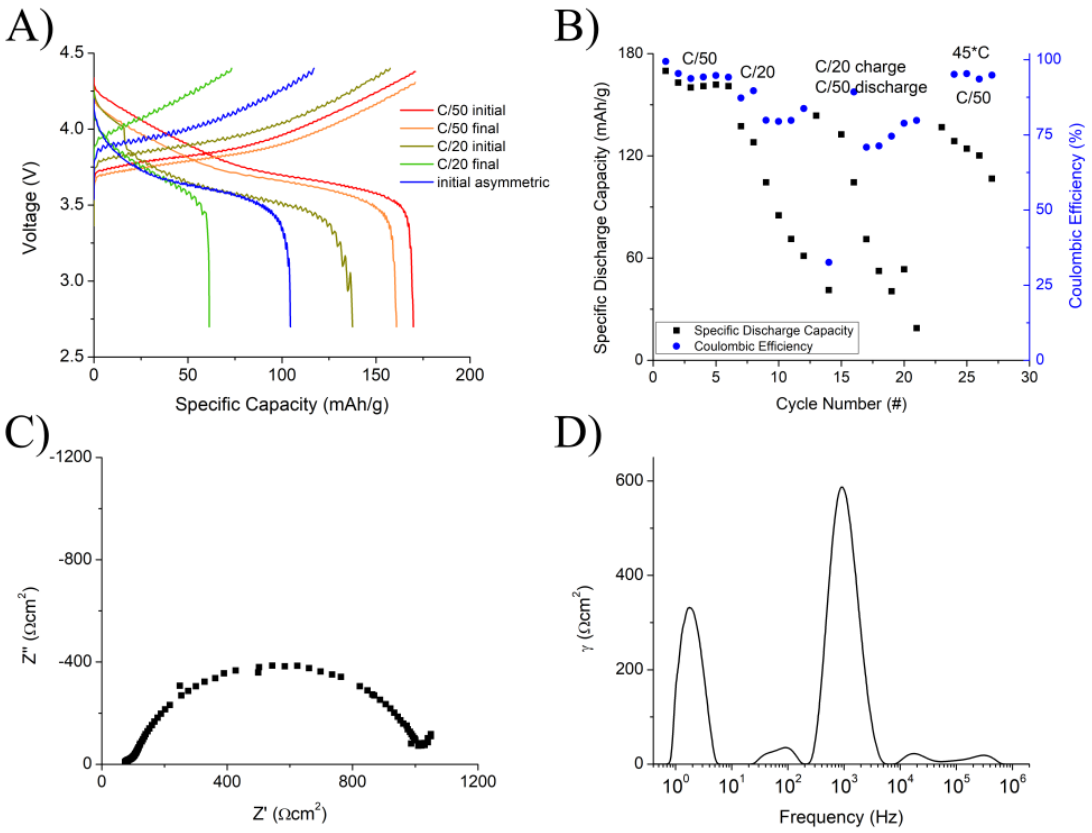

Figure 28. A) Voltage profile, B) discharge-coulombic efficiency for the cycle life, C) EIS, and D) DRT of lithium-NMC cell with bilayer garnet using 1 M LiTFSI $Pyr_{14}TFSI$ with TTFTFE dilutant catholyte

4.4 Conclusions

A series of co-solvents and additives were added to $Pyr_{14}TFSI$ based catholyte with garnet solid electrolyte to study effects on the resultant interface. Increases in LiTFSI concentration in both the base ionic liquid and solvent mixtures led to decreases in the interfacial resistance while blue-shifting the frequency observed via DRT for most interfaces. Cross-referencing this with Raman data, the decreased impedance was correlated with reduction in the signal of free $TFSI^-$ anions. Introduction of TEP and ACN resulted in increased interfacial resistance between garnet and ionic liquid based

catholyte, as determined by EIS and DRT. An LFP cell (13 mg/cm^2 active loading) utilizing TEP co-solvent was achieved 158 and 160 mAh/g at 60°C and 90°C, while retaining over 100 mAh/g at 1.13 mA/cm^2. After cycling up to 2.26 mAh/cm^2 and thermal cycling at room temperature through 90°C again, cell capacity was still recoverable over 120 mAh/g. Fluoro-ethers were then tested to decrease viscosity while minimizing impact on binding structures. TTFTFE and OFPTFE diluted catholytes allowed for high capacity, 170 and 157 mAh/g respectively, at room temperature but only around 37 μA/cm^2 and with expanded cycling voltage window. OFPTFE diluted cell allowed for good capacity and increased rate capability at 45°C, displaying stable capacity around 160 mAh/g at 0.1 mA/cm^2 and not displaying shorting behavior even at 0.4 mA/cm^2. While the TTFTFE-diluted cell initially reached good capacity at this temperature it had a significant capacity loss per cycle. Further optimization of salt to ionic liquid to fluoroether ratio as well as testing catholyte viscosity and alternative ionic liquid chemistry should further improve cell performance.

Chapter 5: Porous Garnet Separators

5.1 Phase, Microstructural Evolution

5.1.1 Phase Evolution and Sintering Environment

Upon indexing and Rietveld refinement of the XRD spectra, displayed in Figure 29A and expounded upon numerically in

Table *5*, display no garnet character at 650°C in either O_2 or air. Increasing sintering temperature to 750°C, a mixture of cubic and tetragonal garnet was observed as the only readily identifiable phases not attributable to the affixing putty under both environments. The sample sintered under atmospheric air with no forced gas flow achieved higher cubic character than its oxygen flow sintered counterpart. Further increasing sintering to 850°C resulted in pure cubic garnet under in oxygen with the air sintered sample containing some lanthanum rich phases, likely indicating a loss of lithium from the structure as no additional lithium containing phases were observed.

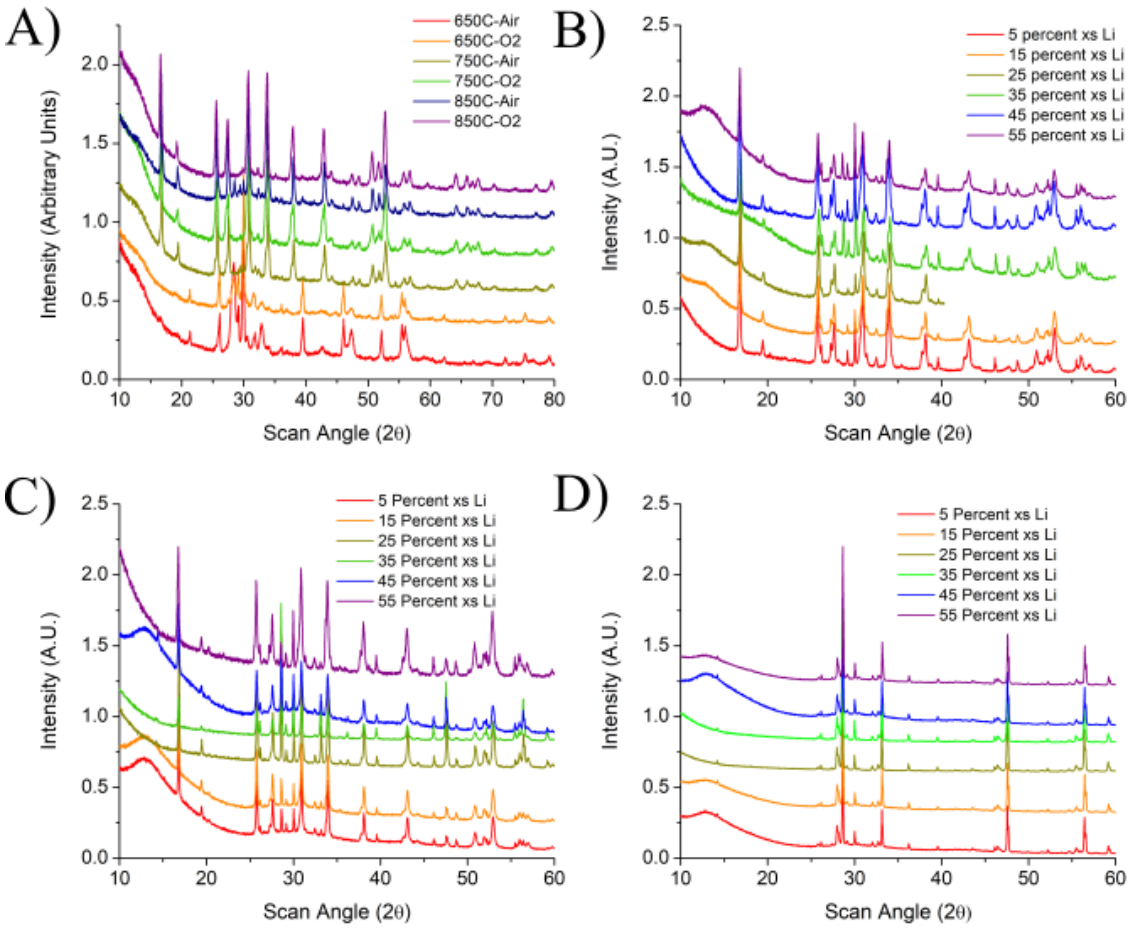

Figure 29XRD A) displaying evolution for reactive phase sintering of tape-cast garnet, and that observing effect of lithium excess at B) 900, C) 1000, and D) 1100 degrees Celsius without powderbed.

Table 5. Final phase composition of thin porous LLZT sintered at various temperatures.

		Phase Fraction				
		Cubic Garnet	Tetragonal Garnet	La_2O_3	$La_2Zr_2O_7$	Li_2CO_3
650°C	Air	0	0	0.415257	0.02037	0.563563
	O_2	0	0	0.395546	0.009274	0.59518
750°C	Air	0.737411	0.262589	0	0	0
	O_2	0.485151	0.514849	0	0	0
850°C	Air	0.47964	0	0.491038	0.029323	0
	O_2	1	0	0	0	0
1150°C	Argon	1	0	0	0	0

Above these temperatures, effect of excess lithium content in tapes was tested, from 5 to 55% in air from 900°C to 1100°C as displayed in Figure 29B-D. At these long sintering times, some lanthanum oxide remained constantly present, shown in the Rietveld Refinement summarized in Table 6, though greatly varied with temperature and lithium excess. A few of these samples, namely those at 5-25 percent lithium excess at 900 and 1000°C, displaying only around 5 weight percent lanthanum oxide. Increased lithium excess displayed an initial uptick in garnet character at 900°C from 91 to 97 weight percent at 5 and 25 percent excess lithium, followed by a massive drop at 35 percent excess to 75 weight percent garnet and a recovery into the 80's above this point. 1000°C sintering displayed similar inverse v-shaped behavior in garnet character relative to excess lithium, though consistently lower garnet content than 900°C. This downtrend in garnet character was further continued into 1100°C sintering as no garnet content was observed regardless of lithium content. In place of high content garnet lanthanum zirconate became the dominant phase observed, with some additional lanthanum oxide. Similarly to lanthanum oxide, lanthanum zirconate was observed in most samples tested, though content was low to none at 900°C.

Table 6. Final weight fraction for phases found in porous LLZN separators of varied lithium excess at different temperatures.

		Weight Fraction					
	Lithium Excess (%)	Cubic Garnet	Tetragonal Garnet	La_2O_3	$La_2Zr_2O_7$	Li_2ZrO_3	$LiNb_3O_8$
900°C	5	0.469(8)	0.446(9)	0.068(3)	0	0.018(5)	0
	15	0.508(8)	0.44(1)	0.0499(3)	0	0	0

	25	0.484(9)	0.48(1)	0.0313(4)	0	0	0
	35	0.358(7)	0.393(9)	0.133(4)	0.076(4)	0.040(7)	0
	45	0.427(8)	0.438(9)	0.103(4)	0.009(2)	0.023(6)	0
	55	0.407(7)	0.396(9)	0.121(4)	0.050(3)	0.027(7)	0
1000° C	5	0.552(7)	0.325(9)	0.049(3)	0.047(3)	0.027(6)	0.195(5)
	15	0.501(7)	0.370(8)	0.048(3)	0.056(3)	0.025(6)	0.203(5)
	25	0.443(8)	0.324(8)	0.051(3)	0.181(4)	0.001(4)	0.187(4)
	35	0.394(8)	0	0.149(4)	0.450(6)	0.008(6)	0.178(5)
	45	0.268(7)	0.449(9)	0.090(3)	0.163(3)	0.031(6)	0.181(5)
	55	0.524(9)	0.34(1)	0.079(4)	0.027(3)	0.035(6)	0.187(5)
1100° C	5	0	0	0.085(3)	0.720(6)	0	0
	15	0	0	0.075(3)	0.722(6)	0	0
	25	0	0	0.077(3)	0.736(7)	0	0
	35	0	0	0.098(3)	0.724(7)	0	0
	45	0	0	0.088(4)	0.730(6)	0	0
	55	0	0	0.092(3)	0.721(6)	0	0

5.1.2 TGA-DSC

Organics observed to burnout with its major peak around 300°C in Figure 30 for the pre-milled powder, while using sourced nano-powders led to two distinct peaks around 325 and 400°C, likely related to various lanthanum phases on the nano-powder as discussed by other groups[143]. Initial weight loss observed from organics and lanthanum impurities levels out by 500°C for both sets of samples. While less obvious in the TGA curve, DSC displays disconnected carbonate decomposition/melting peaks at 725°C and 775°C in Figure 30 for all samples. These are attributed to lithium

carbonate as the lower temperature peak and lanthanum carbonate at the higher, helping to explain its larger peak in samples using as-received nano lanthanum. In conjunction with the observed XRD under oxygen flow these carbonate melts/decompositions also appear to highly correlate with formation of tetragonal and cubic garnets. The continued observed mild linear endothermic response above these peaks is likely related to evaporation of lithium species and possible reaction with alumina TGA boats.

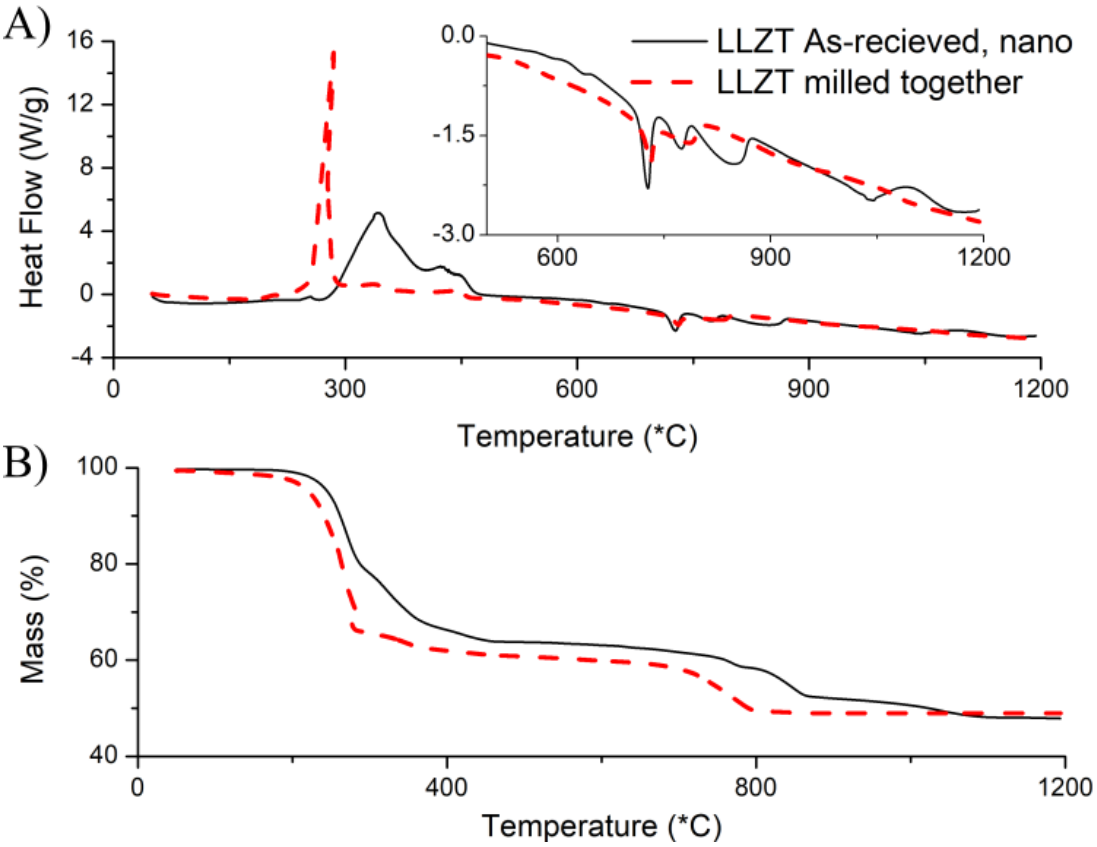

Figure 30. A) DSC and B) TGA of garnet tapes made using as-received nano powders and in-house milled garnet precursors with and without extra lithium carbonate in the TGA boat.

5.1.2 Microstructure

Analyzing Figure 31 using ImageJ, converting to binary and using watershed to segment large particles, showed that despite particle growth from 0.24 um^2 to 2.7

um^2, porosity remained in the 60% range. Comparing the as-received nano-precursors to milled nano-precursor in Figure 31, far larger grains, and subsequently larger interconnections were observed in the as-received nano-powder. Analyzing these particles, as previously discussed, indicated double the particle size for the nano powder relative to the milled particles. This leads to a less flexible sample given the inverse relationship between thickness and flexibility though somewhat increased strength for the same reason.

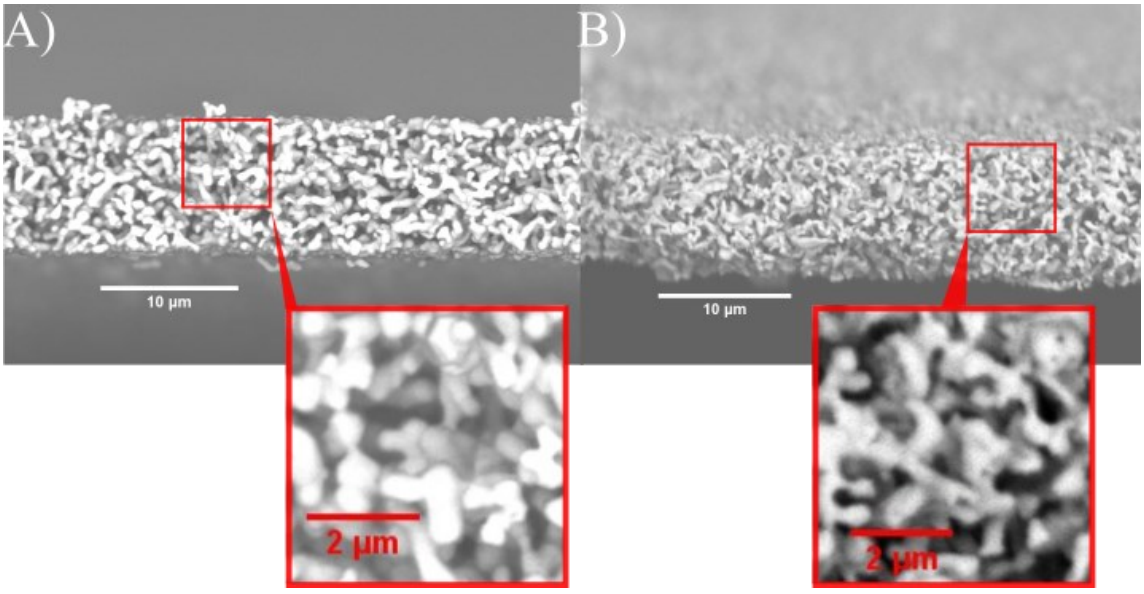

Figure 31. Sintered microstructure from tapes using A) as-received precursor powders and B) nano-precursors.

5.2 Liquid Cell Testing

5.2.1 Determination of MacMullen Number

Cell resistance was obtained by subtracting contact resistance from the observed x-intercept from EIS of the flooded cells. After removal of a few outlier data, MacMullen number was calculated individually for each cell and averaged for

separator type. The increase in areal resistance used for this is shown in Figure 32. Porous LLZO separator displays far lower resistance and much slower resistance increase with thickness than the Celgard 2325, translating into MacMullin numbers of 1.52 and 10.6 respectively. The obtained 10.6 MacMullin value for Celgard falls well within observed literature data, while a value of 1.52 places porous LLZO separator very near the ideal value of one [32], [144], [145], [146], [147]. This nearly order of magnitude lower MacMullin number, accounting for a combination of surface effects, higher porosity, and lower tortuosity, is made evident by the porous LLZO separator of 75 µm contributing only around half of the resistance observed for Celgard a third of the same thickness.

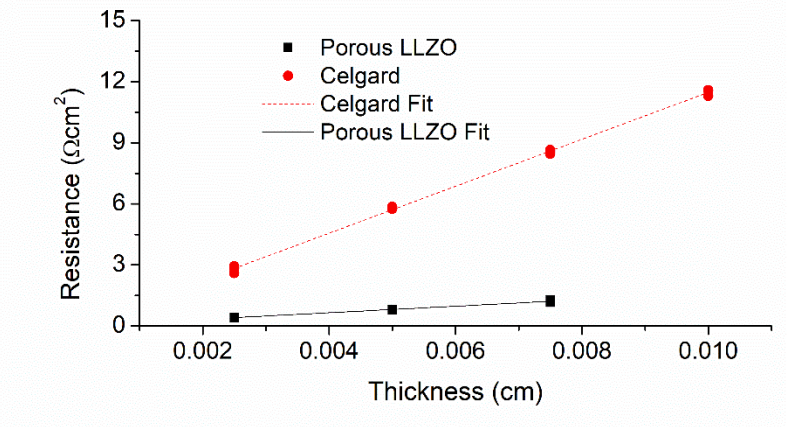

Figure 32 Comparison of areal resistance increase with additional layers of either Celgard2325 or porous LLZO separator.

5.2.2 Graphite-NMC Cell Testing

Figure 33A shows the voltage profile for the NMC622 graphite cell tested with uncoated porous LLZO separator. Formation cycling cycles at C/20 display low overpotential, with voltage not significantly changing between cycling, with gradual

increase in this resulting in minimal charge/discharge plateaus for 3C and 4C cycling. This is reflected in Figure 33B where capacity is gradually lost through C, peaking at 99 mAh/g and dropping to 69 mAh/g at C. Further pushing to rate to 4C, only around 20 mAh/g discharge capacity was retained. Returning cell rate to C/20, capacity returned to 80 mAh/g on cycle 30.

Similar to the formation cycles with the uncoated sample, the LiPAA-coated porous garnet separator in Figure 33C and D displayed an early cycle with lesser capacity before increasing and stabilizing at 140 mAh/g. Initial rate testing similarly pushed to 4C, maintaining discharge capacities of 115 and 65 at rates of C and 4C respectively. After relaxing rate to C/20 and re-increasing to 1 C, capacity returned to 125 and 85 mAh/g. Over the 200 cycles the cell maintained C-rate of 1 C, minimal capacity decay was observed with the cell maintaining nearly 90% of its capacity. Final rate testing from here increased to 6C, displaying no shorting behavior, though capacity was greatly reduced. Relaxing cycle-rate C/20, capacity returned to 90 mAh/g.

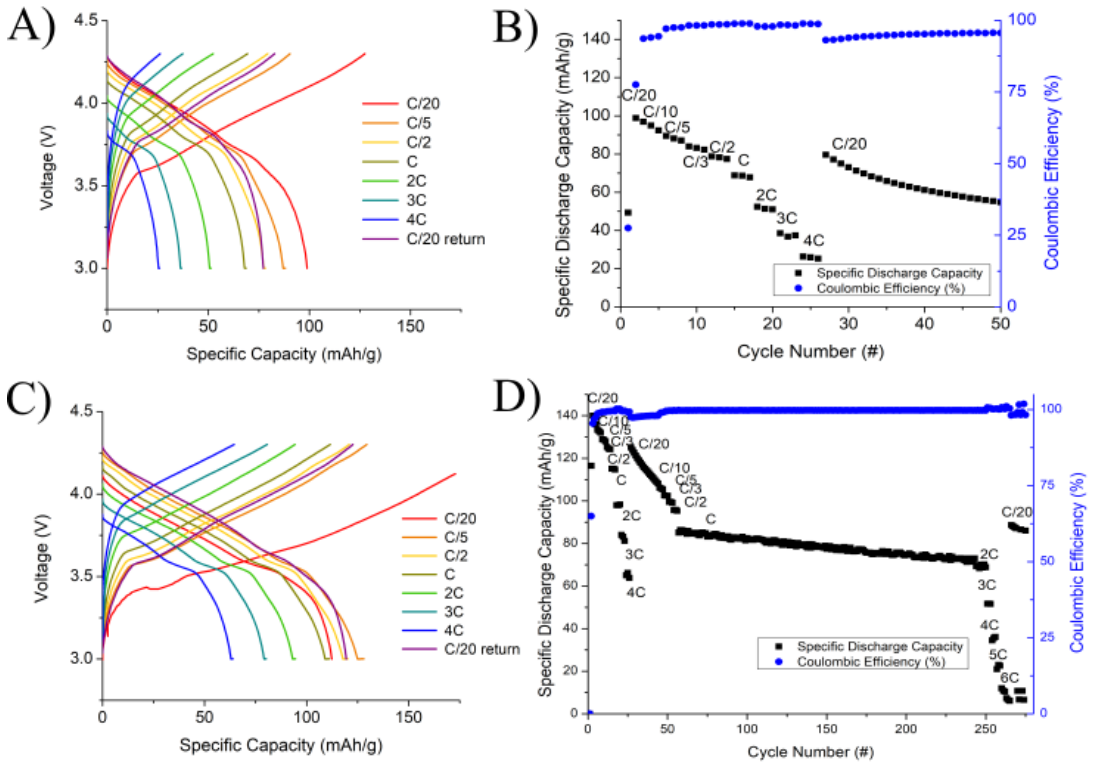

Figure 33. Voltage profiles and discharge-cycle life for uncoated A) and B) and LiPAA coated C) and D) porous LLZO separator with graphite and NMC622 electrodes using 1M $LiPF_6$ EC/DEC standard electrolyte.

5.2.3 Post-Mortem

Post-mortem SEM in Figure 34 of the coated separator shows the porous garnet structure distinctly with what appears to be largely a single organic phase throughout, indicating good stability of the LiPAA inside of the region. Surface of the graphite anode similarly displays minimal issues, with a few grains of garnet removed from the separator remaining behind and a small amount of organic buildup. The surface of the NMC cathode however appears to display a higher buildup of organics as typical meatball structure cannot be observed. This buildup of organic on the cathode surface appears to be the culprit for the observed capacity decay.

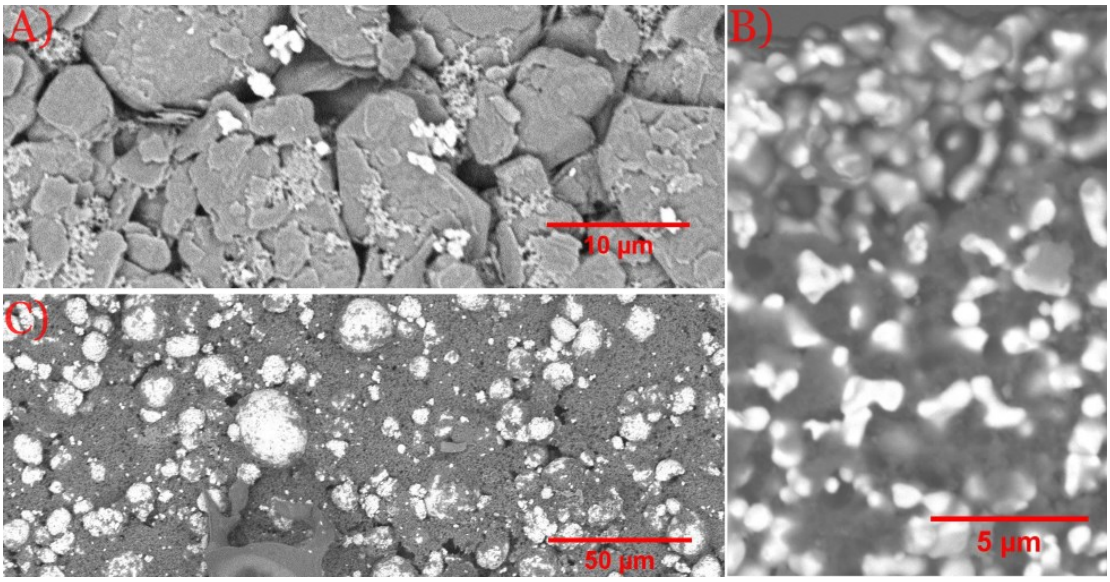

Figure 34. Post-Mortem SEM of A) graphite anode, B) LiPAA coated porous LLZO separator, and C) NMC cathode.

5.3 Extending Methods to Electrode Materials

Sintered LTO, utilizing a small excess of lithium carbonate, was shown to form pure phase LTO indicating a slight excess of lithium relative to the base $Li_4Ti_5O_{12}$ shown from the indexed XRD in Figure 35A. The sintered structures could easily be wetted with lithium as demonstrated in Figure 35B and C displaying LTO before and after melt-infiltration of lithium metal. These structures were shown to be capable of directly plating lithium in electrochemical cells without previous infiltration against lithium metal in Figure 35D. Post mortem confirms that lithium was plating directly into the pores in the asymmetric lithium-lithium host liquid cell as the darker phase is seen preferentially in the host towards the separator instead of the current collector

below in Figure 35E. This plating nature also confirms good electronic conductivity through the host can be observed to be over 100µm in the post-mortem SEM.

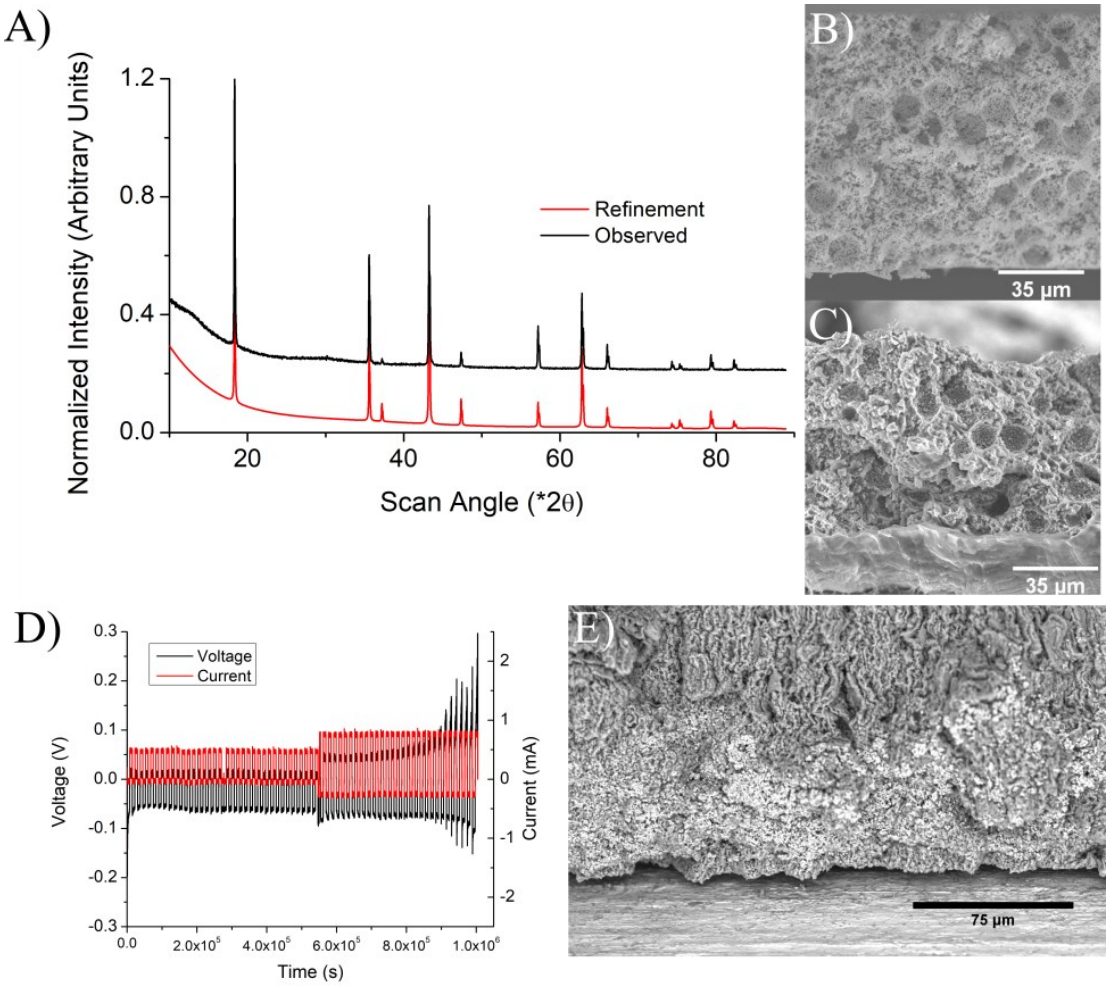

Figure 35. A) XRD spectra of sintered LTO, SEM of B) as-sintered and C) lithium infiltrated LTO, D) Cycling of uninfiltrated host against Li metal, and E) post-mortem SEM showing lithium electrochemically plated into the top of LTO host.

Figure 36 shows that in co-sintering the LCO structure with the garnet separator shows that some impurities exist. Indexing of the impurity peaks reveal the presence of lanthanum oxide, zirconium oxide, and lanthanum zirconate in addition to the desired LCO and garnet phases. Importantly the only observed bulk impurities indicate a loss

of lithium in the garnet phase as the LCO remain pure. SEM and backscatter analysis further display the lack of interdiffusion of non-lithium species between layers. Cycling of this material further show the purity of cathode material given the high discharge capacity despite the sample thickness. Interestingly, the capacity observed in this sample was largely obtained in a fairly narrow voltage window. Thus the rapid decay in capacity is likely related to the large amount of interfacial layer developed outside of this window where most LCO-graphite cells achieve a significant amount of capacity.

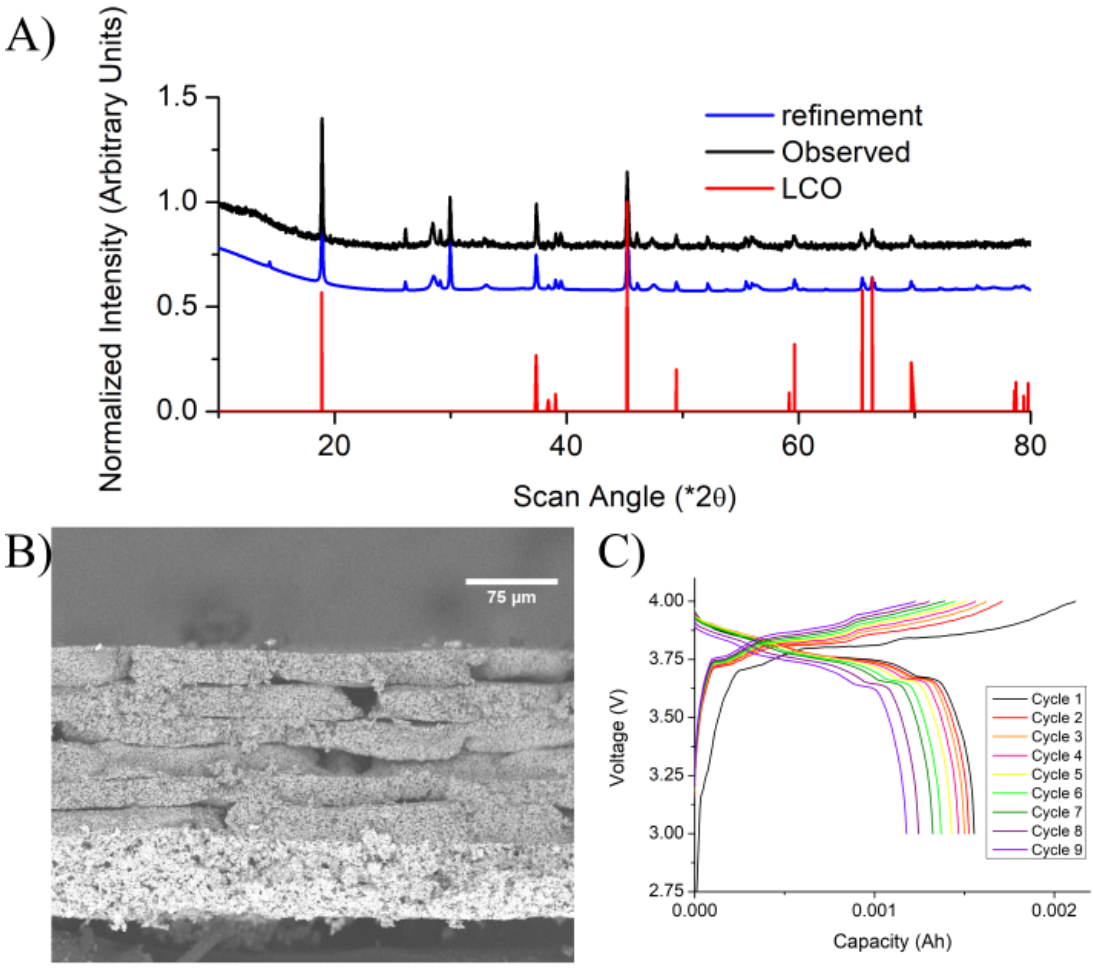

Figure 36. A) XRD, B) back-scatter SEM, and C) cycling of LCO- porous LLZO separator co-sintered structure against graphite with standard electrolyte.

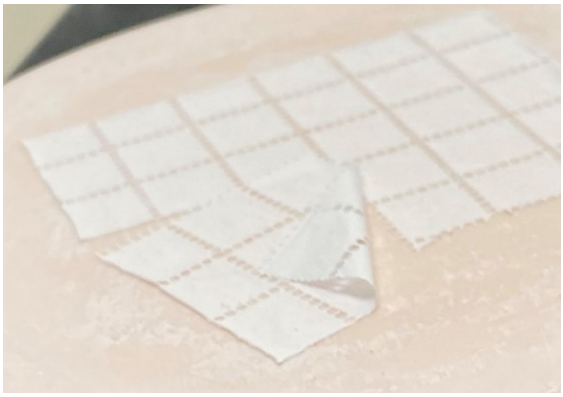

Figure 37.Post sintered separator structure displaying flexibility.

5.5 Conclusions

Porous garnet structures were synthesized, along with cathode and anode host structures, directly from low-reactivity precursors. Phase evolution were examined through XRD and TGA/DSC. Thinner structures and smaller particles resulted in more flexible structures which were balanced with the added mechanical robustness of large grain-to-grain connections provided for cell fabrication. High rates were observed in full NMC-Li cells using the porous structure without shorting, with improved capacity achieved using a polymeric coating. Coated and uncoated samples were pushed to C-rates or 4C (8 mA/cm^2) and 6C (12 mA/cm^2), respectively, with no indications of shorting behavior observed. Cathode and lithium host anode structures were both successfully synthesized and tested using similar methods.

Chapter 6: Free-standing Near-Thin-Film Garnet Electrolytes

6.1 Sintering Environment, Phase Evolution, and Microstructure

6.1.1 DSC-TGA

Using 550°C pre-sintered samples to isolate ceramics behaviors from the organics used in tape casting, higher temperature sintering behavior was further tested in Figure 38 using a series of carbon based powderbeds under argon to minimize reaction of samples with alumina TGA boats. DSC curves in Figure 38A all three samples display a single carbonate melt just under 750°C with graphite bed's peak being the sharpest and at the lowest temperature, activated carbon the broadest and highest temperature, and graphite with added lithium carbonate in between. After this an extended shoulder is apparent whose end shifts from around 835°C for activated carbon to 850°C and all the way to 885°C for graphite/lithium carbonate: increasing from activated carbon, graphite, to graphite with lithium carbonate in an inverse relationship with how reductive the environment is. A final highly endothermic reaction beyond this shoulder is observed for all three samples, with the activated carbon sample resulting peaking around 1050°C, only slightly eclipsing the intensity of its carbonate peak. Both graphite, at 1130°C, and graphite-lithium carbonate, at both 1070°C and 1130°C, samples had similar intensity peaks. These peaks were more difficult to detect in graphite containing samples due to an additional, high intensity peak around 1170°C, which was significantly more intense for the sample without additional lithium carbonate. Peaks around 1050-1130°C are likely sintering related, while the peak nearer 1200°C that was suppressed by additional lithium carbonate may

be high-temperature side-reaction between garnet and graphite delithiating the garnet, not experience by the activated carbon due to its lack of crystallization.

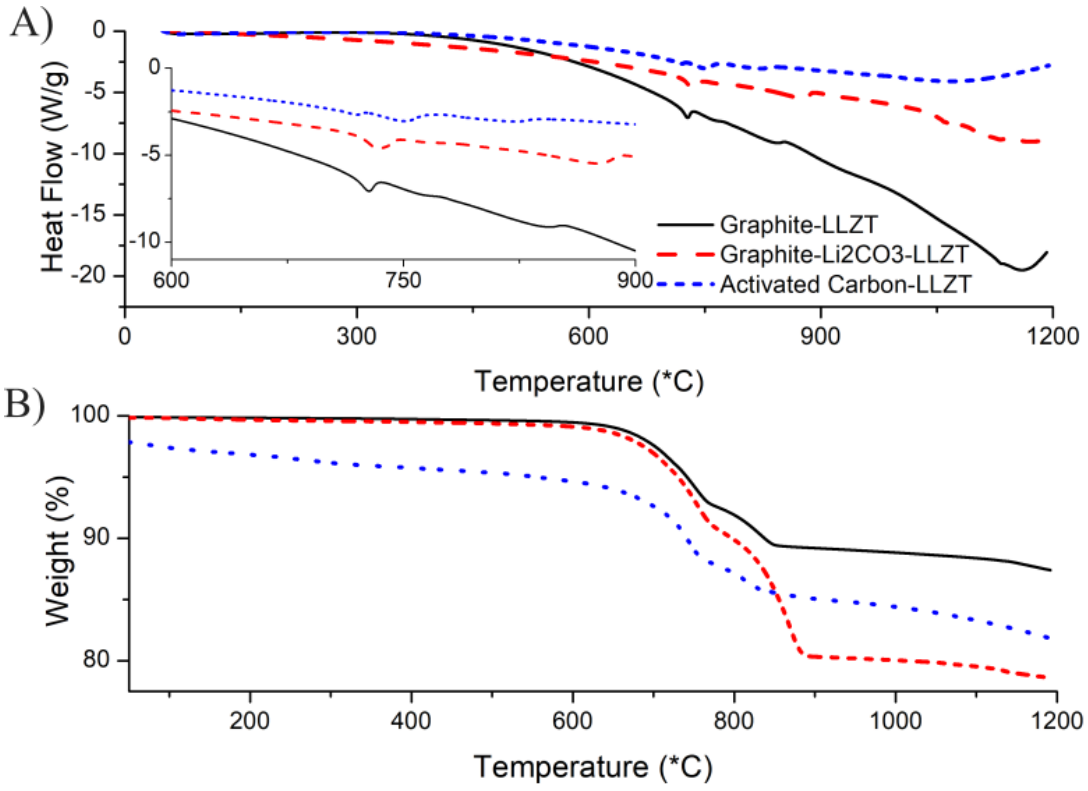

Figure 38. A) DSC and B) TGA of garnet tapes pre-sintered at 550°C with varied carbon sources as powderbed to isolate from the TGA boat.

6.1.2 Microstructure

Green-bodies sintered with external lithium carbonate on magnesium oxide showed significant densification as well intragranular fracture surface. Samples sintered around 1050°C still retained too high porosity for use as stand-alone dense layer as displayed by Figure 39. However once taken above the peak observed from DSC, retained only minimal porosity that is likely related to the other issue observed in this environment: non-uniform sintering, samples sintering onto MgO powderbed, and tearing of samples during sintering. Though MgO plates are often used in sintering

garnet when avoiding alumina-doping of the structure, MgO itself can begin sintering in atmospheres similar to those used here for garnet[59]. By switching to argon atmosphere with graphite-lithium carbonate powderbeds, highly thin stand-alone dense structures were achieved. Under this environment at 1125°C 10 and 6 µm thick dense garnets were produced, as seen in Figure 39C and D. The thicker of these samples retained high intergranular bonding seen through the intragranular fracture pattern observed in cross-sectional SEM. The thinner of these samples however had mixed inter- and intra- granular fracture. Surface SEM of this sample displayed consistent high density, without large pinholes.

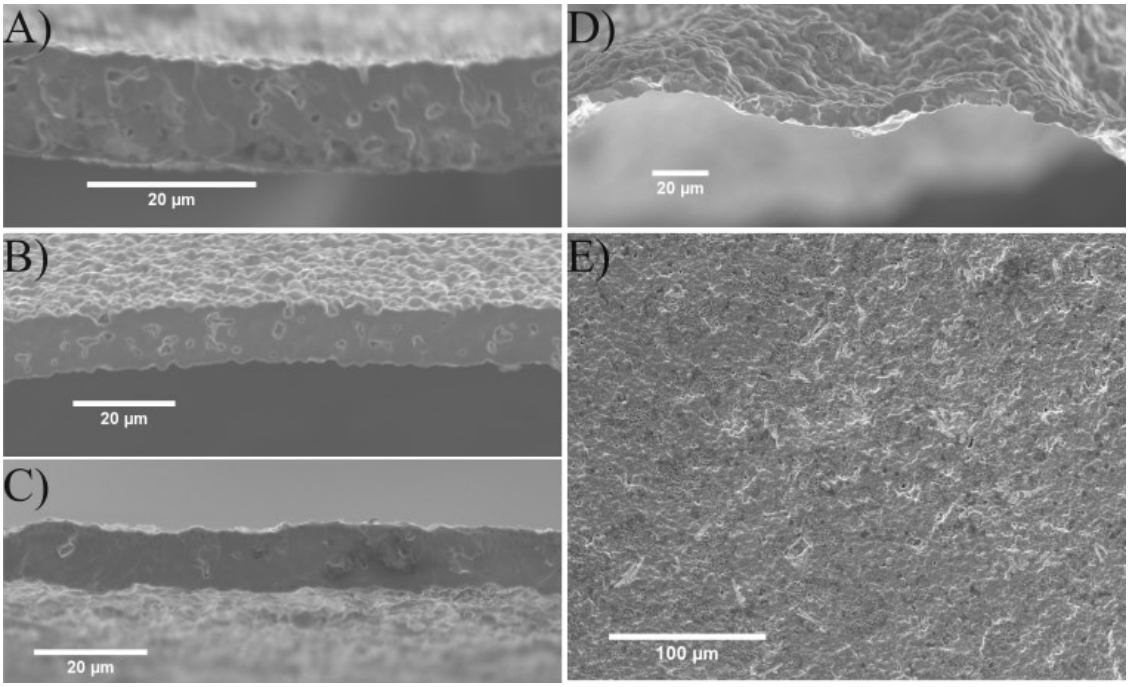

Figure 39. Sintered cross-sectional microstructure for tapes sintered in air at A)1050℃ and B)1100℃ and Argon at 1125℃ C) with thicker tape, D) thin tape, and E) top-down images of thin tape.

Using slightly thicker sample and increasing sintering temperature allowed for the 20µm stand-alone dense layer, of a more intragranular fracture nature. Shortening the sintering time, as in Figure 40, by a full hour still resulted in a fully dense structure.

Observing through backscatter mode of the same structure in Figure 40 shows scattered darker grains within the structure, which EDS indicated as containing high tantalum content. Raman spectroscopy of the garnet similarly displayed a high tantalum character, seen through the peak around 750cm^{-1} , on certain scans. Taken together, this indicates that, while well densified, additional time is required to allow for diffusion to make uniform dense garnet.

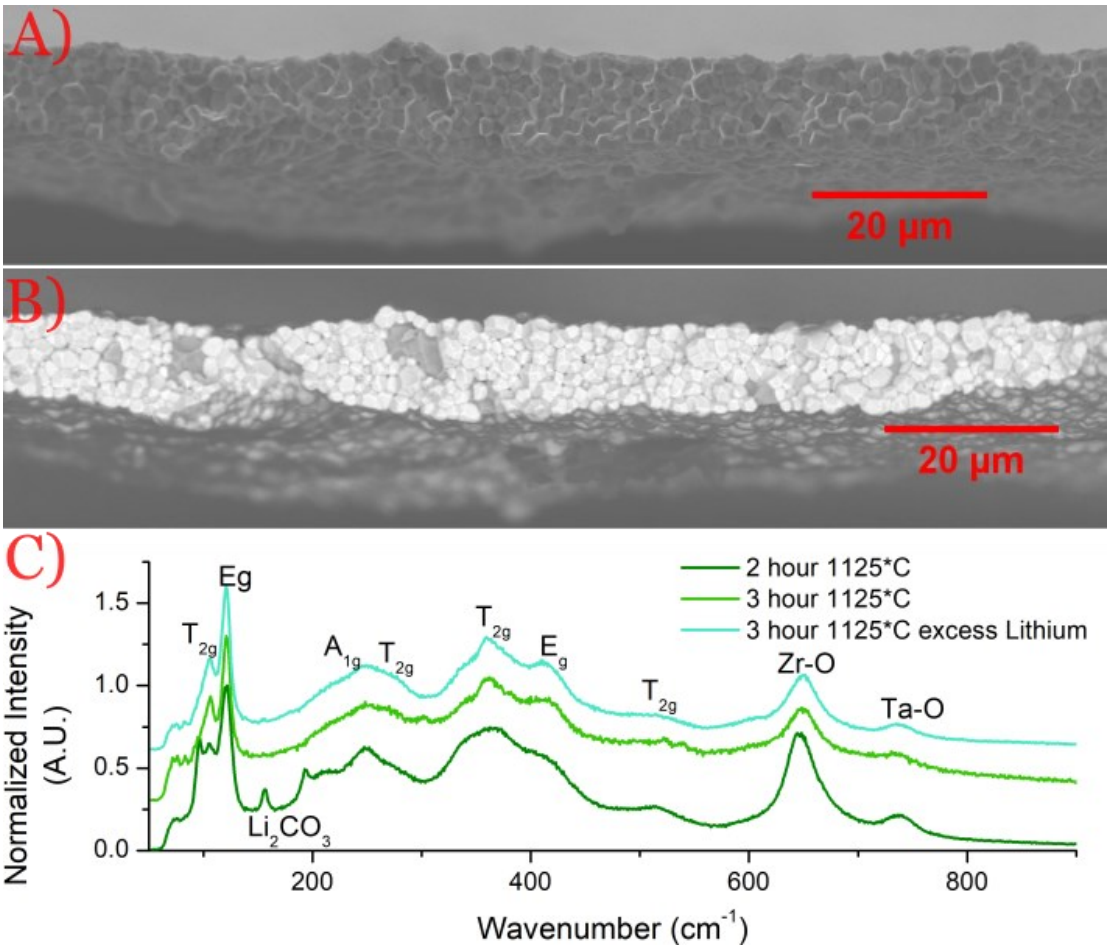

Figure 40. A) SEM and B) backscatter for thin LLZT sintered 2 hours and C) Raman Spectroscopy comparing sintering conditions.

6.1.3 Phase

Indexing of LLZT sintered at 1115°C under Argon using graphite/lithium carbonate powderbed indicated nearly pure cubic phase garnet, with a small amount of

lithium carbonate remaining. While indexing the 1150°C sample, TiO_2 and $CaCO_3$ from the clay affixing the sample to the sample holder and graphite remaining on the surface from the powderbed were observed in addition to cubic phase garnet. Intensity for garnet-related peaks in the 1150°C sample were significantly less intense than those observed for 1115°C.

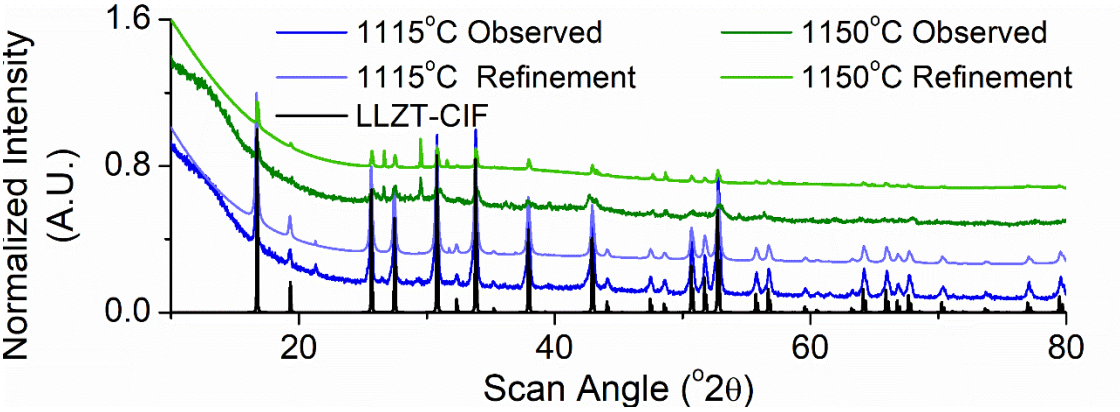

Figure 41. XRD spectra for thin LLZT sintered 1115°C under argon flow.

6.2 Conductivity

DC polarization displayed an increase in electrical conductivity with temperature increased, with the outlier of 25°C in Figure 42A. After normalizing for sample thickness and electrode area, this was determined to correspond to an electrical conductivity of $2*10^{-10}$ S/cm at 25°C and $2.5*10^{-10}$ S/cm at 75°C, placing it below the previously observed values for bulk garnet, but around those for single crystal and above the theoretical [148], [149], [150], [151], [152], [153]. Noise in the measurement was noted to occur when either the environmental chamber blower began turned on or other channels performed EIS and are thus not attributed to issues with the samples.

EIS, performed on the cooling cycle after heating for polarization, displayed an apparent increased x-intercept value, here taken as garnet conductivity, until 0℃ where an increasing presence of electrode-garnet interfacial component complicates the impedance. At 15℃ the x-intercept of 11 Ωcm^2 corresponded to $9*10^{-5}$S/cm, a little below the 10^{-4} S/cm common to most LLZT samples. This can be attributed to the low tantalum dopant concentration, and argon sintering environment. Taking these factors into account, the observed lithium conductivity is within the range observed in literature[154], [155]. Future dopant optimization and possible co-doping should be able to push this conductivity higher[156], [157], [158], [159].

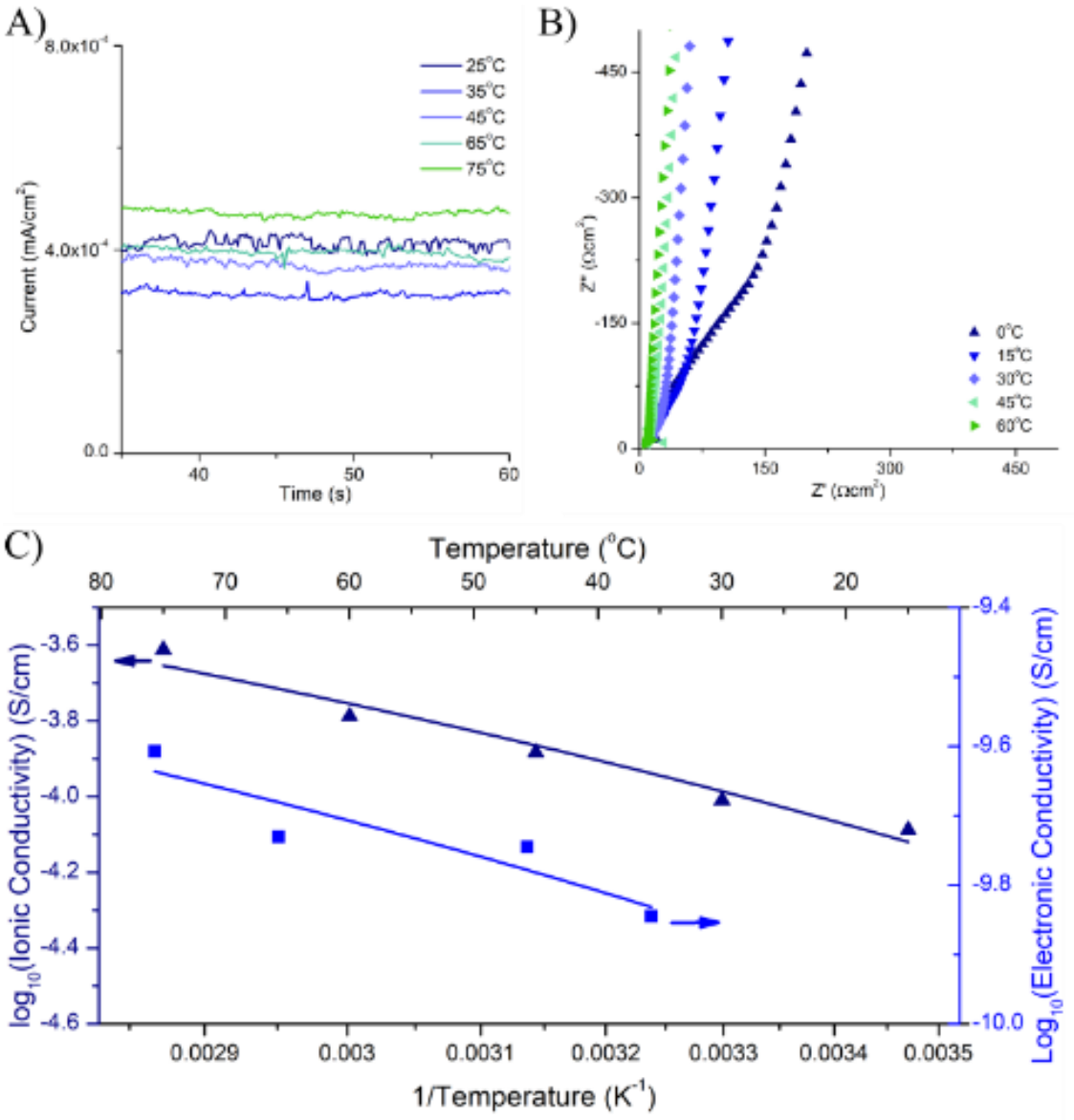

Figure 42. A) DC-Polarization, B) EIS with part of the Warburg tail removed, and C) Arrhenius plot of the calculated ionic and electronic conductivities from 8 um LLZT using gold electrodes over a range of temperatures.

6.3 Cell Testing

6.3.1 Lithium Symmetric

Cycling lithium symmetric cells with dense garnet electrolytes similar to those shown in Figure 39D is displayed in Figure 43, with initial capacity scaling with current

until reaching 10 mAh/cm^2. Current-voltage response remained proportional through the first current ramp through 20 mA/cm^2, as seen in Figure 43, with no indication of shorting. The cell was then allowed to plate and strip lithium for another 1900 hours at 8 mA/cm^2 and 8 mAh/cm^2 for another 1900 hours, in which time an external electrical event caused a sudden spike around hour 1400. During this time there was fluctuation in the voltage tentatively attributed to active area lost and regained, as will be addressed in discussion on EIS. After 2300 total hours of cycling a second rate test was performed, shown in the second inset of Figure 43, which would continue until failure. The resulting voltage response to current continued proportionally through 60 mA/cm^2. Increasing to 75 mA/cm^2 some noise becomes apparent in the voltage response, along with a slight increase in apparent resistance relative to previous rates. While initial voltage response to 100 mA/cm^2 appeared proportional to 75 mA/cm^2, the voltage dropped significantly shortly into the cycle, below what would have been proportional to previous cycling, indicating probable short of the cell.

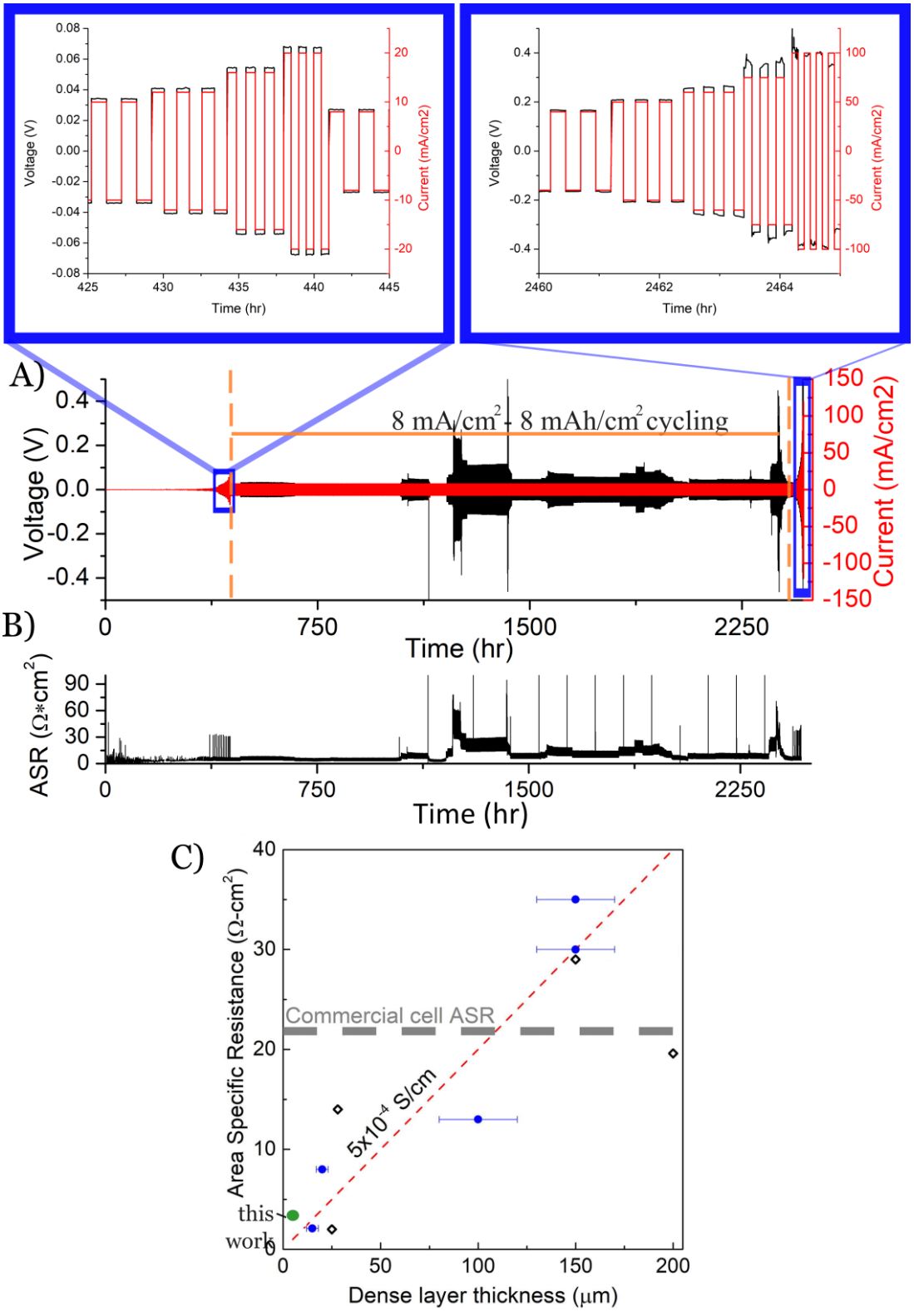

Figure 43. A) Lithium symmetric cycling for thin, 6 μm, dense LLZT, with two insets for the two rate-tests performed. Insets are from around the end of their respective

rate-testing. B) Arial specific resistance (ASR) is calculated directly from cycling data. C) ASR-dense layer thickness comparison adapted from Hitz et al[29], with individual references given in Hitz et al. This work is the green point, with blue points from Hitz et al, black points referenced by Hitz et al, and red dashed line calculated as ASR of commercial 18650 cell in supplementary information by Hitz et al.

During the constant 8 mAh/cm^2 8 mA/cm^2 cycling, EIS was incorporated into the cycling parameters every 100 hours. Nyquist plots from this EIS displayed inductive behavior followed by an x-intercept with a single arc as observed in Figure 44. Inductive tail observed is attributed to a combination of the wires, current collectors, and lithium electrodes, especially given the diffusion lengths in these metal components relative that of the garnet. X-intercept was taken as conductivity of garnet grains, with grain boundary resistance taken as non-contributing given the largely single grain thickness microstructure such as was shown in Figure 39D. Conductivity from these assumptions were consistent with literature values for Tantalum-doped garnet conductivity[151], [153], [160], at 10^{-4} S/cm. Thus, the remaining arc is taken as the interfacial transfer of lithium between garnet and metal. This is further confirmed by the apparent peak frequency of the arc around 40 kHz, which closely mirrors previously published data on ALD alumina coated garnet pellets of 10 kHz [77]. The frequency shift observed could be attributable to improved interface from shorter air exposure time, increasing the surface area without carbonate in the final structure, or from change in composition of the garnet itself.

As the shape of EIS response in Figure 44 remained consistent, only shifting with proportionally increasing or decreasing arcs, the previous attribution of observed resistance change during cycling to loss and rewetting of active area within the cell at

high rates is further supported. EIS performed after the second rate-test however, did not retain this same shape. This Nyquist plots, the left inset in Figure 44, maintained some of the inductive behavior and x-intercept with possible garnet conductivity, but continued trending largely up into negative imaginary impedance and towards the y-axis instead of retaining the characteristic interfacial arc. In conjunction with previously mentioned voltage drop and shaky voltage, this change in EIS was taken as confirmation of shorting of the cell.

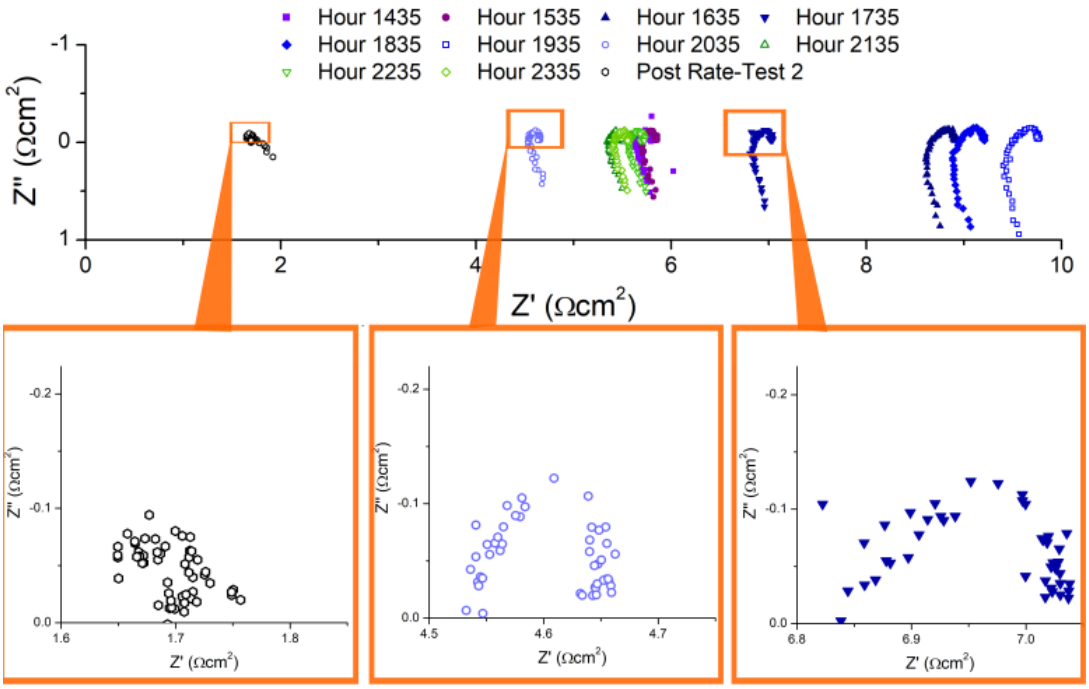

Figure 44. Nyquist plots for EIS of lithium symmetric cell using thin LLZT performed during 8 mA/cm^2-8mAh/cm^2 cycling and after the second rate test.

6.3.2 Lithium-NMC Cycling

Symmetric charge/discharge current density cycling of lithium metal-thin dense garnet-Celgard-NMC using $LiPF_6$ EC/DEC displayed high capacity, reaching 215 mAh/g at 67 µA/cm2 after initial formation cycles. Celgard was incorporated in these

cells to provide mechanical support for the thin ceramic. Capacity remained high, once again 215 mAh/g, and consistent through cycling at 0.14 mA/cm^2, with capacity retention dropping significantly when pushed to 0.244 mA/cm^2. Pushing current further to 0.49 mA/cm^2 and 0.81 mA/cm^2 results in similar capacity decay, along with less stable coulombic efficiency. Returning current back down to 0.14mA/cm^2 did not abate this capacity decay rate nor loss.

Utilizing a CC-CV cycling profile based upon DOE's eXtreme Fast Charge profile, the lithium-thin dense garnet-NMC cell with Celgard and $LiPF_6$ EC/DEC increased charge and discharge current similarly until 0.55 mA/cm^2 cycling, where the constant-current step for discharge would continue to remain at 0.39 mA/cm^2. High capacity of 220 mAh/g was achieved at 0.1mA/cm^2, which dropped to 205 mAh/g at 0.2 mA/cm^2 though this remained highly stable. Increased current beyond this resulted in continued capacity loss, though at a much-reduced rate when compared to the previous cell. Charge-discharge voltage profiles for this cell retain similar shape, except for shifts caused by increased resistance at higher rates in Figure 45C until current exceeded 1 mA/cm^2, where the constant voltage step of the charge cycle took increasingly prominent role. Upon increasing charge current to 2 mA/cm^2, virtually the entire charge cycle was constant voltage, with the set current becoming the starting point from which it would decay. Even under this extreme charge profile, the cell retained discharge capacity of 175 mAh/g, and only dropped to 160 mAh/g when putting this starting current as 4 mA/cm^2. Returning the charge current back to 0.4 mA/cm^2 to make the profile symmetric, the lost capacity did not return, but the

discharge capacity lost between cycles became much less than under high charge currents.

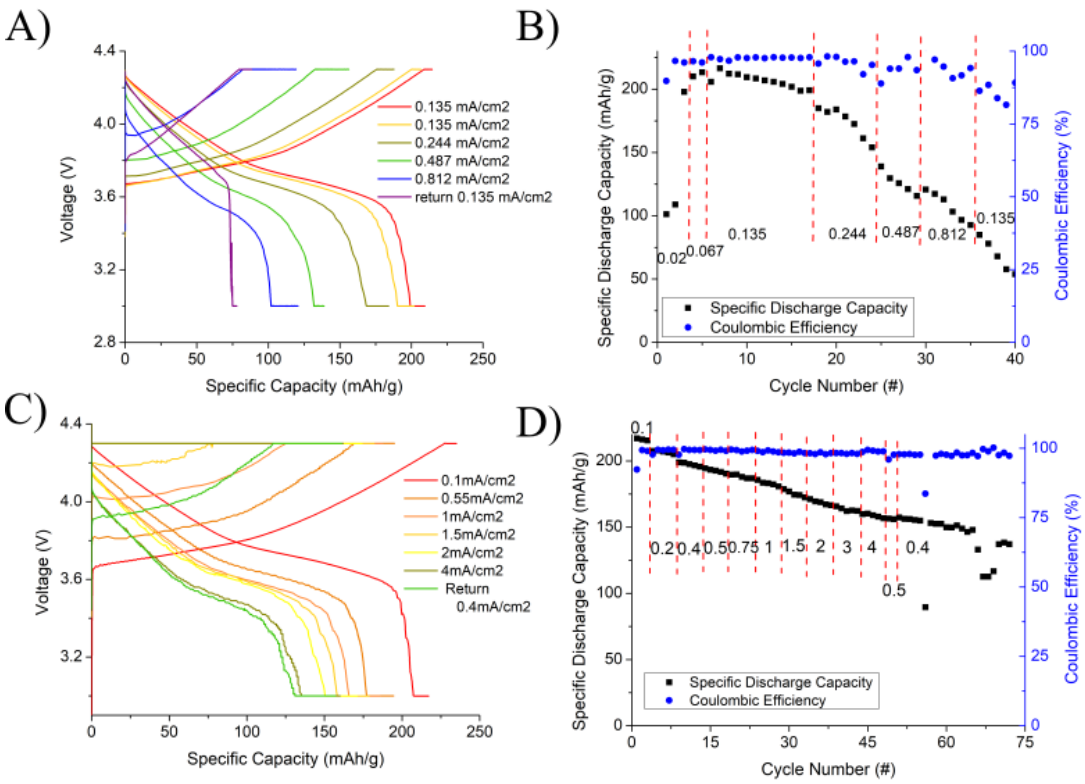

Figure 45. Cell voltage profiles and cycle discharge-coulombic efficiency for lithium metal-thin dense garnet-celgard-1M LiPF6 EC/DEC-NMC622 under symmetric cycling A) and B), with the current reported relating to charge and discharge, and asymetric current C) and D), with reported discharge current capped at 0.39 mA/cm^2 once reached.

Initial EIS of the lithium metal-thin dense LLZT-Celgard/$LiPF_6$ EC/DEC-NMC 622 displayed a low impedance, slightly under 300 Ωcm^2 (Figure 46). After cycling, the total impedance was observed to have more than doubled to just over 600 Ωcm^2. The majority of this growth was observed to have occurred in the middle to high frequency regieme shown as 100 Hz has shifted from near the Warburg tail to the middle point of the impedance arcs. Discussion of EIS and DRT of quasi-solid-state garnet batteries in previous sections indicates this growth in impedance to be largely

related to cathode-catholyte interfaces, with some of the growth in impedance at slightly higher frequency to be solid electrolyte to liquid electrolyte interface.

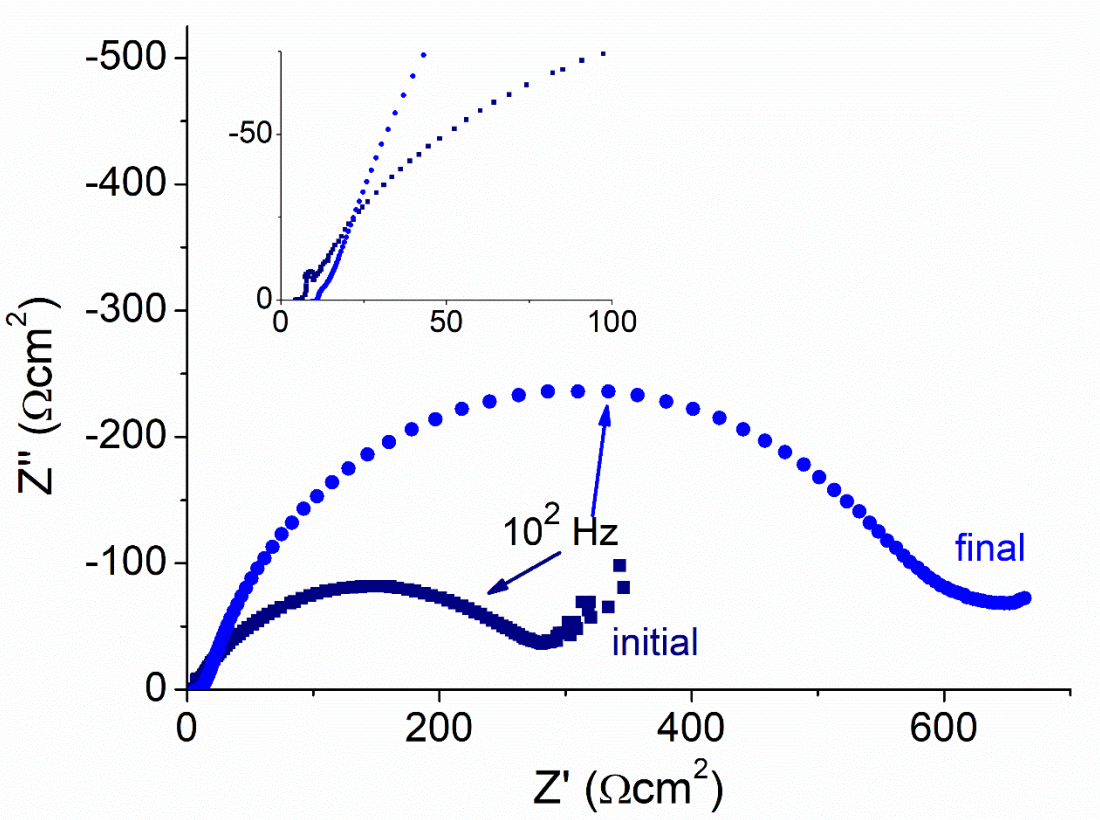

Figure 46. EIS pre- and post- cycling of lithium metal-thin dense LLZT-Celgard/$LiPF_6$ EC DEC-NMC 622 using CC-CV cycling.

6.5 Conclusions

Thin dense garnet electrolyte was successfully synthesized directly from low-reactivity precursors, pushing bulk synthesis methods towards the limit for non-thin film methods. Phase purity, microstructure, and effect of sintering environment was studied via XRD, SEM, and TGA/DSC. Extremely areal high rate of 75 mA/cm^2 was achieved in lithium symmetric cycling before failure. Lithium metal-NMC cells achieved 220 mAh/g at 0.1 mA/cm^2 and 160 mAh/g at 4 mA/cm^2 when using

asymmetric current cycling. Development of such thin garnet from simple precursors and bulk, scalable methods provide a single pathway to both lower materials cost while improving energy density and rate capability.

Chapter 7: Additional Works

7.1 Garnet Composition, its Effect on Select Thermal Properties and Secondary Phases, and the Minimization or Removal Thereof

7.1.1 Effect of Composition of Secondary Phases Present

When making ceramic structures one of the key metrics of is phase purity. Understanding phases present most often this comes through methods such as Rietveld refinement of XRD spectra after peak identification, Raman spectroscopy, and X-ray photoelectron spectroscopy. However all of these methods have crucial drawbacks. XRD typically requires the phases to be crystalline and a certain volume fraction of the material for the method to detect impurities. Thus non-crystalline, small crystals, or small volume fraction impurities are not well detected. Raman spectroscopy, while more fundamentally observing bonds through their excitations rather than diffraction, requires that the impurity is either easily enough visibly distinguishable via optical microscopy or prevalent enough that they are likely to be observed in random spot scans without causing fluorescence. SEM, especially with additional built-in methods such as backscatter mode and EDS, can be a powerful tool in discovering whether secondary phases are present and what element are present.

To illustrate this, Figure 47 shows a top-down view was taken of an LLCZT bilayer, on which several discolorations can be observed. These can be split into two different discolorations: wide, light gray disc-like phases and black fractal-like phases. EDS determined the first to be rich in calcium relative to the pure garnet grains, while the fractals only displayed carbon and oxygen in EDS indicating lithium carbonate given the detector's inability to detect lithium.

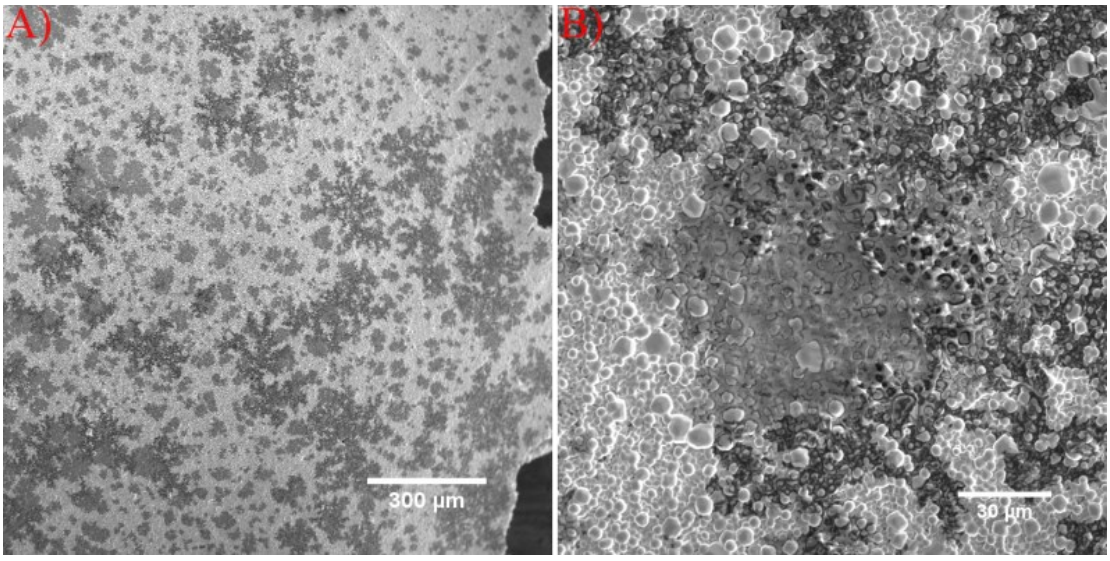

Figure 47. Surface SEM images of LLCZT bilayer A) and zoomed in image to display secondary phases present.

7.1.2 Effectivity of removal methods

In literature acid etching and a thermal annealing process called carbonate removal are used to aid lithium wetting via removal of surface carbonate species [72], [74], [75]. Figure 48 compares effects of carbonate removal and acid etching. After carbonate removal, one secondary phase remained readily observable on the garnet surface. EDS determined that despite the microstructure appearing similar to lithium carbonate, this phase was calcium rich. Cross-sectional SEM of the same sample displayed a new Zr-rich phase between grains. Taken together it would seem that calcium was likely leached from the sample resulting in some local breakdown of the garnet-structure. Initial 90 second etching using diluted HCl, secondary phase was not readily observed. However, the sample had over-etched resulting in significant void formation in dense layer rendering the bilayer not usable.

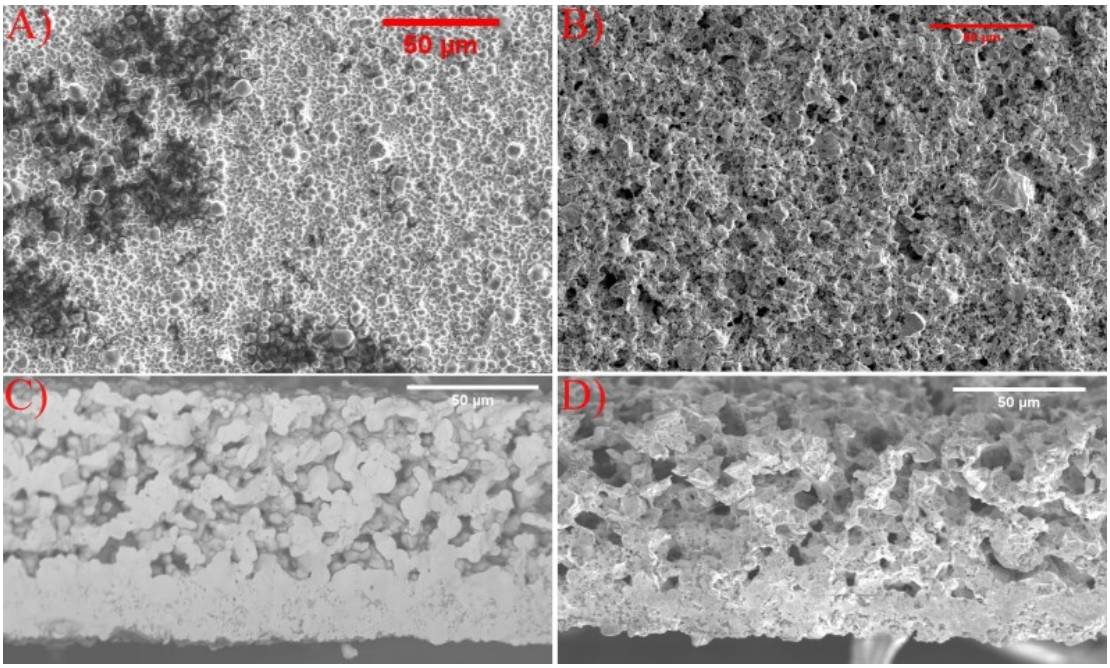

Figure 48. Surface and cross-sectional images of bilayers after carbonate removalA) and C) and after HCl acid etching B) and D).

Longer sintering time displayed significant reduction of observable secondary phase in Figure 49. Only one clearly distinguishable secondary phase remained which appeared as a nearly black islands in backscatter. Utilizing LLZT instead of LLCZT did not result in a lack of secondary phase, instead changing the chemical and microstructural nature of present secondary phases. Noticeably the new secondary phase it nearly plate-like in shape, while in backscatter, the phase is whiter than the garnet grains instead of darker. EDS determined that the new phase was La-rich instead of Ca or C and O rich which tracks with the backscatter observations.

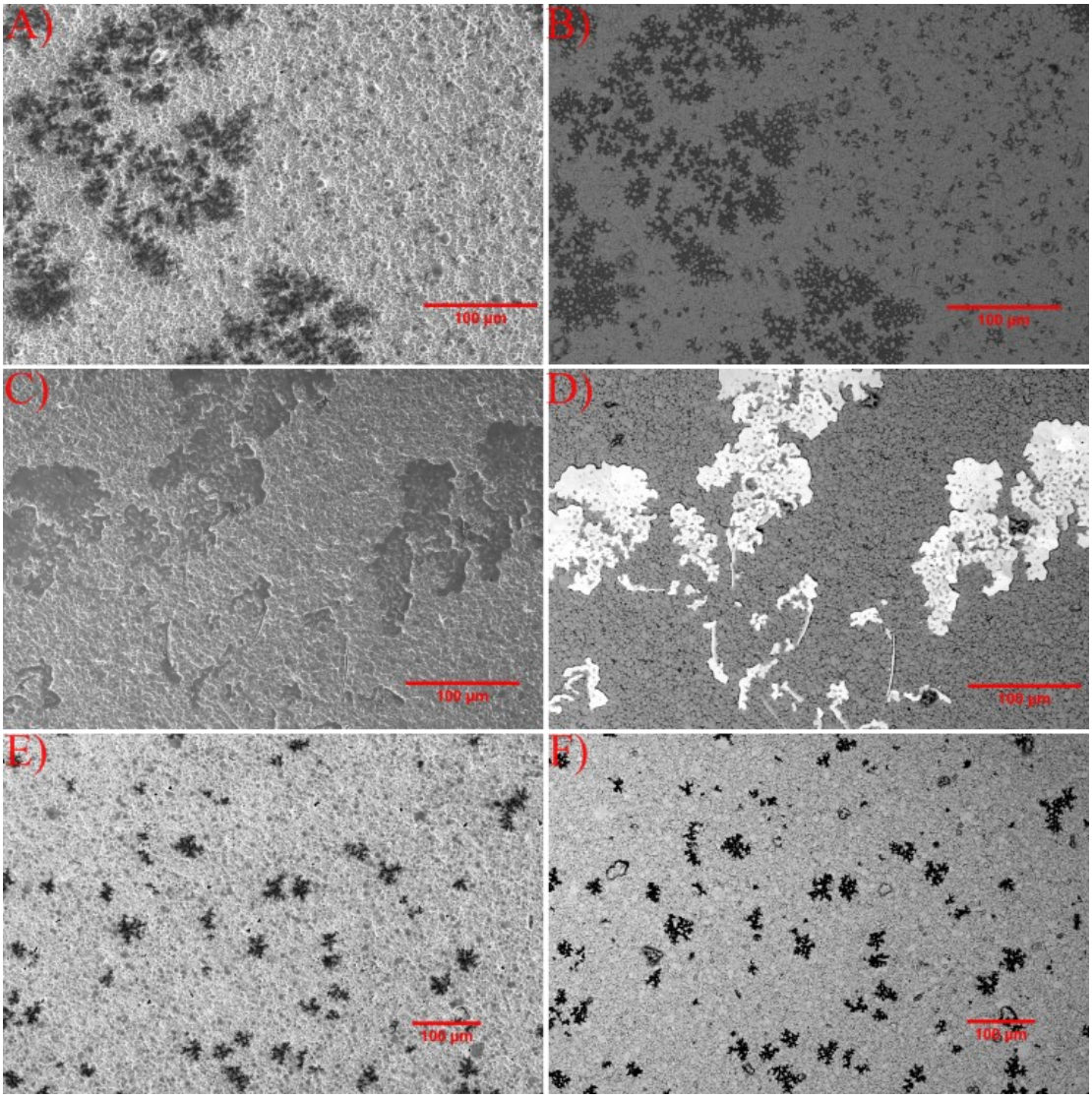

Figure 49. Surface SEM and back-scatter SEM for LLCZT (A) and B)), LLZT (C) and D)), and 4 hour sintered LLCZT (E) and F)).

7.1.3 Formation in LLZT

To better understand La-rich secondary phase, the same tapes were laminated and sintered on the same powderbed for varied sintering times. At 2 hours, the cross-section of the structure displays a persistence of voids remaining in the dense layer. Although no secondary phase was clearly distinguishable in cross-section, imaging of the top surface clearly displays the smooth, plate-like structures previously shown as

lanthanum rich. The microstructure from 3 hour sintering remained largely the same, with the main noticeable difference being the fracture pattern now having vertical rather than horizontal lines. The surface SEM displayed at this time shows similar remnant La-rich phases of those discussed in previous sintered samples, which is to say far less than that of the 2 hour sample. Given the TGA discussed in previous sections of this work and the seemingly preferential nature of this secondary phase for surface and grain boundary segregation, the secondary phase appears to be a remnant of the liquid phase sintering of garnet.

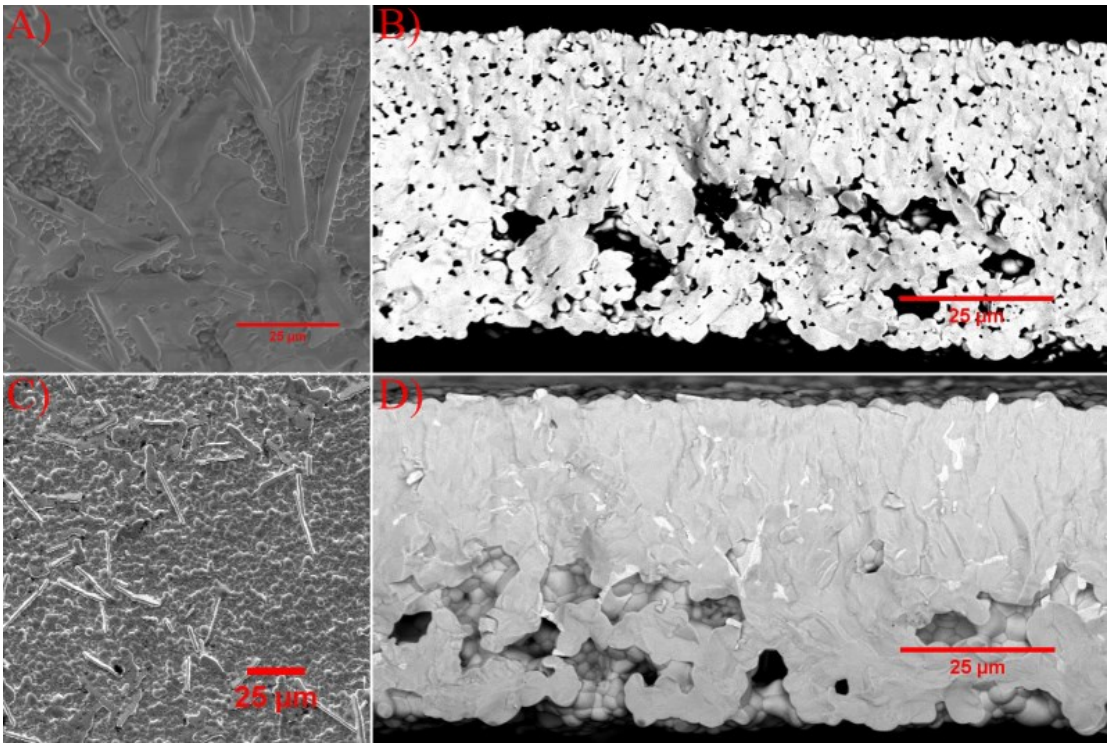

Figure 50. Surface SEM and cross-sectional backscatter SEM of LLZT bilayer sintered for 2 hours, A) and B), and 3 and a half hours, C) and D).

7.1.4 Samarium doping

To lessen the potential effect of lanthanum absorbing carbonate and having difficulty leaving the melt to integrate back into the garnet structure, a small fraction

of the site was doped with samarium. In the cross-section imaging performed, densification was achieved, with a reduced amount of observable secondary phase via backscattering. Imaging of the dense surface of samarium doped garnet really displays the drastic reduction in secondary phase observable. Large plate of the secondary phase were observed, with only small islands of light phases observed in backscatter. EDS of these regions again displayed a lack of elements from the zirconium site, but clear signals from the Lanthanum and even Samarium.

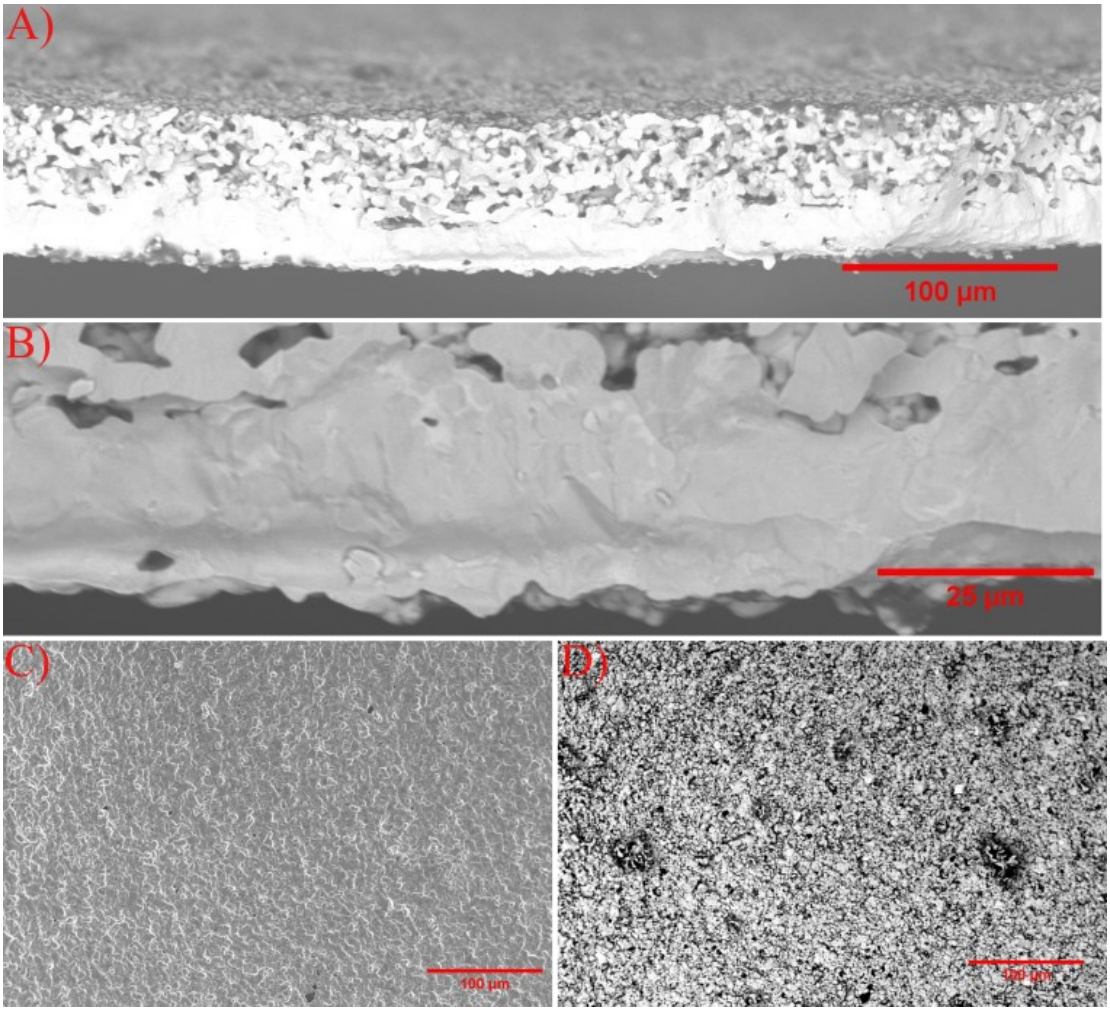

Figure 51. Low-samarium doping garnet bilayer with wide cross-sectional backscatter (A), higher-magnification cross-sectional backscatter (B), and SEM and back-scatter SEM of the surface, C) and D) respectively.

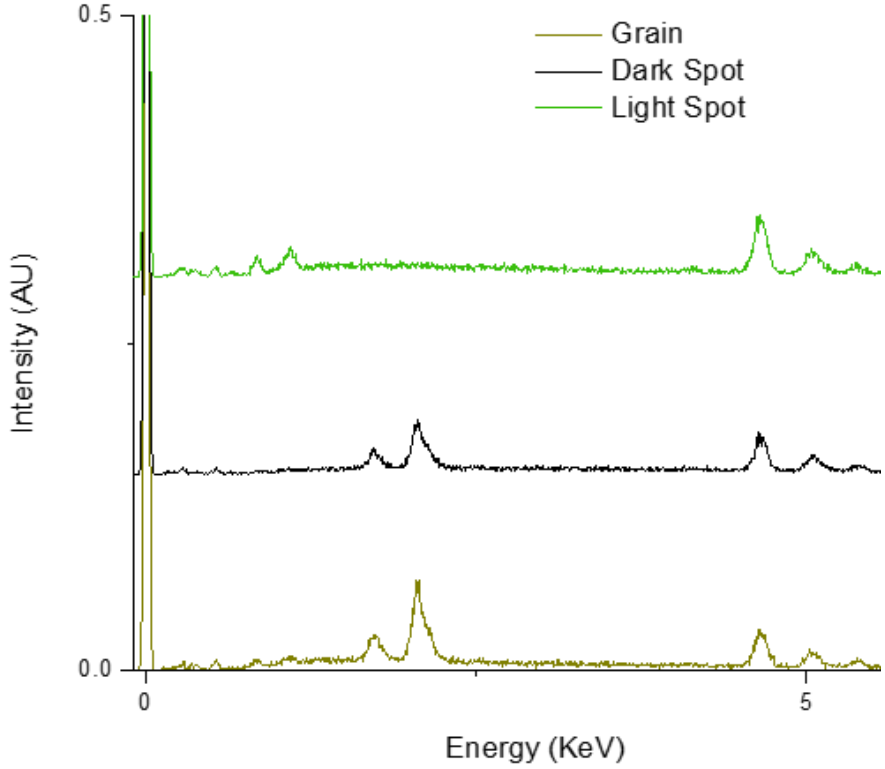

Figure 52. EDS spectra for phases observed in samarium-doped garnet bilayer.

7.2 Hydrophobing

As previously discussed, garnet in atmosphere is prone to reactions creating unfavorable surfaces for electrochemical purposes. Key to the reaction mechanism is the highly polar surface of garnet's affinity for water, without which formation of lithium carbonate is unfavorable. The effect that this might have on sintering of garnet powder or if this is fully reversible in sintered garnet left out for significant time has yet to be studied fully. While many methods have been used to remove surface lithium carbonate from sintered garnet, only a few of these methods have demonstrated a continued resistance to re-formation of this carbonate layer. One method used in certain

metals industry to avoid reaction with water is hydrophobing its surface through reaction of the metal with fatty acids to repel water.

7.2.1 Reaction Time

Contact angle between unreacted garnet and the pellet reacted for 45 minutes in Figure 53A and B display a stark contrast. The unreacted garnet is easily wet by water while the pellet reacted for 45 minutes displayed a fairly high contact angle. Further increasing reaction time to overnight, approximately 16 hours, in Figure 53C shows a similarly high contact angle to the 45 minute sample indicating that the increased time likely would not further improve resistance to water. In fact, XRD of the pellets indicated the presence of lithium stearate on both the 45 minute and overnight samples. Thus it appears that even at 45 minutes the reaction likely exceeded simple surface coating and could be further optimized to lower reaction times.

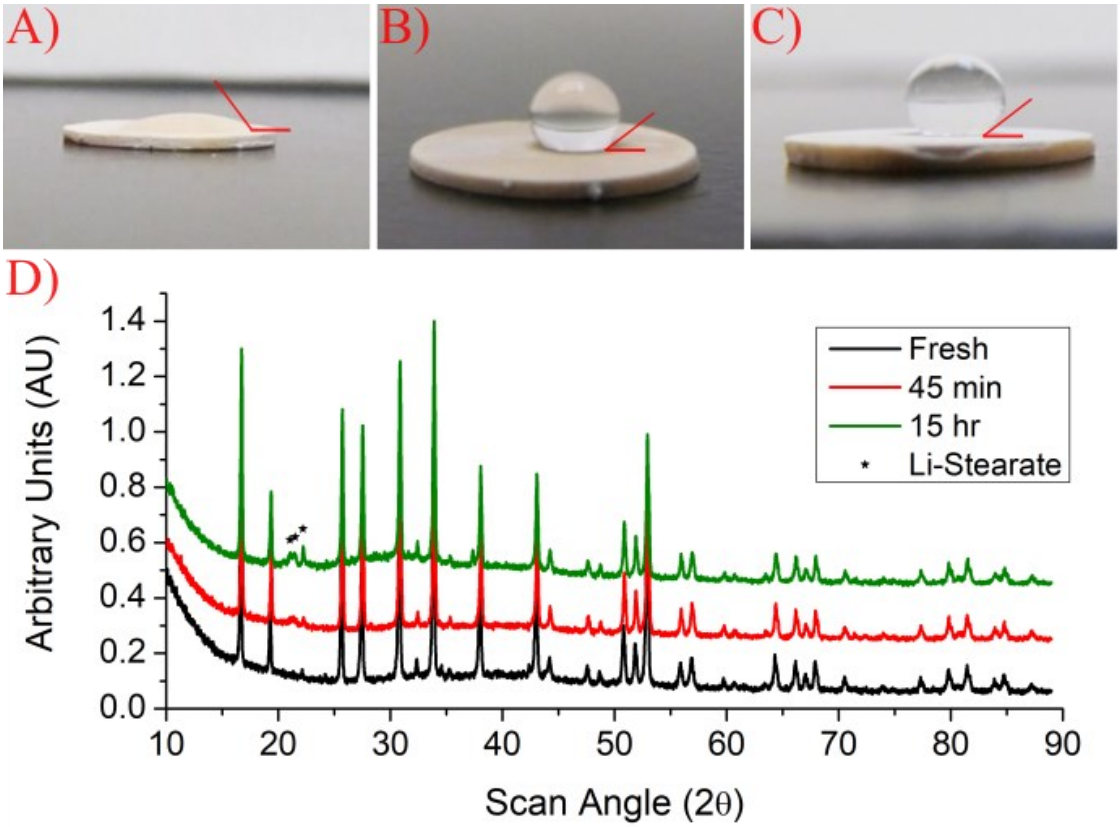

Figure 53. Water-drop contact angle for as-sintered garnet, 45 minute B) and 15 hour C) stearic acid hydrophobed garnet, and XRD spectra for the same D).

7.2.2 Ligand Choice

Three additional fatty acids were selected to display effects of different ligands protecting garnet surfaces: oleic, lauric, and fish oil. Oleic, like stearic acid, is an 18-carbon chain fatty acid, but is monounsaturated. Lauric is fully saturated like stearic, but is only a 12-carbon chain. While maheden fish oil is composed of a wide array of saturated and unsaturated fatty acids of varied length[161]. The images taken of water dropped onto hydrophobed garnet surfaces display large change in contact angle in Figure 54. Stearic acid has the largest contact angle, followed by lauric, oleic, and finally fish oil. As expected, this shows that more lipophilic ligands increase the surface's repulsion of water.

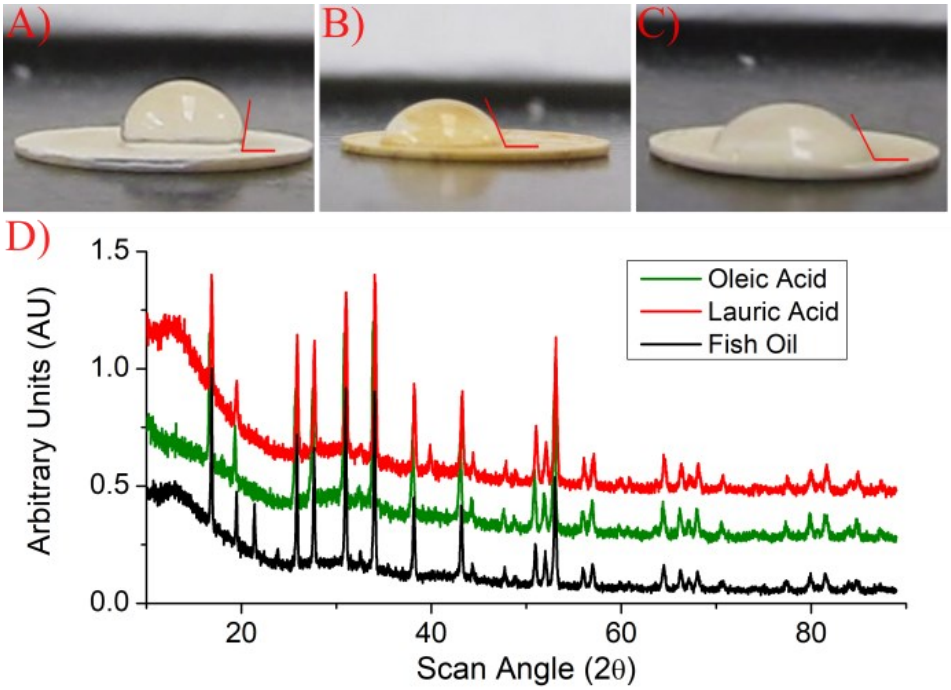

Figure 54. Water-drop contact angle for A) oleic acid hydrophobed garnet, B) fish oil hydrophobed garnet, C) lauric acid hydrophobed garnet, and D) XRD spectra for the same.

Oleic	12.9172(5)
Lauric	12.9210(5)
Fish	12.9379(4)

7.3 Stabilizing High Voltage Spinel with Thin dense Garnet

$Li_{1.075}Ni_{0.35}Mn_{1.5}Cr_{0.075}O_4$ (NMCr) powder, provided by ARL was cast as previously discussed with LFP, with super P and PVDF at a ratio of 85:7.5:7.5. Single discharge-charge plateau behavior was observed with significant IR loss between the two. Initial discharge capacity of 60 mAh/g was observed, with large capacity loss per cycle thereafter. Given the voltage window for standard liquid electrolyte, such fast capacity decay is to be expected.

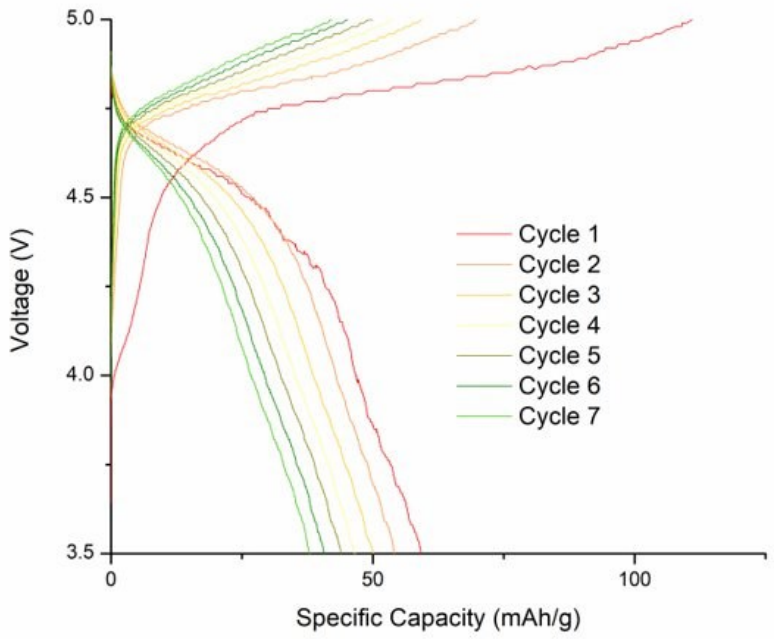

Figure 55. Voltage profile for cycling Li metal-thin LLZT-1 M$LiPF_6$ EC/ DEC/ Celgard-NMCr.

Modifying the standard electrolyte with 2 weight percent of either FEC and TEP led to significant capacity improvements. 2% TEP addition brought out the second, lower voltage plateau on both discharge and charge for the first two cycles. FEC addition, while not as successful in stabilizing the second plateau, more drastically increased discharge capacity to 130 mAh/g on its first two cycles. Looking at the precycling EIS of these cells, it is immediately apparent that the electrolyte additions behaved much differently at all interfaces present. FEC has the much lower x-intercept, and therefor the higher conductivity liquid. The cell with TEP in the catholyte, however, has a lower total initial resistance. DRT of this impedance further shows confirms that TEP resulted in elevated resistances at high frequencies -such as SLEI.

FEC had higher cathode-liquid interfacial resistances, which may help explain the greater prevalence of the second voltage plateau in the TEP sample than FEC.

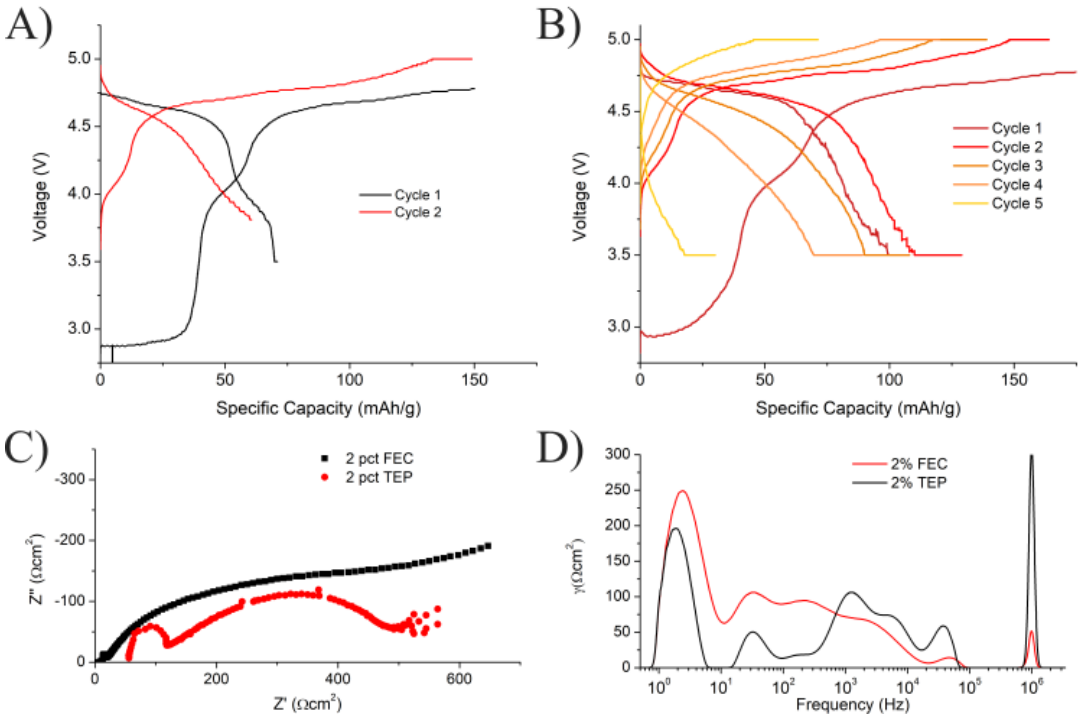

Figure 56. Voltage profiles for cells using A) TEP and B) FEC additives and C) EIS and D) DRT comparing the two cells.

7.4 Synthesizing and Integrating porous MIEC with thin dense Garnet

7.4.1 Sintering thin MIEC

Thin, porous MIEC tapes were prepared via tape-casting the precursor materials after milling it down to the desired particle size. LGPZN was sintering at 900 ℃ for 45 minutes, mirroring the porous LLZT from previous chapters. Epoxy-filled back-scatter SEM was employed to increase contrast between MIEC and pore volume precisely through using ImageJ software to determine porosity. The initial tape, with no added pore-former as seen in Figure 57, was determined to be 6 μm and 72 % porous.

Lamination of this tape scaled well as seen in Figure 57B, which retained high porosity of 74 % and a thickness of 12 µm. In order to increase porosity further, cross-linked PMMA pore-former was added to MIEC tapes as done in our group's more traditional bi- and tri-layered garnet. The resultant sintered MIEC in Figure 57C was too thick at 27 µm but had increased porosity up to an average of 82%. This could be scaled to thinner garnet, as seen in Figure 57D which retained 81 % porosity when scaled down to 17 µm.

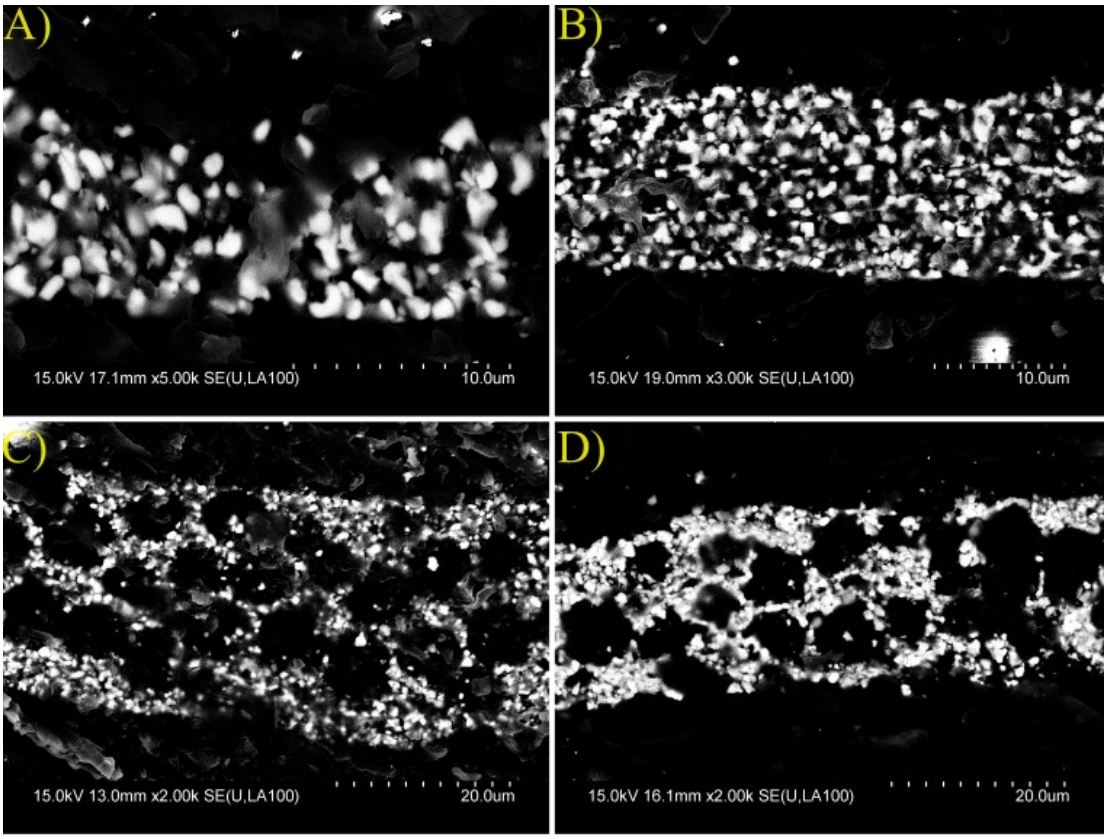

Figure 57. Epoxy-filled SEM image of thin, porous, stand-alone Nb-LGPZ for A) initial, B) laminated, C) pore-former introduced, and D) thinner sample with pore-former.

Similarly, porous Ce-LGPZ was sintered under both O_2 and Ar at 850°C for 45 minutes, with the resulting structures seen in backscatter in Figure 58. Both structures were highly porous (~80%), though the O_2 sintered sample had significant observable

dark secondary phase. XRD of these samples showed no garnet character in the O_2-sintered sample, while the argon-sintered sample appeared largely cubic phase garnet with some contribution of affixing clay used in the XRD testing (Figure 58).

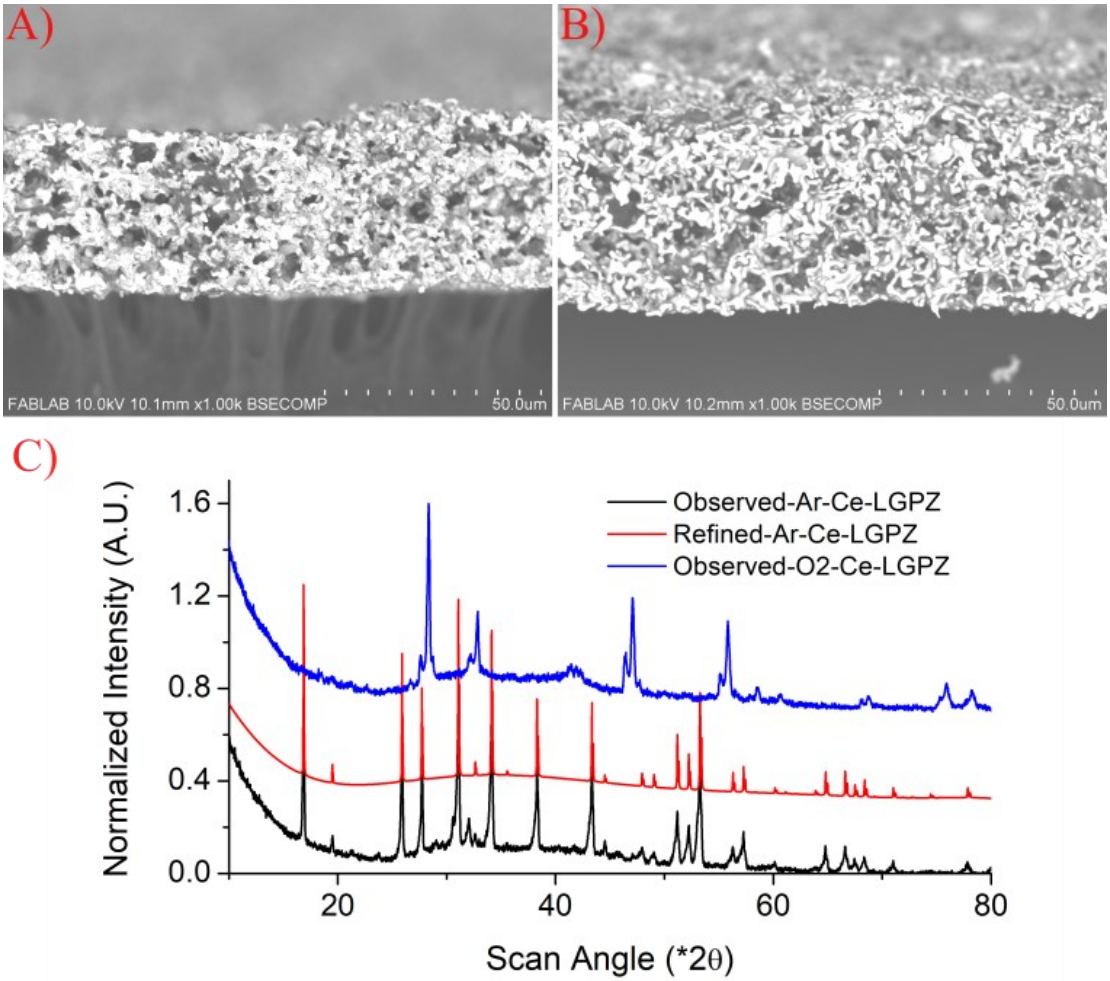

Figure 58. Backscatter SEM image of porous Ce-LGPZ sintered in A) O2 and B) Ar along with C) XRD spectra of the two.

7.4.2 Matching sintering temperature

Thin LGPZN MIEC structures were observed to fully collapse in the presence of excess lithium by 1050℃ as seen in Figure 59, with some gray secondary phase observed in backscatter. This was below the sintering temperature previously required

for thin LLZT of 1115℃. Given this disparity, a series of dopants was tested to correct this issue.

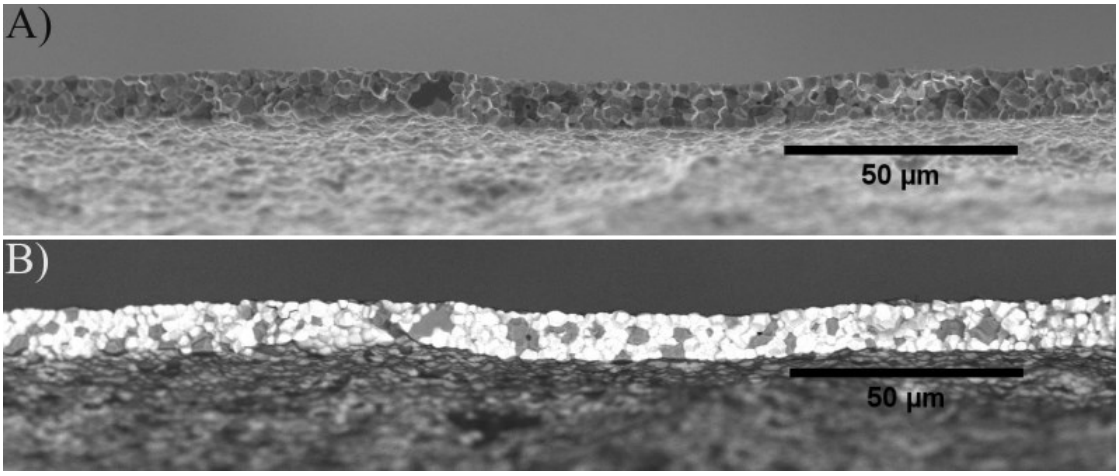

Figure 59. A) SEM and B) back-scatter SEM of thin LGPZN tape sintered at 1050℃ for 3 hours with lithium carbonate-magnesium oxide powderbed.

This collapsing behavior was further studied using TGA/DSC, with the DSC results highlighted in Figure 60. Comparing just LLZT and LGPZN under O_2 flow in Figure 60B, initial melt is observed for LGPZN before LLZT around the Li_2CO_3 melting temperature. This is likely due to gallium reacting similarly to the aluminum dopant discussed in the introduction forming of lithium-gallium oxides, such as the Li_5GaO_4 observed by Rawlence et al[162]. Additionally, A longer secondary shoulder is observed, related to either or both of niobium's replacement of tantalum or praseodymium for lanthanum. Increasing local lithium environment through additional lithium carbonate to simulate powderbed resulted in a distinct and dominant lithium carbonate melt peak. Despite its relatively small nature, the lower temperature peak can still be observed from in the higher lithium sample. Interestingly, changing sintering environment to argon not only shifted the peaks but changed the entire shape of the endotherm. Three distinct peaks occur under argon for LGPZN with the highest temperature of these peaks occurring roughly where the low-temperature melt was

observed under O_2 flow. Taken in conjunction with the previously discussed color change, some change in charge, likely praseodymium, seems to occur that may help stabilize the garnet phase.

LGPZC under O_2 flow had a low-temperature melting temperature more reminiscent of LGPZN under argon, though an overall shape likely that under O_2. The endotherm retains the initial shoulder observed for LGPZN that ends around 850 °C, proving that this shoulder is related to praseodymium in the garnet melt rather than niobium. An additional shoulder is observed for LGPZN extending to around 1050°C, which in addition to the low temperature early melt indicates cerium may be more active in the melt than niobium.

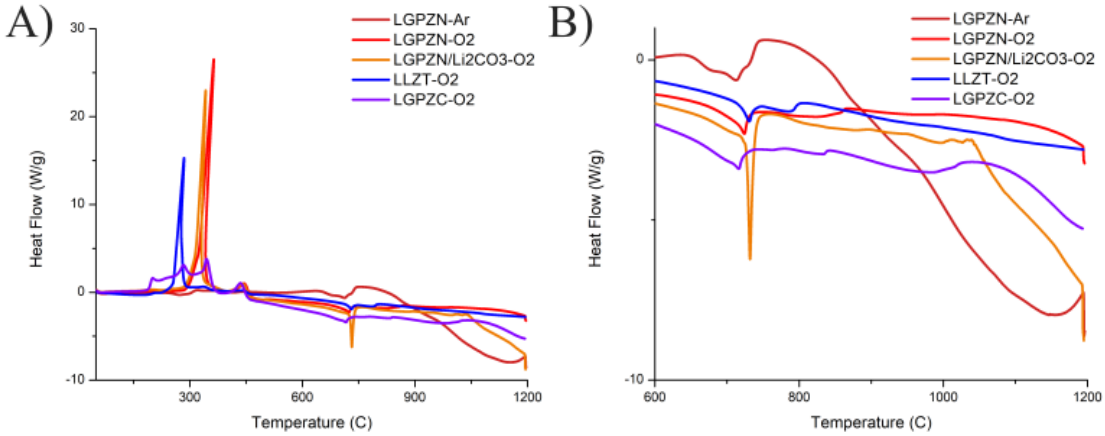

Figure 60. A)Full-scan and B) zoomed-in portion of DSC comparing LGPZN with LLZT and LGPZC.

7.4.2.1 Low Temperature sintering

Following the low temperature sintering of LGPZN and the change in DSC curve between it and LLZT, a series of dopants were chosen to lower dense layer sintering temperature to better match. DSC of this series was taken as an initial measure to discover compatable tapes as shown in Figure 61. The most basic of these of only gallium doped garnet, LGLZ, similar shift in initial melting temperature is observed in

Figure 61B, as occurred for LGPZN. This is significantly lower than the carbonate melting temperature observed for LLZT, agreeing with the previous assertion that the shift observed for LGPZN in air was related to gallium. The second peak approximately 50°C higher than the carbonate peak is largely similar to the one seen in LLZT, indicating it relates to lanthanum's incorporation into the melt.

With the importance of gallium to lowering melting temperature established, co-dopants were studied. Niobium co-doped garnet (LGLZN) displayed an initial carbonate melting temperature inbetween LGLZ and LLZT. The secondary lanthanum peak was retained, with greater separation from the carbonate peak than either LGLZ or LLZT. Furhter an additional smaller peak at slightly higher temperature than occuered in addition to a long shoulder extending to around 1050°C, simlar to LGPZN. Addition of calcium to this system (LGLCZN-1) slightly lowered the initial carbonate peak, while lowering the lanthanum peak. Additionally, the peak associated with niobium introduction became a less distinct peak. For reasons later discussed, a second gallium, niobium, and calcium sample was prepared with lower gallium content (LGLCZN-2). This lowered the initial carbonate peak back to the temperature for LGLZ and moved caused the secondary peak to become far closer to the carbonate peak in temperature. The long shoulder extending to 1050°C also became more distinct. Tantalum co-dopant (LGLCZT) was also tested to replace the niobium from LGLCZN-2.This largely retained the same DSC curve as LGLCZN-2, though the entire curve following the carbonate peak, and especially where the long shoulder is observed, was far less endothermic.

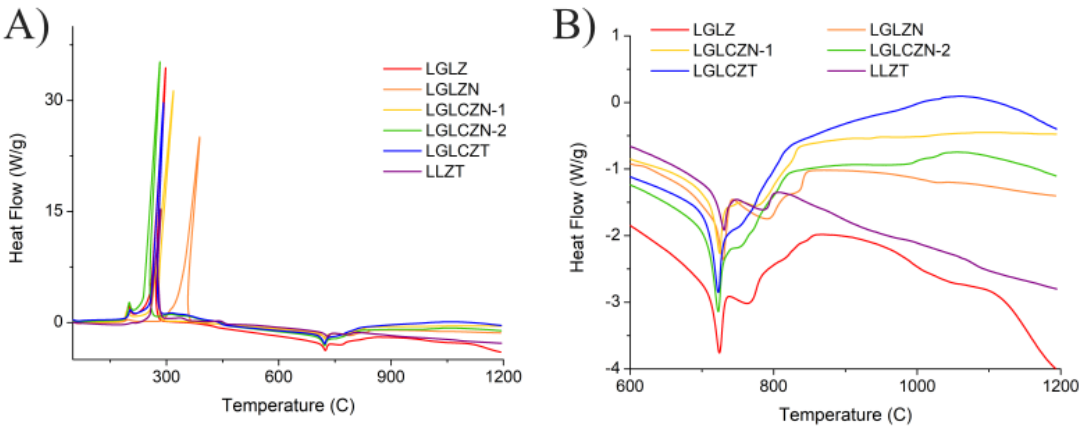

Figure 61. A) full scan and B) zoomed-in scan around melting and sintering temperatures for a series of lowered sintering temperature dense garnets.

Gallium-doped, or LGLZ, sintered densely, as seen in Figure 62A, though with a significant amount of dark secondary phase in backscatter. XRD of this material found tetragonal garnet, but the secondary phase did not readily appear in the spectra. This discrepancy in secondary phases could relate to non-crystallinity or low volume percentage. Gallium, niobium co-doped (LGLZN) and both gallium, niobium, and calcium co-doped garnets (LGLCZN-1 and LGLCZN-2) similarly sintered densely in the back-scatter in Figure 62B-D. LGLZN displayed similar dark secondary phase as LGLZ, while LGLCZN-1 and -2 both had significantly less secondary phase. Figure 62E shows cubic phase garnet for LGLZN, LGLCZN-1, and LGLCZN-2 with only some affixing clay observed in the spectra due to the thinness of the samples.

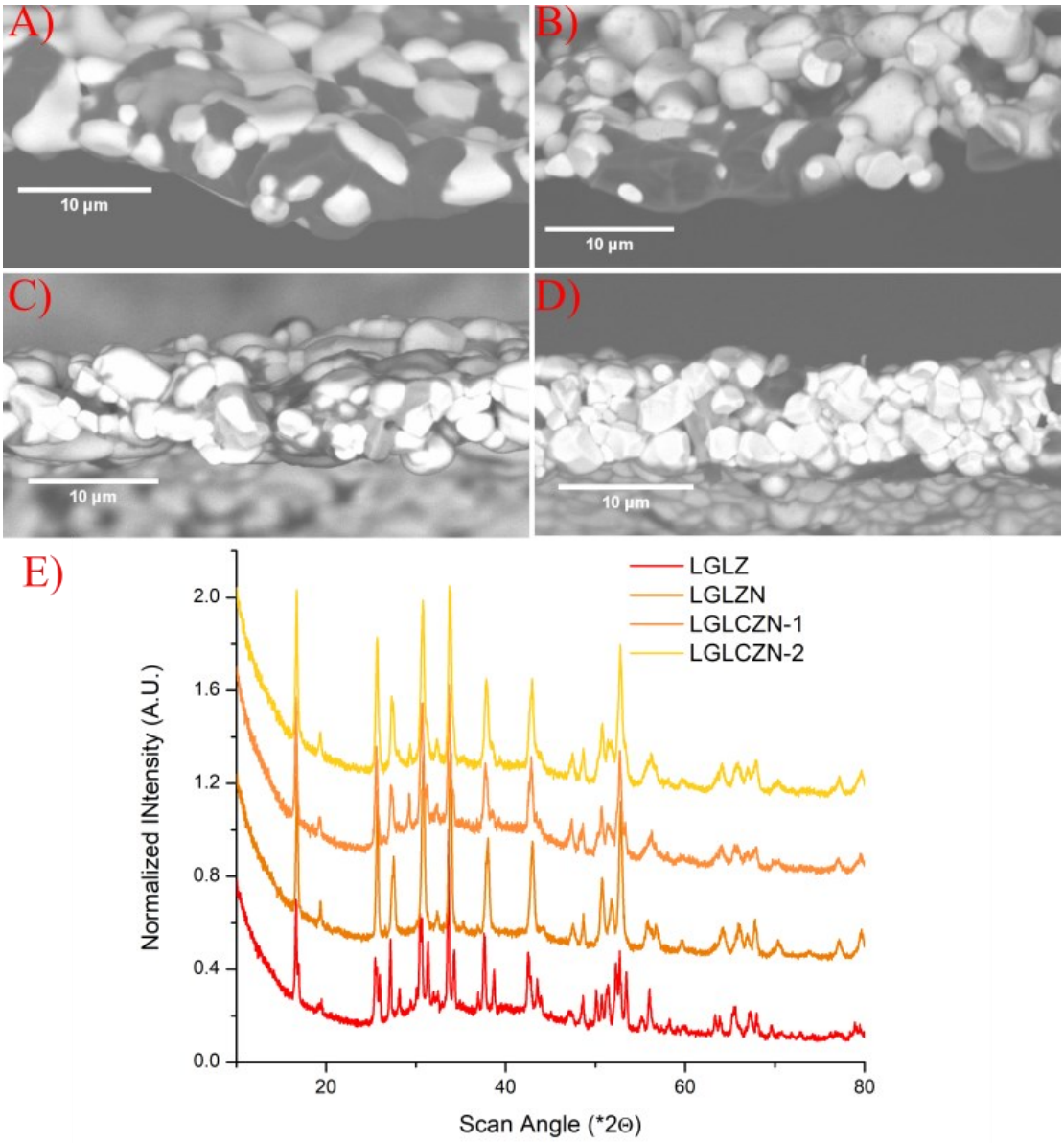

Figure 62. Backscattered SEM images of A) LGLZ, B) LGLZN, C) LGLCZN-1, and D) LGLCZN-2 along with XRD of said samples sintered at 1000°C.

EIS and DC polarizations were performed on this low-temperature sintering garnet, displayed in Figure 63, as was performed in previous chapter with thin LLZT using gold electrodes. Projected X-intercept from EIS indicates an ionic conductivity of $6*10^{-5}$ S/cm, lower than that of LLZT. DC polarization indicated an electronic conductivity of $2*10^{-11}$ S/cm. While this means that the lithium conductivity is lower

than LLZT, the ratio of ionic to electronic remains approximately the same. Thus this new composition should remain a viable conductor.

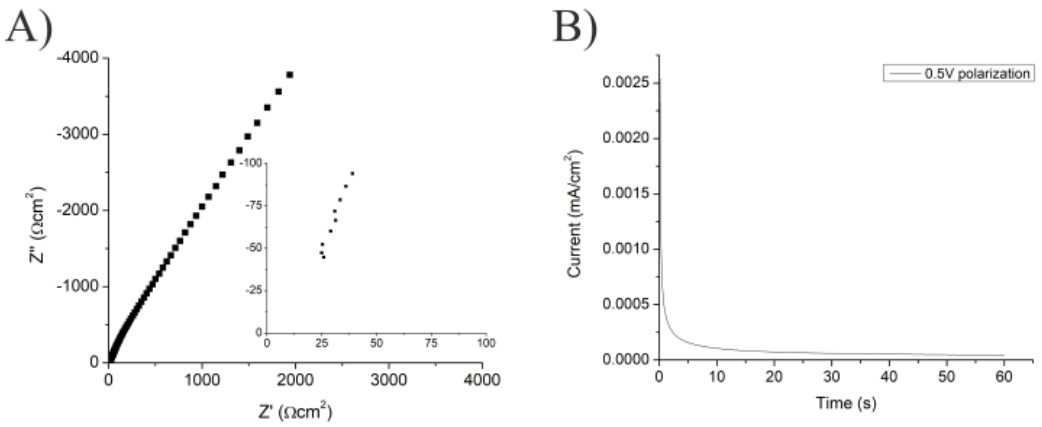

Figure 63. A) EIS and B) DC polarization for sintered LGLCZN-2 sample using gold electrode with silver leads.

Utilizing a gallium and niobium co-doped garnet with niobium-doped MIEC, the bilayer in Figure 64A was sintered with a highly dense 4 µm thick dense layer and 65 % porosity 16 µm thick Nb-LGPZ MIEC layer. Top-down imaging in Figure 64B and C reveals good surface porosity in the MIEC layer and a lack of pinholes in the dense. However, the dark coloration remaining in the dense layer (Figure 64 **C**) shows remaining secondary phase, similar to that observed this dense layer composition as a stand-alone garnet.

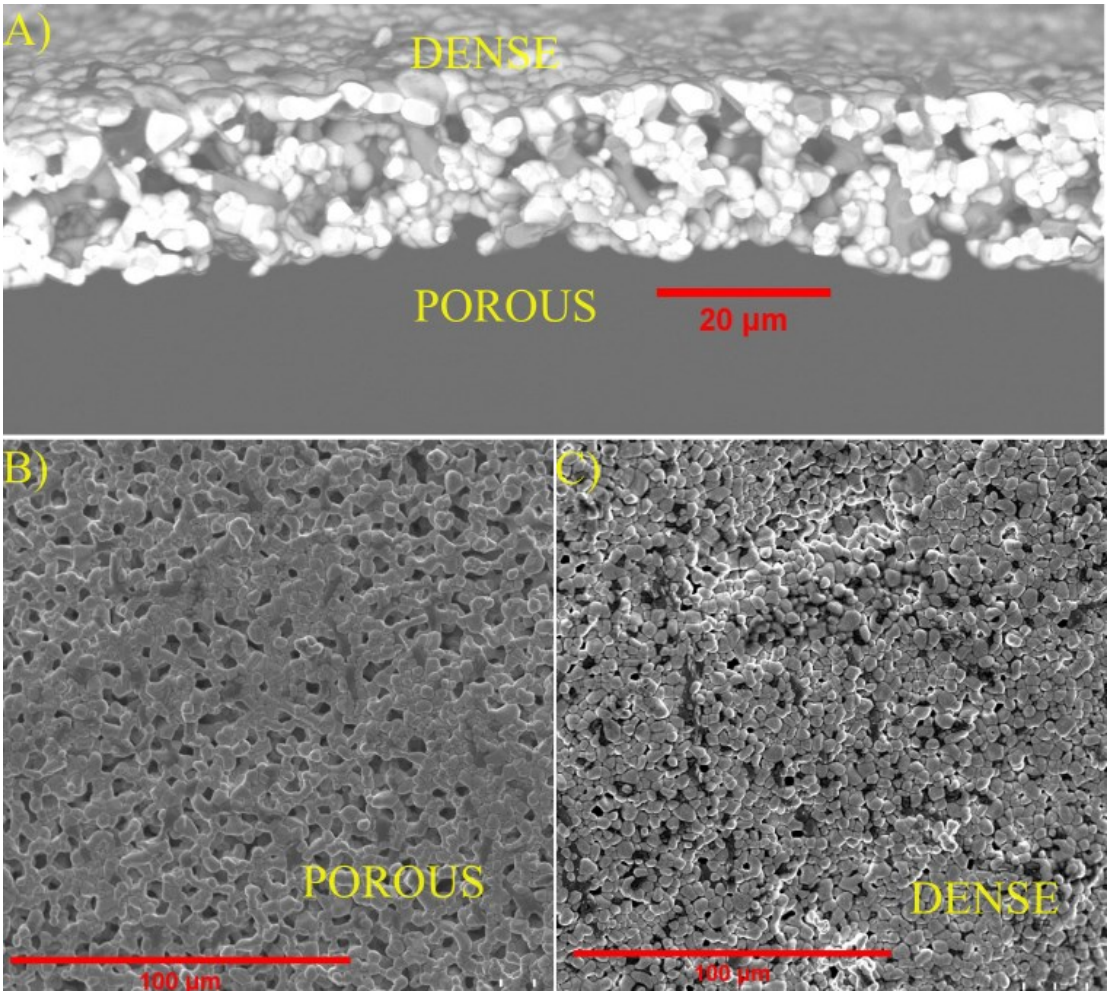

Figure 64. A) Cross-sectional, B) porous surface, and C) dense surface SEM of LGLZN-MIEC(Nb) bilayer.

To deal with the secondary phase, gallium, calcium, and niobium co-doped garnet (LGLCZN) was utilized as the dense garnet layer. Similarly, a bilayer was fabricated with 65 % porous Nb-LGPZ MIEC layer with highly dense LGLCZN layer at 9 and 3 µm thicknesses respectively as shown in Figure 65A. Top-down imaging again showed good surface porosity in the Nb-LGPZ MIEC layer (Figure 65B) and pin-hole free dense structure (Figure 65C). It is also worth to note that the dense layer did not retain the secondary phase observed in the non-calcium doped sample.

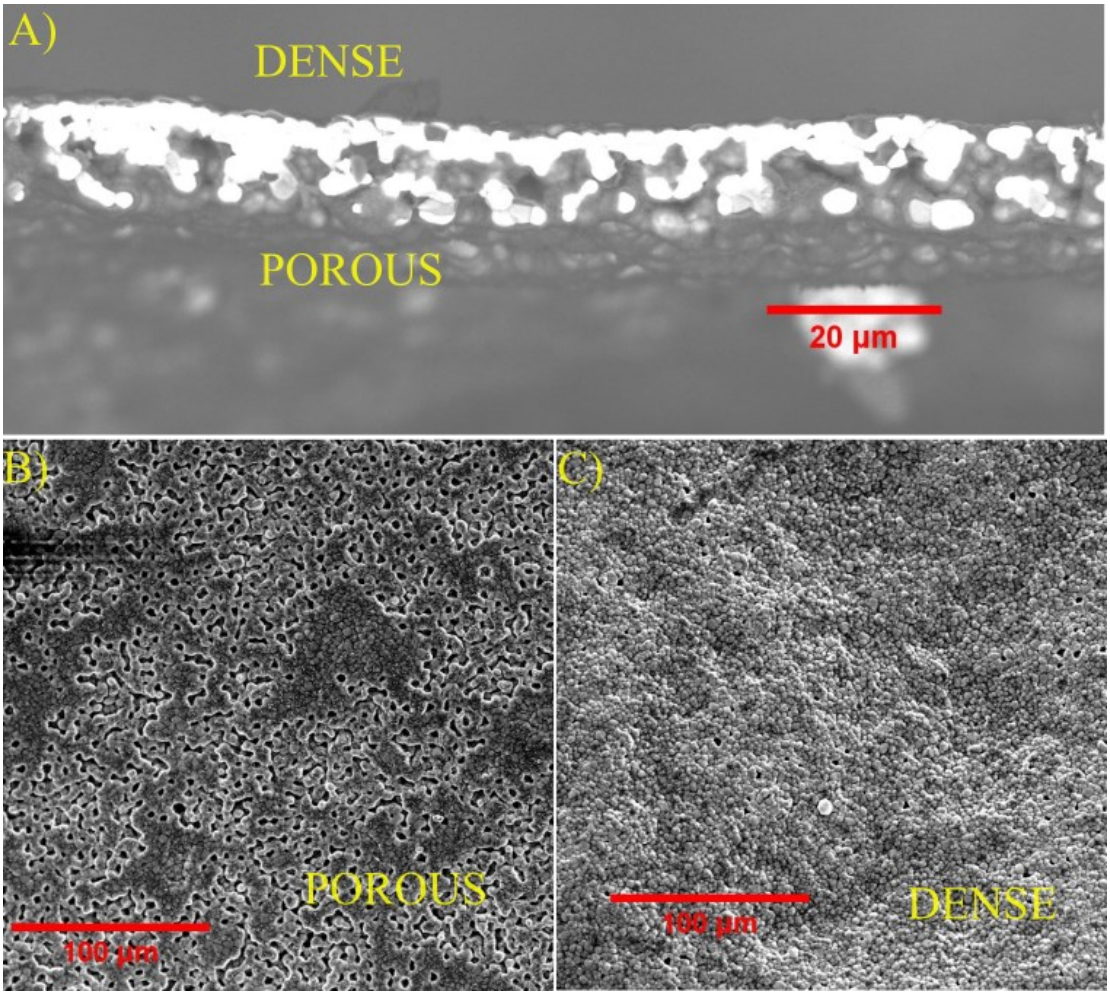

Figure 65. A) Cross-sectional, B) porous surface, and C) dense surface SEM of LGLCZN-MIEC(Nb) bilayer

Using the thin LGLCZN-2 and thin bilayer using dense LGLCZN and porous LGPZN MIEC layer, from Figure 62 and Figure 65 respectively, full cell were assembled. Al_2O_3 was ALD coated on the porous side, and lithium metal wet onto the surface as previously described. Minimal (~ 4 µl) of 1M $LiPF_6$ in EC: DEC liquid electrolyte was added to NMC cathode. Celgard was placed between NMC cathode and the dense layer to improve the mechanical support, as with the thin dense LLZT work. Constant current-constant voltage charge and discharge profiles were used.

Using the thin LGLCZN dense garnet high capacity, 173 mAh/g, was reached at 0.084 mA/cm^2 as observed in Figure 66. Minimal capacity drops were observed with increased rates 0.17 and 0.34 mA/cm^2, at 173 and 165 mAh/g respectively. Sudden capacity loss was observed upon further rate increase to 0.48 mA/cm^2 along with sudden low coulombic efficiency. Both of these values increased when rate was further increased to 0.72 mA/cm^2.

Figure 66C shows that after the initial high capacity of 177 mAh/g observed at 0.085 mA/cm^2, discharge capacity achieved drops significantly, followed by more steady decline upon further rate increases at 145, 133, 126, 121, and 115 mA/g with respective rates of 0.35, 0.48, 0.98, 1.5 and 2 mA/cm^2. The loss of capacity is tied closely with the increasing over-potential seen through initial charging voltage in Figure 66 C. Upon returning to 0.35 mA/cm^2 the discharge capacity was still only in the range of ~ 110 mAh/g, however the coulombic efficiency was always close to 100%. The poor rate capability could possibly due to the low ionic conductivity of the new composition dense layer and the thinness of the porous layer. In the upcoming quarter, we will perform studies on the optimum thickness of the porous and dense layer to achieve low areal specific resistance. Also, to improve the mechanical support, brazing of bilayer to the metal current collector will be done and more cells will be tested in the following quarter.

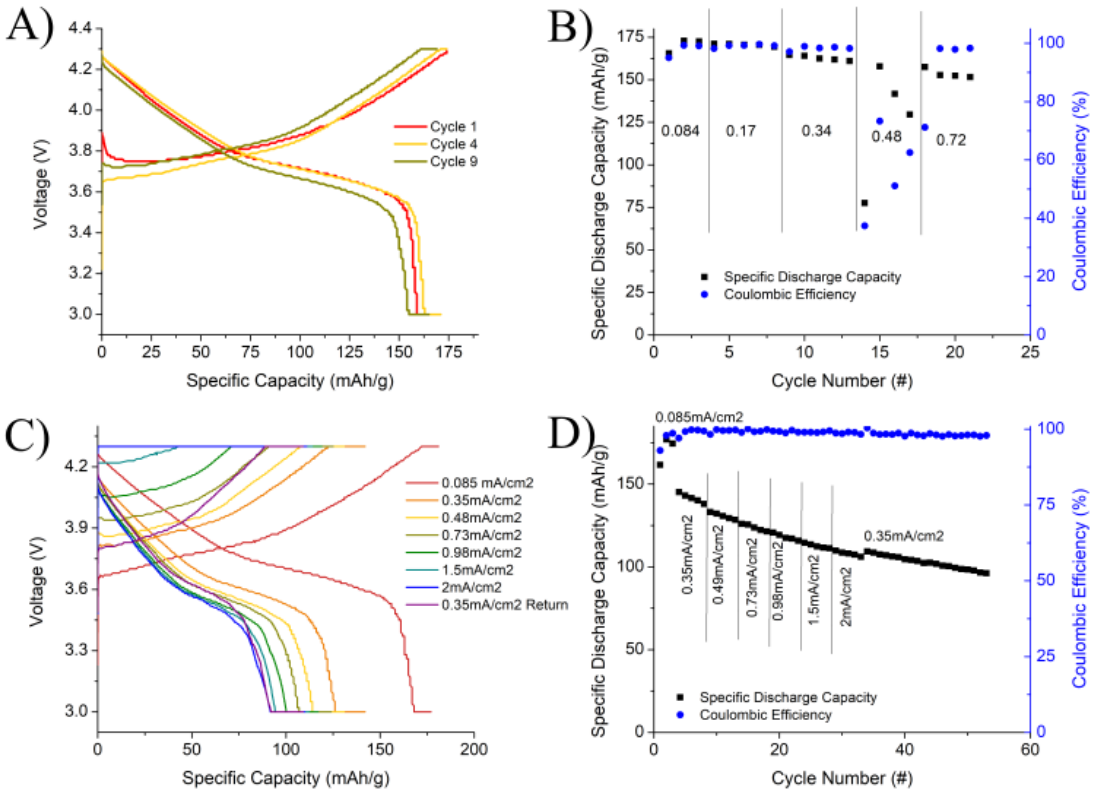

Figure 66. Voltage profiles and discharge capacity and coulombic efficiency for lithium metal-thin LGLCZN-celgard/1 M $LiPF_6$ EC/DEC-NMC622 A) and B) and lithium metal-thin bilayer-celgard/1 M $LiPF_6$ EC/DEC-NMC622 cell C) and D).

7.4.2.2 Interlayer

Tapes with varied praseodymium content were cast to test its effect on sintering and ability to limit praseodymium and multivalent ion diffusion into the dense layer. Tapes were cast with praseodymium content of $Pr_{0.1}$, $Pr_{0.4}$, $Pr_{1.5}$, and Pr_2, by mixing the following powders in the respective ratios: LGLCZT-MIEC(Nb) at 2.9:0.1, LGLCZN-MIEC(Nb) at 2.6:0.4, LLZT-MIEC(Nb) at 1.5:1.5, and LLZT-MIEC(Nb) at 1:2. These were laminated with LLZT thin dense tape and the resulting trilayers, sintered at 1100 °C, are displayed in Figure 67. Pr0.1 trilayer, in Figure 67A, achieved a highly dense and intra-granular dense layer while retaining good porosity in the porous layers. $Pr_{0.4}$,

shown in Figure 67B, fully collapsed, with extremely high intra-granular fracture akin to what was observed during sintering of LLZT-A with MIEC(Nb) seen in Figure 67C.

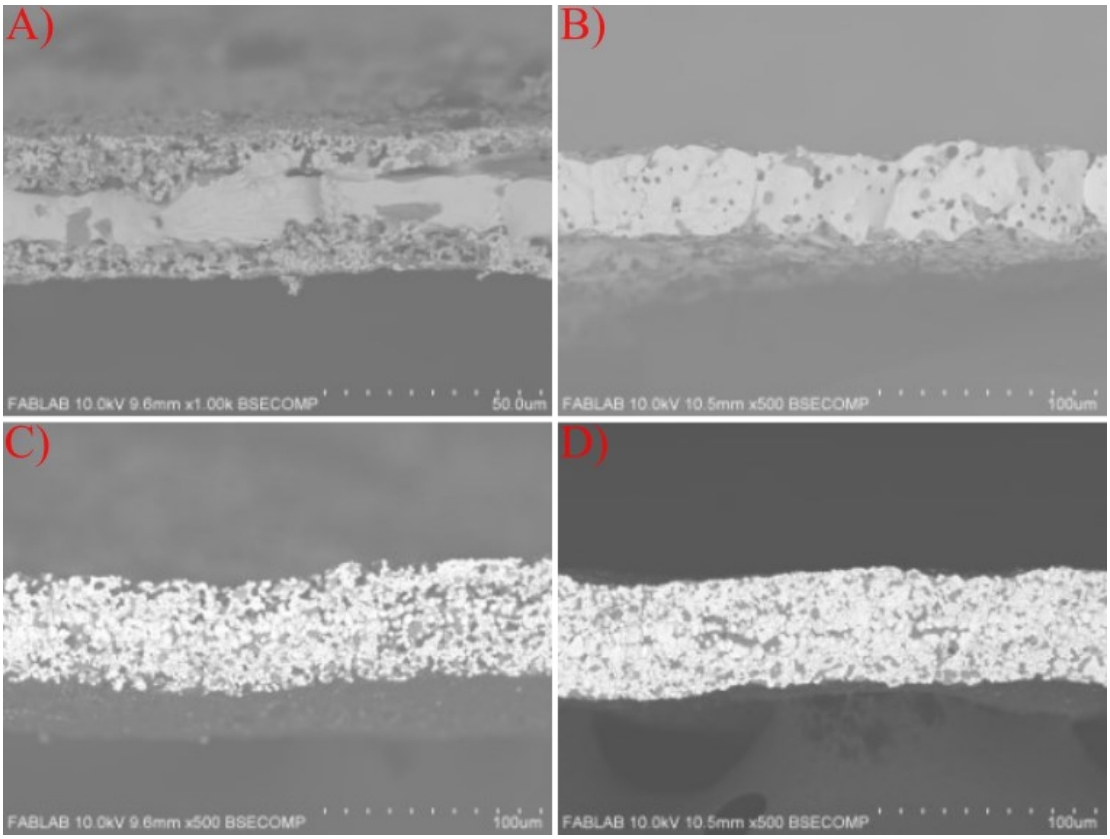

Figure 67.Trilayers incorporating LLZT dense layer and A) (2.9)LGLCZT(0.1)MIEC(Nb), B) (2.6)LGLZN(0.4)MIEC(Nb), C) (1.5)LLZT(1.5)MIEC(Nb), and D) (1)LLZT(2)MIEC(Nb) sintered at 1100 ℃ for 2 hours under argon flow.

Similar testing was conducted for LLZT-A dense layer, though curtailed to just $Pr_{1.5}$ and Pr_2 porous layers to limit variables. The microstructure for LLZT-A and $Pr_{1.5}$ trilayer, shown in Figure 68A, retained some porosity after sintering. Furthermore, it displayed a high degree of density in the dense layer and intragranular fracture. However, spot EDS scans across the surface indicate a high level of praseodymium and niobium cross-diffusion into the dense layer and a minimal gradient of praseodymium concentration from the exterior to the dense layer. EDS scans from the Pr_2 trilayer, in

Figure 68B, saw similar cross-diffusion, as both dense layers had approximately 93% of the praseodymium concentration on the lanthanoid site as the exterior of the trilayer. Though less intergranular fracture was observed for Pr_2 than $Pr_{1.5}$, it underwent even further porosity collapse.

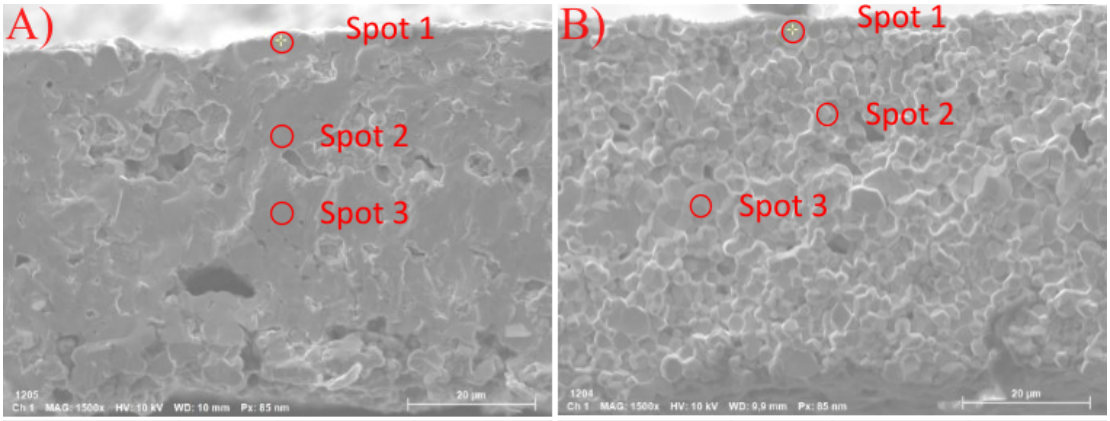

	Spot 1	Spot 2	Spot 3
Lanthanum	11(1)	11(1)	13(1)
Praseodynium	9(2)	8(1)	10(1)
Zirconium	12.0(9)	12.0(9)	15.0(9)
Niobium	1.0(3)	1.1(3)	1.1(3)
Tantallum	0.6(2)	0.6(2)	0.8(2)
Pr/(La+Pr)	0.45	0.42	0.43

	Spot 1	Spot 2	Spot 3
Lanthanum	7(1)	14(1)	14(1)
Praseodynium	10(2)	20(2)	17(2)
Zirconium	11.3(9)	26(1)	19(1)
Niobium	1.0(3)	2.3(4)	1.9(4)
Tantallum	0.6(2)	1.2(4)	0.8(3)
Pr/(La+Pr)	0.59	0.59	0.55

Figure 68. Trilayers of LLZT-A dense composition sintered at 1100 ℃ for 2 hours under argon flow with mixed LLZT-MIEC porous layers at ratios of A) 1:2 and B) 1:1.

To help bridge the gap between MIEC and traditional garnet dense compositions, LLZN was tested as well as the previously discussed LLZT and LLZT-A. Trilayer MIEC(Ce)-LLZN-MIEC(Ce) garnet sintered at 1050 ℃ for two hours resulted in high density dense layer while retaining good porosity in the MIEC layer. Trilayer was flat with only small amounts of bright secondary phase in the dense layer. EDS unfortunately displayed significant praseodymium diffusion into the dense layer at approximately a content of Pr_2 on the lanthanoid site. Niobium was noted to diffuse into the dense layer, but detection of Cerium was less visible.

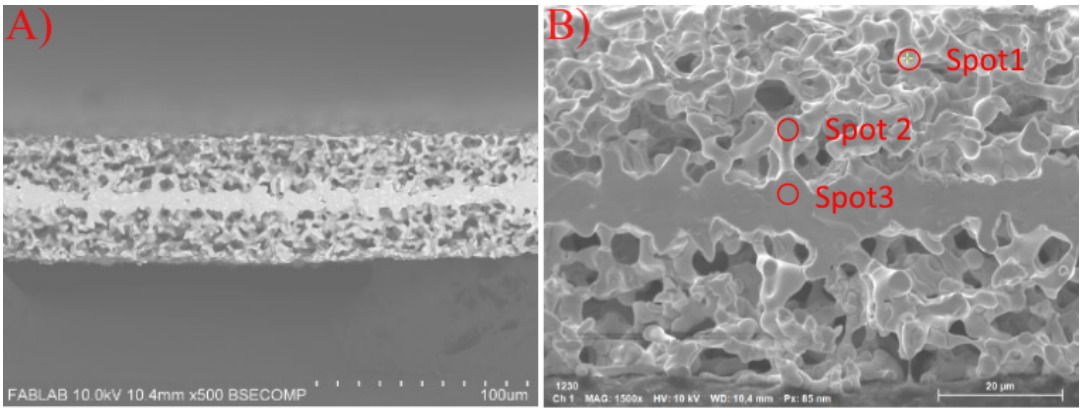

atomic %	Spot 1	Spot 2	Spot 3
Lanthanum	4.8(8)	4.2(9)	4.8(9)
Praseodymium	30(3)	11(2)	9(2)
Zirconium	6.0(4)	9.1(8)	8.9(8)
Niobium	x	0.6(2)	0.7(2)
Cerium	4.6(7)	x	x
Pr/(La+Pr)	0.86	0.72	0.65

Figure 69.A) backscatter and B) SEM of Ce-LGPZ/LLZN/Ce-LGPZ trilayers with EDS of indicated spots, sintered at 1050 C for 2 hours in air.

Praseodymium content lowered in MIEC layer using interlayer tapes. Retained good density and porosity, with some decrease in density with praseodymium content. Lower MIEC(Nb) content in the interlayer displayed lower concentration in dense layer as expected with Pr_2 and $Pr_{1.5}$ porous layers resulting in final praseodymium content in the dense layers of approximately $Pr_{1.5}$ and Pr, respectively. Pr concentration relative to La from the outermost section to that in the dense layer reduced by 25% in the above case down to 17% for $Pr_{1.5}$ initial porous layer.

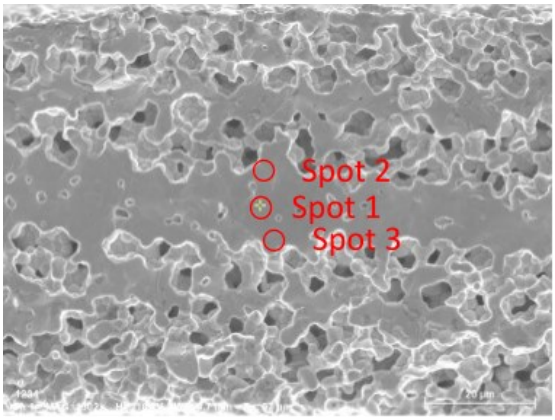

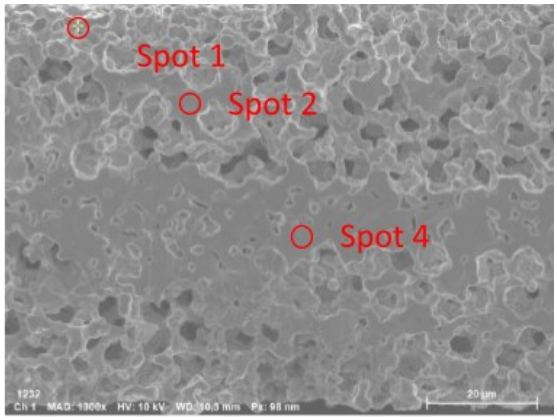

atomic %	Spot 1	Spot 2	Spot 3
Lanthanum	12(1)	14(1)	11(1)
Praseodynium	11(2)	14(2)	10(2)
Gallium	1.3(2)	1.6(2)	1.3(2)
Zirconium	12.7(8)	18(2)	11.1(8)
Niobium	1.9(3)	2.3(3)	1.4(2)
Tantallum	x	0.6(2)	0.3(2)
Pr/(La+Pr)	0.48	0.5	0.48

atomic %	spot1	spot 2	spot 4
Lanthanum	14(1)	15(2)	13(1)
Praseodynium	10(1)	10(1)	7(1)
Zirconium	14.5(9)	14.3(9)	12.0(8)
Niobium	1.5(3)	1.9(3)	1.5(3)
Tantallum	0.8(0.2)	0.8(2)	0.3(1)
Pr/(La+Pr)	0.42	0.4	0.35

Figure 70.SEM and EDS for LLZN-LLZT/MIEC(Nb) trilayers with LLZT/MIEC ratios of A) 1:2 and B) 1:1.

Incorporating even lower Pr content interlayer, Pr0.1, with full MIEC porous layers of both MIEC(Ce) and MIEC(Nb) had similar results. Good density was retained in the dense layer, with the trilayer incorporating MIEC(CE) having more preferable microstructure as the grains are more fused together. Final Pr content in the dense layer of both samples was significantly reduced to less than 25% of the lanthanoid site in garnet, approximating at $Pr_{0.65}$.

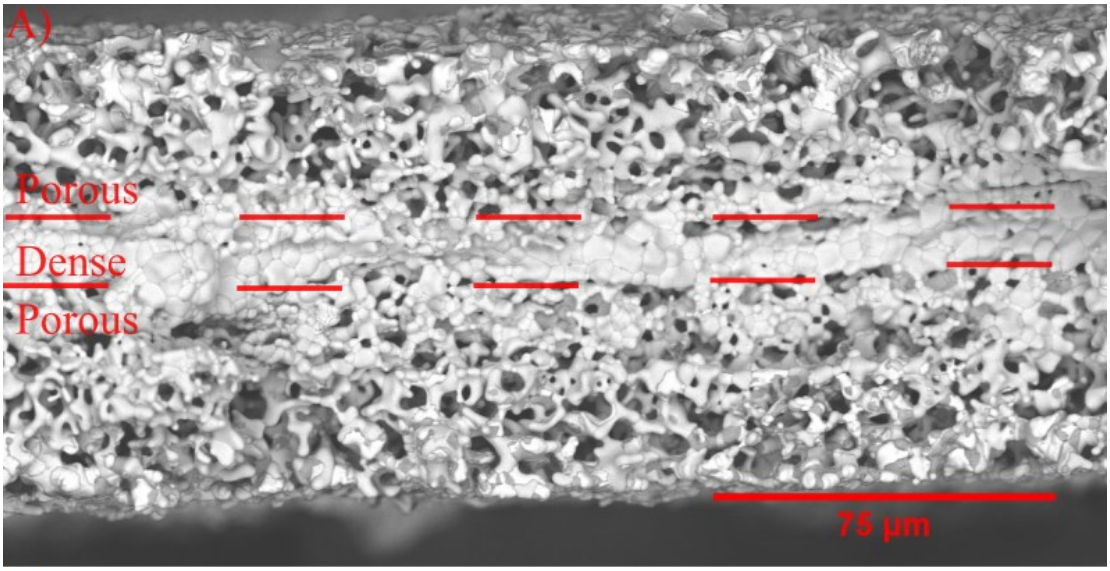

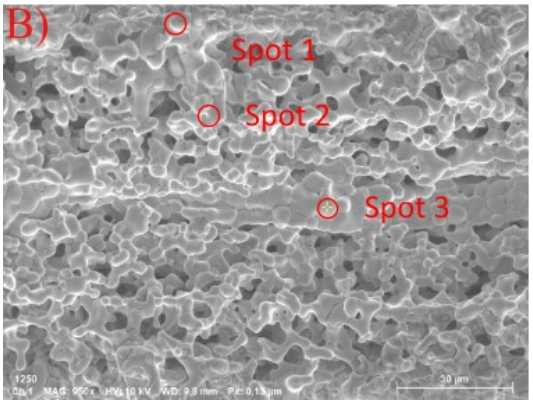

atomic %	Spot 1	Spot 2	Spot 3
Lanthanum	4.0(8)	9(1)	13(2)
Praseodymium	13(2)	16(2)	4(1)
Gallium	1.7(3)	1.4(2)	1.5(2)
Zirconium	10.8(9)	19(1)	11(1)
Niobium	0.5(2)	1.2(3)	1.0(2)
Tantalum	0.2(2)	0.6(3)	0.3(2)
Pr/(Pr+La)	0.765	0.64	0.235

Figure 71.A) Back-scatter and B) SEM and EDS analysis for trilayer LLZN-LGLCZT/Ce_LGPZ

DC polarization was performed on trilayers utilizing the basic structure from Figure 71 using either ceria or niobium doped MIEC, as shown in Figure 72, and compared with the thin LLZT layer discussed in previous chapters. Both trilayer compositions tested displayed electronic conductivity through the structure almost, but not quite, as low as the thin LLZT. The low observed through structure electronic

conductivity shows that the interlayer reduced praseodymium diffusion sufficiently for use as solid electrolyte.

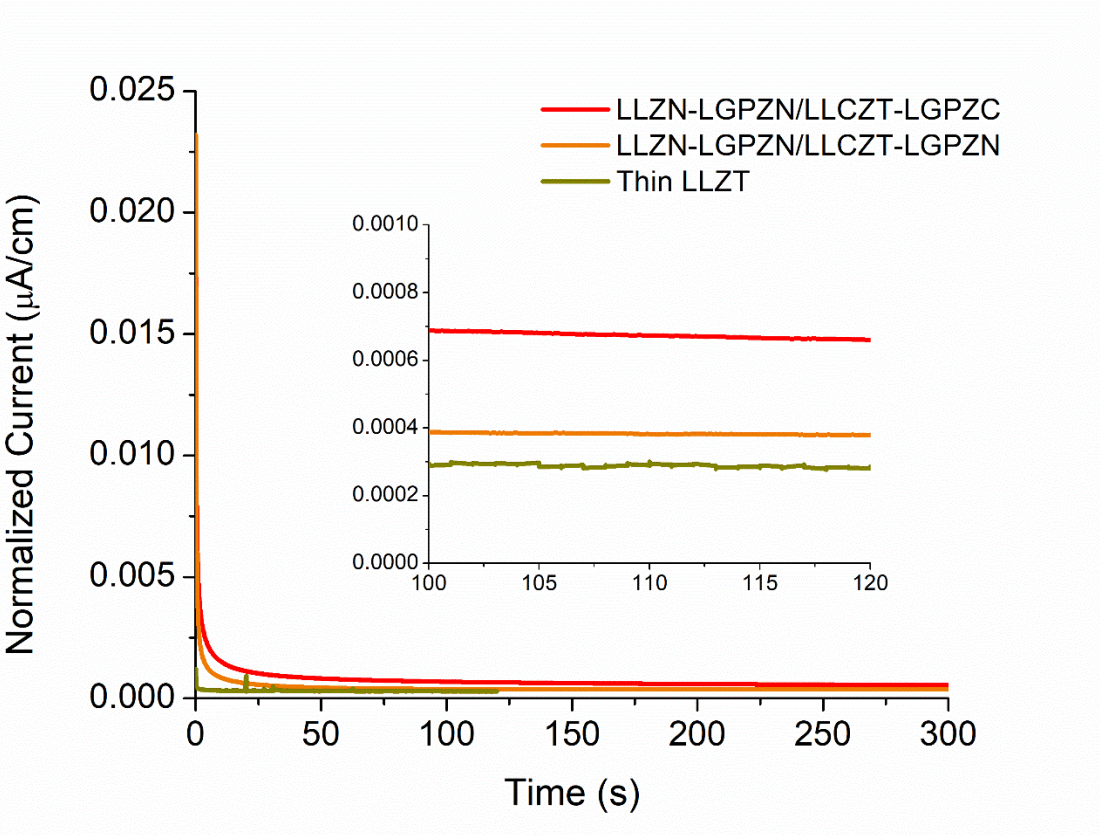

Figure 72. DC polarization comparing the trilayer structures synthesized via reactive phase sintering to the thin dense LLZT from previous chapters.

7.4.2.3 Increase MIEC sintering temperature

In tandem with the interlayer work, increasing MIEC sintering temperature to better match LLZT were made. Work elsewhere had indicated samarium dopant on the lanthanum site may increase sintering temperature, and was thus chosen, at 5 site percent, to test. Trilayers with dense layer composition of LLZT and LLZT-A were sintered with MIEC(Nb) and MIEC(SmNb) at 1100 °C to observe if similar microstructural change would occur. Cross-sectional SEM of the MIEC(Nb) with

LLZT and LLZT-A display, in Figure 73A and C respectively, complete pore collapse in both structures. Both structures display secondary phases in backscatter, though the aluminum doped structure showing more significant intra-granular fracture. As shown in Figure 73B and D, the samarium doping into the MIEC layer did not prevent the total collapse of the porous layer at the temperature required to sinter LLZT, though it did appear to weaken bonding between grains as seen through the lessened intra-granular fracture pattern.

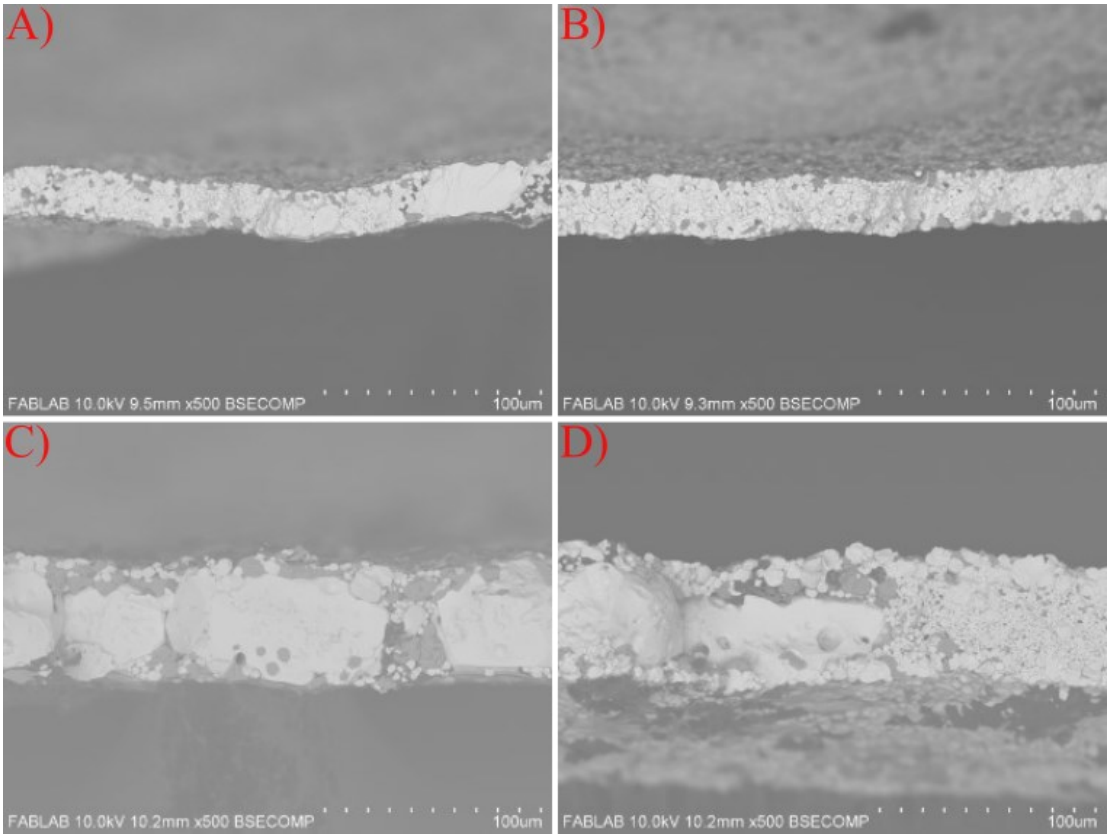

Figure 73.Cross-sectional SEM for LLZT dense-layer with A) niobium doped MIEC and B) samarium and niobium co-doped MIEC and LLZT-Al dense layer with C) niobium doped MIEC and D) samarium and niobium co-doped MIEC.

Chapter 8: Conclusions and Future Works

8.1 Conclusions

The work performed in this dissertation achieves the goals of both increasing rate-capability, improving garnet interfacing with liquid electrolyte, and introduces a novel approach to creating extremely thin free-standing garnet. The tests shown here prove that garnet-based battery systems can operate at high current density even with significant cathode loadings.

The initial study was to study interfaces within garnet-based quasi-solid-state batteries to determine the main sources of resistance with a focus on high temperature applications. Through testing cells of varied cathode loading and a series of impedance tests, IL-garnet interface was found to be the rate-determining factor in cell performance. Furthermore, secondary phase and low uniformity of grain structure were revealed as likely sources of cell failure. Modification of this interface through the addition of a new thin layer during lamination was shown to make this interface far more uniform and minimize the amount of secondary phase present. EIS-DRT testing of bilayers utilizing this interlayer revealed much improved elevated temperature capabilities but indicated a potential continued wetting issue between garnet and IL. Full cell utilizing this interlayer resulted in significant improvements in capacity, stability, and rate performance.

The second study then looked to understand the relationship between bonding within the catholyte of these systems and the interfacial resistance. A series of additives and lithium concentrations were tested in symmetric cells with LFP cathodes and dense garnet, which revealed lower IL-garnet interfacial resistance with higher lithium

concentration and higher resistance with ACN or TEP additives. Raman spectroscopy of these catholytes revealed a correlation between these resistances and the appearance of Li^+-$TFSI^-$ bonding, which was suppressed with co-solvent addition. This conclusion led to the use of fluoro-ether dilutants in the catholyte for room temperature and slightly elevated temperature use with NMC622 cathode. Near full practical capacity was achieved for both fluoro-ethers tested in full cells at room temperature, with TTFE achieving slightly higher capacity than OFPTFE. The cell with OFPTFE was much more stable cycling at slightly elevated temperatures as well as greater stability at higher cycling rates.

The third study looked to further minimize resistance from the garnet itself without introducing significantly more complications to processing. Extremely thin stand-alone dense garnet was successfully synthesized via bulk methods without the need to calcine garnet. Lithium symmetric cells reached the fastest rate reported for planar garnet or 75 mA/cm^2 before shorting and after nearly 2500 hours cycling. Lithium-NMC622 cells using thin garnet with Celgard interlayer and standard carbonate electrolyte achieved high capacity and reached 4 mA/cm^2 charging without shorting.

The fourth study created a flexible porous garnet to replace organic separators in traditional liquid electrolyte batteries to improve rate capability. Pure phase flexible garnet of high porosity was developed. MacMullen Number was much closer to ideal than Celgard separator indicating less tortuous pore network and/or better wetting. Rate-testing was performed both as sintered and with LiPAA coating, with both reaching 8 mA/cm2 without shorting and retaining xx and yy mAh/g respectively.

LiPAA greatly improved the discharge capacity reached and achieved 12 mA/cm^2 after an additional 200 cycles, mostly at 2 mA/cm^2.

8.2 Contributions

The work presented in this dissertation represents four first-author manuscripts currently in preparation for submission. My research has further contributed to 9 published manuscripts with more in preparation. This research has been funded by the Department of Energy's Advanced Research Projects Agency – Energy (ARPA-E), the Center for Research on Extreme Batteries (CREB), and Lockheed Martin.

Through the first two sections of this work, two different approaches were taken to improve garnet-ionic liquid catholyte system to improve rate capability and capacity. By minimizing secondary phases and creating more uniform microstructure across the interface, garnet was able to operate at 0.5 mA/cm^2 and to higher voltage without inducing instability in cycling while improving capacity. Addition of TEP to the catholyte resulted similarly improved cycling results, largely due to improved catholyte conductivity, while helping to show the interrelation between Li-TFSI bonding in the catholyte with interfacial resistance with garnet. Furthermore, this insight was leveraged to achieve 170 and 157 mAh/g using TTFTFE and OFPTFE dilutants at room temperature. OFPTFE-dilutant additionally displayed stability at elevated temperature (45°C) while reaching 160 and 87 mAh/g at 0.1 and 0.4 mA/cm^2.

The third section displayed that by combining tape-casting with reactionary phase sintering, it is possible to further reduce the thickness of free-standing garnet and thereby decrease cell resistance. Stand-alone garnet thicknesses of around 5 μm were

achieved, thinner than any other lithium garnet reported in literature. In addition to reducing the mass of garnet used, diffusion length of lithium was greatly reduced, and extremely high rates were achieved for lithium symmetric (75 mA/cm^2) and lithium-NMC full cells (4 mA/cm^2) without shorting.

In the fourth section, a flexible highly porous garnet structure was developed to reduce resistance in more traditional liquid electrolyte systems from the separator region. By combining this structure with LiPAA, cell rates were pushed to 8 mA/cm^2 while reaching 60 mAh/g. An additional 200 cycles after this, most of which was at C-rate of C, the cell did not short even when pushed to 12 mA/cm^2.

8.3 Future Works

In this work, full cell cycling was achieved using sub 10 μm thick free-standing garnet multiple times, but only with a polymeric interlayer to avoid point contact that would compress upon vacuum sealing of the cells. This unfortunately contributes additional mass and volume to the cell. Optimization of thinner interlayer provides one possible path forward for further improving energy density. Furthermore this could again improve rate-capability further as the lithium ion would have shorter diffusion pathways.

Alternatively, greater mechanical support or alternative packaging could be developed to allow this thin layer to withstand the impact upon sealing. Finishing the development of bilayer or trilayer structures incorporating this thin layer would be one path to achieving mechanical support.

Deposition of the cathode directly onto the garnet surface as a film provides an alternative path. This could also help to circumvent thermal issues between the

materials, depending on deposition technique, as the full sintering temperature of garnet would not have to be reached to ensure contact. Given the reduction in garnet volume and mass, relatively little active material would be required to potentially achieve high energy densities.

Optimization of other catholyte systems interface with garnet would likely prove fruitful in improving cell performance. Common carbonate, ether, and even some ionic liquids based electrolytes have inherently higher conductivities than the $Pyr_{14}TFSI$ system. So long as some thermal stability can be sacrificed, overall rate performance can likely be improved significantly at room temperature. Furthermore, greater understanding of the speciation of the interphase formed and how it is affected by additives and salt concentration helps tailor catholyte selection.

The presence of lanthanum-rich secondary phases was shown to be deleterious to cell performance. In the additional works section, it was shown that the secondary phases present in sintered garnet structures were strongly affected by dopant selection. While small amounts of samarium dopant displayed promise in further reducing secondary phases present, it may be possible to fully eliminate these secondary phases with further optimization of dopant system or sintering environment.

Bibliography

[1] K. Momma and F. Izumi, "VESTA 3 for three-dimensional visualization of crystal, volumetric and morphology data," *J Appl Crystallogr*, vol. 44, no. 6, pp. 1272–1276, Dec. 2011, doi: 10.1107/S0021889811038970.

[2] US EPA, "Sources of Greenhouse Gas Emissions," 2020. Accessed: Mar. 14, 2021. [Online]. Available: https://www.epa.gov/ghgemissions/sources-greenhouse-gas-emissions

[3] "Electricity in the U.S. - U.S. Energy Information Administration (EIA)." Accessed: Mar. 15, 2021. [Online]. Available: https://www.eia.gov/energyexplained/electricity/electricity-in-the-us.php

[4] "• Global battery demand by application | Statista." Accessed: Mar. 14, 2021. [Online]. Available: https://www.statista.com/statistics/1103218/global-battery-demand-forecast/

[5] "Wearable Technology Market by Product, Application | COVID-19 Impact Analysis | MarketsandMarkets™." Accessed: Mar. 14, 2021. [Online]. Available: https://www.marketsandmarkets.com/Market-Reports/wearable-electronics-market-983.html

[6] "Wearable Technology Market to Grow by $ 35.48 bn During 2020-2024 | Industry Analysis, Market Trends, Market Growth, Opportunities and Forecast 2024 | Technavio | Business Wire." Accessed: Mar. 14, 2021. [Online]. Available: https://www.businesswire.com/news/home/20201119005982/en/Wearable-Technology-Market-to-Grow-by-35.48-bn-During-2020-2024-Industry-Analysis-Market-Trends-Market-Growth-Opportunities-and-Forecast-2024-Technavio

[7] "Wearable Technology Market Size | Industry Report, 2020-2027." Accessed: Mar. 14, 2021. [Online]. Available: https://www.grandviewresearch.com/industry-analysis/wearable-technology-market

[8] M. Yacoub Al Shdaifat, R. Zulkifli, K. Sopian, and A. Adel Salih, "Basics, properties, and thermal issues of EV battery and battery thermal management systems: Comprehensive review," *Proceedings of the Institution of Mechanical Engineers, Part D: Journal of Automobile Engineering*, vol. 237, no. 2–3. SAGE Publications Ltd, pp. 295–311, Feb. 01, 2023. doi: 10.1177/09544070221079195.

[9] J. Hong, D. H. Seo, S. W. Kim, H. Gwon, S. T. Oh, and K. Kang, "Structural evolution of layered Li1.2Ni0.2Mn 0.6O2 upon electrochemical cycling in a Li rechargeable battery," *J Mater Chem*, vol. 20, no. 45, pp. 10179–10186, Dec. 2010, doi: 10.1039/c0jm01971b.

[10] A. R. Armstrong *et al.*, "Demonstrating Oxygen Loss and Associated Structural Reorganization in the Lithium Battery Cathode Li[Ni 0.2 Li 0.2 Mn 0.6]O 2," 2006, doi: 10.1021/ja062027.

[11] J. R. Croy, D. Kim, M. Balasubramanian, K. Gallagher, S.-H. Kang, and M. M. Thackeray, " Countering the Voltage Decay in High Capacity xLi 2 MnO 3 •(1–x)LiMO 2 Electrodes (M=Mn, Ni, Co) for Li + -Ion Batteries ," *J Electrochem Soc*, vol. 159, no. 6, pp. A781–A790, 2012, doi: 10.1149/2.080206jes.

[12] S. K. Jung *et al.*, "Understanding the degradation mechanisms of LiNi0.5Co 0.2Mn0.3O2 cathode material in lithium ion batteries," *Adv Energy Mater*, vol. 4, no. 1, Jan. 2014, doi: 10.1002/aenm.201300787.

[13] J. R. Croy, S. H. Kang, M. Balasubramanian, and M. M. Thackeray, "Li2MnO3-based composite cathodes for lithium batteries: A novel synthesis approach and new structures," *Electrochem commun*, vol. 13, no. 10, pp. 1063–1066, Oct. 2011, doi: 10.1016/j.elecom.2011.06.037.

[14] C. Tian, F. Lin, and M. M. Doeff, "Electrochemical Characteristics of Layered Transition Metal Oxide Cathode Materials for Lithium Ion Batteries: Surface, Bulk Behavior, and Thermal Properties," *Acc Chem Res*, vol. 51, no. 1, pp. 89–96, Jan. 2018, doi: 10.1021/acs.accounts.7b00520.

[15] T. M. Bandhauer, S. Garimella, and T. F. Fuller, "A Critical Review of Thermal Issues in Lithium-Ion Batteries," *J Electrochem Soc*, vol. 158, no. 3, p. R1, 2011, doi: 10.1149/1.3515880.

[16] S. Ohneseit *et al.*, "Thermal and Mechanical Safety Assessment of Type 21700 Lithium-Ion Batteries with NMC, NCA and LFP Cathodes–Investigation of Cell Abuse by Means of Accelerating Rate Calorimetry (ARC)," *Batteries*, vol. 9, no. 5, p. 237, Apr. 2023, doi: 10.3390/batteries9050237.

[17] D. W. McOwen, D. M. Seo, O. Borodin, J. Vatamanu, P. D. Boyle, and W. A. Henderson, "Concentrated electrolytes: Decrypting electrolyte properties and reassessing Al corrosion mechanisms," *Energy Environ Sci*, vol. 7, no. 1, pp. 416–426, Dec. 2014, doi: 10.1039/c3ee42351d.

[18] K. Matsumoto, K. Inoue, K. Nakahara, R. Yuge, T. Noguchi, and K. Utsugi, "Suppression of aluminum corrosion by using high concentration LiTFSI electrolyte," *J Power Sources*, vol. 231, pp. 234–238, 2013, doi: 10.1016/j.jpowsour.2012.12.028.

[19] A. Abouimrane, J. Ding, and I. J. Davidson, "Liquid electrolyte based on lithium bis-fluorosulfonyl imide salt: Aluminum corrosion studies and lithium ion battery investigations," *J Power Sources*, vol. 189, no. 1, pp. 693–696, Apr. 2009, doi: 10.1016/j.jpowsour.2008.08.077.

[20] E. Ls and E. Er, "POWER Corrosion of aluminum at high voltages in non-aqueous electrolytes containing perfluoroalkylsulfonyl imides; new lithium salts for lithium-ion cells," 1997.

[21] J. Zhang, J. Zhao, L. Yue, Q. Wang, J. Chai, and Z. Liu, "Safety-Reinforced Poly (Propylene Carbonate) -Based All-Solid-State Polymer Electrolyte for Ambient-Temperature Solid Polymer Lithium Batteries," pp. 1–10, 2015, doi: 10.1002/aenm.201501082.

[22] X. Gao, G. Zhu, and Q. Qu, "To cite this article: Rosamaría Fong et al," 1990.

[23] K. Xu, "Nonaqueous liquid electrolytes for lithium-based rechargeable batteries," *Chem Rev*, vol. 104, no. 10, pp. 4303–4417, Oct. 2004, doi: 10.1021/cr030203g.

[24] S. Kumagai, M. Sasaki, and M. Koyanagi, “Rechargeable Li 1 + x Mn 2 O 4 / Carbon Cells with a New Electrolyte Composition: Potentiostatic Studies and Application to Practical Cells You may also like LaserInduced Fluorescence Measurement of Metastable Chlorine Ion Temperature in TimeModulated Inductively Coupled Plasma,” 1993.
[25] D. Pavlov *et al.*, “To cite this article: Doron Aurbach et al,” 1995.
[26] Y. Eineli, S. R. Thomas, V. Koch, D. Aurbach, B. Markovsky, and A. Schechter, “Ethylmethylcarbonate, a Promising Solvent for Li-Ion Rechargeable Batteries.”
[27] H. Song *et al.*, “Hierarchically Porous, Ultrathick, ‘Breathable’ Wood-Derived Cathode for Lithium-Oxygen Batteries,” *Adv Energy Mater*, vol. 8, no. 4, Feb. 2018, doi: 10.1002/aenm.201701203.
[28] J. Dai *et al.*, “Flexible Solid-State Electrolyte with Aligned Nanostructures Derived from Wood,” *ACS Mater Lett*, vol. 1, no. 3, pp. 354–361, 2019, doi: 10.1021/acsmaterialslett.9b00189.
[29] Y. Zhang *et al.*, “High-capacity, low-tortuosity, and channel-guided lithium metal anode,” *Proc Natl Acad Sci U S A*, vol. 114, no. 14, pp. 3584–3589, 2017, doi: 10.1073/pnas.1618871114.
[30] R. Xu, J. Haung, Z. Tian, J. Xie, and C. Lei, “Effects of Coated Separator Surface Morphology on Electrolyte Interfacial Wettability and Corresponding Li-Ion Battery Performance,” *Polymers (Basel)*, vol. 12, no. 1, Jan. 2020, doi: 10.3390/polym12010117.
[31] H. Nakae’, R. Inup, Y. Hira’i’a’, and H. Saito, “EFFECTS OF SURFACE ROUNDNESS ON WETTABILITY,” 1998.
[32] J. Landesfeind, J. Hattendorff, A. Ehrl, W. A. Wall, and H. A. Gasteiger, “Tortuosity Determination of Battery Electrodes and Separators by Impedance Spectroscopy,” *J Electrochem Soc*, vol. 163, no. 7, pp. A1373–A1387, 2016, doi: 10.1149/2.1141607jes.
[33] J. Kalhoff, G. G. Eshetu, D. Bresser, and S. Passerini, “Safer electrolytes for lithium-ion batteries: State of the art and perspectives,” *ChemSusChem*, vol. 8, no. 13, pp. 2154–2175, 2015, doi: 10.1002/cssc.201500284.
[34] S. Chen, Z. Wang, H. Zhao, H. Qiao, H. Luan, and L. Chen, “A novel flame retardant and film-forming electrolyte additive for lithium ion batteries,” *J Power Sources*, vol. 187, no. 1, pp. 229–232, Feb. 2009, doi: 10.1016/j.jpowsour.2008.10.091.
[35] D. J. Lee *et al.*, “Phosphorus derivatives as electrolyte additives for lithium-ion battery: The removal of O2 generated from lithium-rich layered oxide cathode,” *J Power Sources*, vol. 243, pp. 831–835, 2013, doi: 10.1016/j.jpowsour.2013.06.091.
[36] S. Stramare, V. Thangadurai, and W. Weppner, “Lithium Lanthanum Titanates: A Review,” 2003, doi: 10.1021/cm0300516.
[37] E. Krämer *et al.*, “Mechanism of Anodic Dissolution of the Aluminum Current Collector in 1 M LiTFSI EC:DEC 3:7 in Rechargeable Lithium Batteries,” *J Electrochem Soc*, vol. 160, no. 2, pp. A356–A360, 2013, doi: 10.1149/2.081302jes.

[38] M. Morita, T. Shibata, N. Yoshimoto, and M. Ishikawa, “Anodic behavior of aluminum current collector in LiTFSI solutions with different solvent compositions,” in *Journal of Power Sources*, Jun. 2003, pp. 784–788. doi: 10.1016/S0378-7753(03)00253-2.

[39] P. C. Shi *et al.*, “Effect of propylene carbonate-Li+ solvation structures on graphite exfoliation and its application in Li-ion batteries,” *Electrochim Acta*, vol. 247, pp. 12–18, Sep. 2017, doi: 10.1016/j.electacta.2017.06.174.

[40] Y. Shen *et al.*, “Water-in-salt electrolyte for safe and high-energy aqueous battery,” *Energy Storage Materials*, vol. 34. Elsevier B.V., pp. 461–474, Jan. 01, 2021. doi: 10.1016/j.ensm.2020.10.011.

[41] L. Suo *et al.*, “‘Water-in-salt’ electrolyte enables high-voltage aqueous lithium-ion chemistries.” [Online]. Available: https://www.science.org

[42] R. Petibon, C. P. Aiken, L. Ma, D. Xiong, and J. R. Dahn, “The use of ethyl acetate as a sole solvent in highly concentrated electrolyte for Li-ion batteries,” *Electrochim Acta*, vol. 154, pp. 287–293, 2015, doi: 10.1016/j.electacta.2014.12.093.

[43] Y. Yamada *et al.*, “Unusual stability of acetonitrile-based superconcentrated electrolytes for fast-charging lithium-ion batteries,” *J Am Chem Soc*, vol. 136, no. 13, pp. 5039–5046, 2014, doi: 10.1021/ja412807w.

[44] T. Tamura *et al.*, “Physicochemical properties of glyme-Li salt complexes as a new family of room-temperature ionic liquids,” *Chem Lett*, vol. 39, no. 7, pp. 753–755, 2010, doi: 10.1246/cl.2010.753.

[45] H. Moon *et al.*, “Solvent activity in electrolyte solutions controls electrochemical reactions in Li-Ion and Li-Sulfur batteries,” *Journal of Physical Chemistry C*, vol. 119, no. 8, pp. 3957–3970, Feb. 2015, doi: 10.1021/jp5128578.

[46] K. Ueno *et al.*, “Li+ Solvation and Ionic Transport in Lithium Solvate Ionic Liquids Diluted by Molecular Solvents,” *Journal of Physical Chemistry C*, vol. 120, no. 29, pp. 15792–15802, Jul. 2016, doi: 10.1021/acs.jpcc.5b11642.

[47] K. Dokko *et al.*, “Solvate Ionic Liquid Electrolyte for Li–S Batteries,” *J Electrochem Soc*, vol. 160, no. 8, pp. A1304–A1310, 2013, doi: 10.1149/2.111308jes.

[48] K. Ueno, J. Murai, H. Moon, K. Dokko, and M. Watanabe, “A Design Approach to Lithium-Ion Battery Electrolyte Based on Diluted Solvate Ionic Liquids,” *J Electrochem Soc*, vol. 164, no. 1, pp. A6088–A6094, 2017, doi: 10.1149/2.0121701jes.

[49] W. Dai *et al.*, “Localized concentrated high-concentration electrolyte enhanced stability and safety for high voltage Li-ion batteries,” *Electrochim Acta*, vol. 320, p. 134633, Oct. 2019, doi: 10.1016/j.electacta.2019.134633.

[50] S. Perez Beltran, X. Cao, J. G. Zhang, and P. B. Balbuena, “Localized High Concentration Electrolytes for High Voltage Lithium-Metal Batteries: Correlation between the Electrolyte Composition and Its Reductive/Oxidative Stability,” *Chemistry of Materials*, vol. 32, no. 14, pp. 5973–5984, Jul. 2020, doi: 10.1021/acs.chemmater.0c00987.

[51] M. J. Wang, J. B. Wolfenstine, and J. Sakamoto, “Mixed Electronic and Ionic Conduction Properties of Lithium Lanthanum Titanate,” *Adv Funct Mater*, vol. 30, no. 10, Mar. 2020, doi: 10.1002/adfm.201909140.
[52] Y. Mo, “First principles study on electrochemical and chemical stability of solid electrolyte–electrode interfaces in all-solid-state Li-ion batteries,” vol. 4, no. 9, 2016, doi: 10.1039/C5TA08574H.
[53] S. Ohta, T. Kobayashi, and T. Asaoka, “High lithium ionic conductivity in the garnet-type oxide Li7-X La3(Zr2-X, NbX)O12 (X = 0-2),” *J Power Sources*, vol. 196, no. 6, pp. 3342–3345, Mar. 2011, doi: 10.1016/j.jpowsour.2010.11.089.
[54] C. A. Geiger *et al.*, “Crystal chemistry and stability of ‘Li7La 3Zr2O12’ garnet: A fast lithium-ion conductor,” *Inorg Chem*, vol. 50, no. 3, pp. 1089–1097, Feb. 2011, doi: 10.1021/ic101914e.
[55] Y. Shimonishi *et al.*, “Synthesis of garnet-type Li7 - XLa3Zr 2O12 - 1/2x and its stability in aqueous solutions,” *Solid State Ion*, vol. 183, no. 1, pp. 48–53, 2011, doi: 10.1016/j.ssi.2010.12.010.
[56] E. A. Dobretsov, Y. G. Mateyshina, and N. F. Uvarov, “Influence of lithium oxide excess and alumina on grain boundary resistance of Li6.75La3Zr1.75Nb0.25O12 solid electrolyte,” *Solid State Ion*, vol. 299, pp. 55–59, Jan. 2017, doi: 10.1016/j.ssi.2016.09.014.
[57] E. Rangasamy, J. Wolfenstine, J. Allen, and J. Sakamoto, “The effect of 24c-site (A) cation substitution on the tetragonal-cubic phase transition in Li7-xLa3-xAxZr 2O12 garnet-based ceramic electrolyte,” *J Power Sources*, vol. 230, pp. 261–266, May 2013, doi: 10.1016/j.jpowsour.2012.12.076.
[58] S. Vema, A. H. Berge, S. Nagendran, and C. P. Grey, “Clarifying the Dopant Local Structure and Effect on Ionic Conductivity in Garnet Solid-State Electrolytes for Lithium-Ion Batteries,” *Chemistry of Materials*, vol. 35, no. 22, pp. 9632–9646, Nov. 2023, doi: 10.1021/acs.chemmater.3c01831.
[59] X. Huang, Y. Lu, Z. Song, T. Xiu, M. E. Badding, and Z. Wen, “Preparation of dense Ta-LLZO/MgO composite Li-ion solid electrolyte: Sintering, microstructure, performance and the role of MgO,” *Journal of Energy Chemistry*, vol. 39, pp. 8–16, Dec. 2019, doi: 10.1016/j.jechem.2019.01.013.
[60] J. Sastre *et al.*, “Aluminum-Assisted Densification of Cosputtered Lithium Garnet Electrolyte Films for Solid-State Batteries,” *ACS Appl Energy Mater*, vol. 2, no. 12, pp. 8511–8524, Dec. 2019, doi: 10.1021/acsaem.9b01387.
[61] Y. Zhu *et al.*, “Dopant-Dependent Stability of Garnet Solid Electrolyte Interfaces with Lithium Metal,” vol. 1803440, pp. 1–11, 2019, doi: 10.1002/aenm.201803440.
[62] Y. Luo, Q. Zhang, A. Shen, M. Shen, D. Xie, and Y. Yan, “Calcium-doping effects on structure and electric performances of garnet-type Li6.6La3Zr1.6Sb0.4O12 solid-state electrolytes,” *Solid State Ion*, vol. 374, Jan. 2022, doi: 10.1016/j.ssi.2021.115812.
[63] T. Zhang, T. D. Christopher, S. Huang, T. Söhnel, Y. Liu, and P. Cao, “Electrochemical properties of Li6+yLa3−yBayNbZrO12 lithium garnet oxide solid-state electrolytes with co-doping barium and zirconium,” *J Alloys Compd*, vol. 862, May 2021, doi: 10.1016/j.jallcom.2021.158600.

[64] R. Murugan, V. Thangadurai, and W. Weppner, “Lithium ion conductivity of Li5+x Ba x La 3-x Ta2O12 (x∈=∈0-2) with garnet-related structure in dependence of the barium content,” *Ionics (Kiel)*, vol. 13, no. 4, pp. 195–203, Aug. 2007, doi: 10.1007/s11581-007-0097-8.
[65] G. V. Alexander, C. Shi, J. O’Neill, and E. D. Wachsman, “Extreme lithium-metal cycling enabled by a mixed ion- and electron-conducting garnet three-dimensional architecture,” *Nat Mater*, vol. 22, no. 9, pp. 1136–1143, Sep. 2023, doi: 10.1038/s41563-023-01627-9.
[66] K. Hofstetter, A. J. Samson, S. Narayanan, and V. Thangadurai, “Present understanding of the stability of Li-stuffed garnets with moisture, carbon dioxide, and metallic lithium,” *J Power Sources*, vol. 390, no. February, pp. 297–312, 2018, doi: 10.1016/j.jpowsour.2018.04.016.
[67] J. G. Connell *et al.*, “Kinetic versus Thermodynamic Stability of LLZO in Contact with Lithium Metal,” *Chemistry of Materials*, vol. 32, no. 23, pp. 10207–10215, 2020, doi: 10.1021/acs.chemmater.0c03869.
[68] K. Hofstetter *et al.*, “Electrochemical Stability of Garnet-Type Electrochemical Stability of Garnet-Type Deposited-Al 2 O 3 under CO 2 and Humidity,” 2019, doi: 10.1149/2.0201910jes.
[69] A. Sharafi *et al.*, “Impact of air exposure and surface chemistry on Li-Li7La3Zr2O12 interfacial resistance,” *J Mater Chem A Mater*, vol. 5, no. 26, pp. 13475–13487, 2017, doi: 10.1039/c7ta03162a.
[70] S. Sen Chi, Y. Liu, N. Zhao, X. Guo, C. W. Nan, and L. Z. Fan, “Solid polymer electrolyte soft interface layer with 3D lithium anode for all-solid-state lithium batteries,” *Energy Storage Mater*, vol. 17, no. July 2018, pp. 309–316, 2019, doi: 10.1016/j.ensm.2018.07.004.
[71] S. A. Pervez *et al.*, “Overcoming the Interfacial Limitations Imposed by the Solid – Solid Interface in Solid-State Batteries Using Ionic Liquid-Based Interlayers,” 2020, doi: 10.1002/smll.202000279.
[72] A. Sharafi *et al.*, “Surface Chemistry Mechanism of Ultra-Low Interfacial Resistance in the Solid-State Electrolyte Li7La3Zr2O12,” *Chemistry of Materials*, vol. 29, no. 18, pp. 7961–7968, 2017, doi: 10.1021/acs.chemmater.7b03002.
[73] Y. Shao *et al.*, “Drawing a Soft Interface: An Effective Interfacial Modification Strategy for Garnet-Type Solid-State Li Batteries,” *ACS Energy Lett*, vol. 3, no. 6, pp. 1212–1218, 2018, doi: 10.1021/acsenergylett.8b00453.
[74] Y. Li *et al.*, “Garnet Electrolyte with an Ultralow Interfacial Resistance for Li-Metal Batteries,” *J Am Chem Soc*, vol. 140, no. 20, pp. 6448–6455, 2018, doi: 10.1021/jacs.8b03106.
[75] H. Huo *et al.*, “In-situ formed Li2CO3-free garnet/Li interface by rapid acid treatment for dendrite-free solid-state batteries,” *Nano Energy*, vol. 61, no. January, pp. 119–125, 2019, doi: 10.1016/j.nanoen.2019.04.058.
[76] M. M. Besli *et al.*, “Effect of Liquid Electrolyte Soaking on the Interfacial Resistance of Li7La3Zr2O12 for All-Solid-State Lithium Batteries,” *ACS Appl Mater Interfaces*, vol. 12, no. 18, pp. 20605–20612, 2020, doi: 10.1021/acsami.0c06194.

[77] X. Han *et al.*, “Negating interfacial impedance in garnet-based solid-state Li metal batteries,” *Nat Mater*, vol. 16, no. 5, pp. 572–579, May 2017, doi: 10.1038/nmat4821.
[78] B. Liu *et al.*, “3D lithium metal anodes hosted in asymmetric garnet frameworks toward high energy density batteries,” *Energy Storage Mater*, vol. 14, no. January, pp. 376–382, 2018, doi: 10.1016/j.ensm.2018.04.015.
[79] G. T. Hitz *et al.*, “High-rate lithium cycling in a scalable trilayer Li-garnet-electrolyte architecture,” *Materials Today*, vol. 22, no. February, pp. 50–57, 2019, doi: 10.1016/j.mattod.2018.04.004.
[80] E. Yi *et al.*, “All-Solid-State Batteries Using Rationally Designed Garnet Electrolyte Frameworks,” *ACS Appl Energy Mater*, vol. 3, no. 1, pp. 170–175, 2020, doi: 10.1021/acsaem.9b02101.
[81] C. Yang *et al.*, “Continuous plating/stripping behavior of solid-state lithium metal anode in a 3D ion-conductive framework,” *Proc Natl Acad Sci U S A*, vol. 115, no. 15, pp. 3770–3775, Apr. 2018, doi: 10.1073/pnas.1719758115.
[82] H. Zhang *et al.*, “Bilayer Dense-Porous Li7La3Zr2O12 Membranes for High-Performance Li-Garnet Solid-State Batteries,” *Advanced Science*, vol. 10, no. 8, Mar. 2023, doi: 10.1002/advs.202205821.
[83] L. Buannic, M. Naviroj, S. M. Miller, J. Zagorski, K. T. Faber, and A. Llordés, “Dense freeze-cast Li7La3Zr2O12 solid electrolytes with oriented open porosity and contiguous ceramic scaffold,” *Journal of the American Ceramic Society*, vol. 102, no. 3, pp. 1021–1029, Mar. 2019, doi: 10.1111/jace.15938.
[84] H. Shen *et al.*, “Oriented porous LLZO 3D structures obtained by freeze casting for battery applications,” *J Mater Chem A Mater*, vol. 7, no. 36, pp. 20861–20870, 2019, doi: 10.1039/c9ta06520b.
[85] J. Reinacher, S. Berendts, and J. Janek, “Preparation and electrical properties of garnet-type Li 6BaLa2Ta2O12 lithium solid electrolyte thin films prepared by pulsed laser deposition,” *Solid State Ion*, vol. 258, pp. 1–7, May 2014, doi: 10.1016/j.ssi.2014.01.046.
[86] J. Nong, H. Xu, Z. Yu, G. Zhu, and A. Yu, “Properties and preparation of Li-La-Ti-Zr-O thin film electrolyte,” *Mater Lett*, vol. 154, pp. 167–169, Sep. 2015, doi: 10.1016/j.matlet.2015.04.088.
[87] R. Pfenninger, M. Struzik, I. Garbayo, E. Stilp, and J. L. M. Rupp, “A low ride on processing temperature for fast lithium conduction in garnet solid-state battery films,” *Nat Energy*, vol. 4, no. 6, pp. 475–483, Jun. 2019, doi: 10.1038/s41560-019-0384-4.
[88] M. Bitzer, T. Van Gestel, S. Uhlenbruck, and Hans-Peter-Buchkremer, “Sol-gel synthesis of thin solid Li7La3Zr2O12 electrolyte films for Li-ion batteries,” *Thin Solid Films*, vol. 615, pp. 128–134, Sep. 2016, doi: 10.1016/j.tsf.2016.07.010.
[89] C. Loho, R. Djenadic, M. Bruns, O. Clemens, and H. Hahn, “ Garnet-Type Li 7 La 3 Zr 2 O 12 Solid Electrolyte Thin Films Grown by CO 2 -Laser Assisted CVD for All-Solid-State Batteries ,” *J Electrochem Soc*, vol. 164, no. 1, pp. A6131–A6139, 2017, doi: 10.1149/2.0201701jes.

[90] E. Kazyak *et al.*, “Atomic Layer Deposition of the Solid Electrolyte Garnet Li7La3Zr2O12,” *Chemistry of Materials*, vol. 29, no. 8, pp. 3785–3792, Apr. 2017, doi: 10.1021/acs.chemmater.7b00944.
[91] S. Hong *et al.*, “Structural and Chemical Compatibilities of Li1−xNi0.5Co0.2Mn0.3O2 Cathode Material with Garnet-Type Solid Electrolyte for All-Solid-State Batteries,” *Small*, vol. 17, no. 46, pp. 1–10, 2021, doi: 10.1002/smll.202103306.
[92] Y. Ren, T. Liu, Y. Shen, Y. Lin, and C. W. Nan, “Chemical compatibility between garnet-like solid state electrolyte Li6.75La3Zr1.75Ta0.25O12 and major commercial lithium battery cathode materials,” *Journal of Materiomics*, vol. 2, no. 3, pp. 256–264, Sep. 2016, doi: 10.1016/j.jmat.2016.04.003.
[93] J. Sastre, X. Chen, A. Aribia, A. N. Tiwari, and Y. E. Romanyuk, “Fast Charge Transfer across the Li7La3Zr2O12Solid Electrolyte/LiCoO2Cathode Interface Enabled by an Interphase-Engineered All-Thin-Film Architecture,” *ACS Appl Mater Interfaces*, vol. 12, no. 32, pp. 36196–36207, Aug. 2020, doi: 10.1021/acsami.0c09777.
[94] J. Sastre *et al.*, “Blocking lithium dendrite growth in solid-state batteries with an ultrathin amorphous Li-La-Zr-O solid electrolyte,” *Commun Mater*, vol. 2, no. 1, Dec. 2021, doi: 10.1038/s43246-021-00177-4.
[95] B. Xu, H. Duan, H. Liu, C. A. Wang, and S. Zhong, “Stabilization of Garnet/Liquid Electrolyte Interface Using Superbase Additives for Hybrid Li Batteries,” *ACS Appl Mater Interfaces*, vol. 9, no. 25, pp. 21077–21082, 2017, doi: 10.1021/acsami.7b05599.
[96] B. Liu *et al.*, “Garnet Solid Electrolyte Protected Li-Metal Batteries,” *ACS Appl Mater Interfaces*, vol. 9, no. 22, pp. 18809–18815, Jun. 2017, doi: 10.1021/acsami.7b03887.
[97] Y. Jin *et al.*, “High-Energy-Density Solid-Electrolyte-Based Liquid Li-S and Li-Se Batteries,” *Joule*, vol. 4, no. 1, pp. 262–274, Jan. 2020, doi: 10.1016/j.joule.2019.09.003.
[98] T. Abe *et al.*, “Lithium-Ion Transfer at the Interface Between Lithium-Ion Conductive Ceramic Electrolyte and Liquid Electrolyte-A Key to Enhancing the Rate Capability of Lithium-Ion Batteries Lithium-Ion Transfer at the Interface Between Lithium-Ion Conductive Ceramic El,” 2005, doi: 10.1149/1.2042907.
[99] M. Weiss *et al.*, “From Liquid - to Solid - State Batteries : Ion Transfer Kinetics of Heteroionic Interfaces,” *Electrochemical Energy Reviews*, no. 0123456789, 2020, doi: 10.1007/s41918-020-00062-7.
[100] Y. Yamada, F. Sagane, Y. Iriyama, T. Abe, and Z. Ogumi, “Kinetics of Lithium-Ion Transfer at the Interface between Li 0 . 35 La 0 . 55 TiO 3 and Binary Electrolytes,” pp. 14528–14532, 2009, doi: 10.1021/jp9043539.
[101] M. Schleutker, J. Bahner, C. L. Tsai, D. Stolten, and C. Korte, “On the interfacial charge transfer between solid and liquid Li+ electrolytes,” *Physical Chemistry Chemical Physics*, vol. 19, no. 39, pp. 26596–26605, 2017, doi: 10.1039/c7cp05213h.

[102] M. R. Busche *et al.*, "The Formation of the Solid/Liquid Electrolyte Interphase (SLEI) on NASICON-Type Glass Ceramics and LiPON," *Adv Mater Interfaces*, vol. 7, no. 19, pp. 1–14, 2020, doi: 10.1002/admi.202000380.
[103] J. Liu *et al.*, "The Interface between Li6.5La3Zr1.5Ta0.5O12 and Liquid Electrolyte," *Joule*, pp. 101–108, 2020, doi: 10.1016/j.joule.2019.10.001.
[104] M. R. Busche *et al.*, "Dynamic formation of a solid-liquid electrolyte interphase and its consequences for hybrid-battery concepts," *Nat Chem*, vol. 8, no. 5, pp. 426–434, May 2016, doi: 10.1038/nchem.2470.
[105] A. Lewandowski and A. Swiderska-Mokek, "Ionic Liquids as Electrolytes for Li-Ion Batteries-An Overview of Electrochemical Studies," *J Power Sources*, vol. 194, pp. 601–609, 2009, doi: 10.1016/j.jpowsour.2009.06.089.
[106] H. Zhang *et al.*, "Ionic liquid electrolyte with highly concentrated LiTFSI for lithium metal batteries," *Electrochim Acta*, vol. 285, pp. 78–85, 2018, doi: 10.1016/j.electacta.2018.07.231.
[107] T. Sato, T. Maruo, S. Marukane, and K. Takagi, "Ionic liquids containing carbonate solvent as electrolytes for lithium ion cells," *J Power Sources*, vol. 138, no. 1–2, pp. 253–261, 2004, doi: 10.1016/j.jpowsour.2004.06.027.
[108] M. Barghamadi *et al.*, "Effect of LiNO3 additive and pyrrolidinium ionic liquid on the solid electrolyte interphase in the lithium-sulfur battery," *J Power Sources*, vol. 295, pp. 212–220, Jul. 2015, doi: 10.1016/j.jpowsour.2015.06.150.
[109] Q. J. Meisner *et al.*, "Impact of Co-Solvent and LiTFSI Concentration on Ionic Liquid-Based Electrolytes for Li-S Battery Impact of Co-Solvent and LiTFSI Concentration on Ionic Liquid- Based Electrolytes for Li-S Battery," 2020, doi: 10.1149/1945-7111/ab76a3.
[110] N. Riphaus, B. Stiaszny, H. Beyer, S. Indris, H. A. Gasteiger, and S. J. Sedlmaier, "Understanding Chemical Stability Issues between Different Solid Electrolytes in All-Solid-State Batteries," *J Electrochem Soc*, vol. 166, no. 6, pp. A975–A983, 2019, doi: 10.1149/2.0351906jes.
[111] F. Soavi, C. Arbizzani, and M. Mastragostino, "Leakage currents and self-discharge of ionic liquid-based supercapacitors," *J Appl Electrochem*, vol. 44, no. 4, pp. 491–496, 2014, doi: 10.1007/s10800-013-0647-x.
[112] N. P. W. Pieczonka *et al.*, "Lithium Polyacrylate (LiPAA) as an Advanced Binder and a Passivating Agent for High-Voltage Li-Ion Batteries," *Adv Energy Mater*, vol. 5, no. 23, 2015, doi: 10.1002/aenm.201501008.
[113] E. Peled, M. Goor, I. Schektman, T. Mukra, Y. Shoval, and D. Golodnitsky, "The Effect of Binders on the Performance and Degradation of the Lithium/Sulfur Battery Assembled in the Discharged State," *J Electrochem Soc*, vol. 164, no. 1, pp. A5001–A5007, 2017, doi: 10.1149/2.0161701jes.
[114] C. Wang *et al.*, "Conformal, Nanoscale ZnO Surface Modification of Garnet-Based Solid-State Electrolyte for Lithium Metal Anodes," *Nano Lett*, vol. 17, no. 1, pp. 565–571, 2017, doi: 10.1021/acs.nanolett.6b04695.
[115] C. A. Schneider, W. S. Rasband, and K. W. Eliceiri, "NIH Image to ImageJ: 25 years of image analysis," *Nat Methods*, vol. 9, no. 7, pp. 671–675, 2012, doi: 10.1038/nmeth.2089.

[116] B. H. Toby and R. B. Von Dreele, "*GSAS-II* : the genesis of a modern open-source all purpose crystallography software package," *J Appl Crystallogr*, vol. 46, no. 2, pp. 544–549, Apr. 2013, doi: 10.1107/S0021889813003531.
[117] T. H. Wan, M. Saccoccio, C. Chen, and F. Ciucci, "Influence of the Discretization Methods on the Distribution of Relaxation Times Deconvolution: Implementing Radial Basis Functions with DRTtools," *Electrochim Acta*, vol. 184, pp. 483–499, 2015, doi: 10.1016/j.electacta.2015.09.097.
[118] Y. Fang, C. Chen, J. Fan, M. Zhang, W. Yuan, and L. Li, "Reversible interaction of 1-butyl-1-methylpyrrolidinium cations with 5,7,12,14-pentacenetetrone from a pure ionic liquid electrolyte for dual-ion batteries," *Chemical Communications*, vol. 55, no. 57, pp. 8333–8336, 2019, doi: 10.1039/c9cc04626g.
[119] B. Manikandan, V. Ramar, C. Yap, and P. Balaya, "Investigation of physico-chemical processes in lithium-ion batteries by deconvolution of electrochemical impedance spectra," *J Power Sources*, vol. 361, pp. 300–309, 2017, doi: 10.1016/j.jpowsour.2017.07.006.
[120] J. P. Schmidt, T. Chrobak, M. Ender, J. Illig, D. Klotz, and E. Ivers-Tiffée, "Studies on LiFePO4 as cathode material using impedance spectroscopy," *J Power Sources*, vol. 196, no. 12, pp. 5342–5348, 2011, doi: 10.1016/j.jpowsour.2010.09.121.
[121] M. R. Busche *et al.*, "Dynamic formation of a solid-liquid electrolyte interphase and its consequences for hybrid-battery concepts," *Nat Chem*, vol. 8, no. 5, pp. 426–434, 2016, doi: 10.1038/nchem.2470.
[122] C. Chen, J. Xie, S. Chen, and Y. Li, "First principles calculations of electronic and optical properties of Zr-doped La2O3," *Can J Phys*, vol. 91, no. 10, pp. 801–807, Oct. 2013, doi: 10.1139/cjp-2012-0528.
[123] N. Erum, M. A. Iqbal, S. Sagar, and F. un Nabi, "Effect of Hydrostatic pressure on structural, electronic, optical and mechanical properties of Lanthanum Oxide (La2O3)," *Phys Scr*, vol. 96, no. 11, Nov. 2021, doi: 10.1088/1402-4896/ac1474.
[124] W. Gu, Y. Song, J. Liu, and F. Wang, "Lanthanum-Based Compounds: Electronic Band-Gap-Dependent Electrocatalytic Materials for Oxygen Reduction Reaction," *Chemistry - A European Journal*, vol. 23, no. 42, pp. 10126–10132, Jul. 2017, doi: 10.1002/chem.201701136.
[125] A. Pandey, G. Jain, D. Vyas, S. Irusta, and S. Sharma, "Nonreducible, basic La2O3 to reducible, acidic La2-xSbxO3 with significant oxygen storage capacity, lower band gap, and effect on the catalytic activity," *Journal of Physical Chemistry C*, vol. 121, no. 1, pp. 481–489, Jan. 2017, doi: 10.1021/acs.jpcc.6b10821.
[126] J. Robertson, "High dielectric constant oxides," *EPJ Applied Physics*, vol. 28, no. 3. pp. 265–291, Dec. 2004. doi: 10.1051/epjap:2004206.
[127] Q. Wu *et al.*, "Interaction-Induced Self-Assembly of Au@La2O3 Core-Shell Nanoparticles on La2O2CO3 Nanorods with Enhanced Catalytic Activity and Stability for Soot Oxidation," *ACS Catal*, vol. 9, no. 4, pp. 3700–3715, Apr. 2019, doi: 10.1021/acscatal.9b00107.

[128] C. Estruch Bosch *et al.*, “Tailoring the physical and catalytic properties of lanthanum oxycarbonate nanoparticles,” *Appl Catal A Gen*, vol. 536, pp. 104–112, 2017, doi: 10.1016/j.apcata.2017.01.019.
[129] Y. H. Hou, W. C. Han, W. S. Xia, and H. L. Wan, “Structure sensitivity of La2O2CO3 catalysts in the oxidative coupling of methane,” *ACS Catal*, vol. 5, no. 3, pp. 1663–1674, Mar. 2015, doi: 10.1021/cs501733r.
[130] Y. Wu, Z. Lin, N. Chen, J. Wang, and R. Zhang, “Lanthanum oxycarbonate with nanosheet-like network structure for cataluminescence sensing of tetrahydrofuran,” *Microchemical Journal*, vol. 181, Oct. 2022, doi: 10.1016/j.microc.2022.107710.
[131] K. Lee *et al.*, “Multifunctional Interface for High-Rate and Long-Durable Garnet-Type Solid Electrolyte in Lithium Metal Batteries,” *ACS Energy Lett*, vol. 7, no. 1, pp. 381–389, 2022, doi: 10.1021/acsenergylett.1c02332.
[132] F. Du, N. Zhao, Y. Li, C. Chen, Z. Liu, and X. Guo, “All solid state lithium batteries based on lamellar garnet-type ceramic electrolytes,” *J Power Sources*, vol. 300, pp. 24–28, 2015, doi: 10.1016/j.jpowsour.2015.09.061.
[133] L. Che, Z. Huang, W. Pand, Z. Jin, Y. Li, and C.-A. Wang, “Dual interface layers for solid-state Li metal battery with low interfacial resistance and small polarization based on garnet electrolyte,” *Electrochim Acta*, vol. 330, 2020.
[134] F. Aguesse, W. Manalastas, L. Buannic, J. Miguel, G. Singh, and A. Llorde, “Investigating the Dendritic Growth during Full Cell Cycling of Garnet Electrolyte in Direct Contact with Li Metal,” 2017, doi: 10.1021/acsami.6b13925.
[135] X. He, S. Hua, F. Yan, H. Bai, B. She, and J. Zhai, “A superior stable interlayer for dendrite-free solid-state lithium metal battereis,” *Chemical Engineering Journal*, vol. 421, part, 2021.
[136] H. Duan *et al.*, “Building an Air Stable and Lithium Deposition Regulable Garnet Interface from Moderate-Temperature Conversion Chemistry,” *Angewandte Chemie - International Edition*, vol. 59, no. 29, pp. 12069–12075, 2020, doi: 10.1002/anie.202003177.
[137] J. Wen *et al.*, “A lithium-MXene composite anode with high specific capacity and low interfacial resistance for solid-state batteries,” *Energy Storage Mater*, vol. 45, pp. 934–940, 2022.
[138] H. Xu *et al.*, “Li3N-Modified Garnet Electrolyte for All-Solid-State Lithium Metal Batteries Operated at 40C,” *2Nano Letters*, vol. 18, no. 11, pp. 7414–7418, 2018.
[139] Y. Umebayashi *et al.*, “Lithium ion solvation in room-temperature ionic liquids involving bis(trifluoromethanesulfonyl) imide anion studied by Raman spectroscopy and DFT calculations,” *Journal of Physical Chemistry B*, vol. 111, no. 45, pp. 13028–13032, 2007, doi: 10.1021/jp076869m.
[140] R. S. Kühnel and A. Balducci, “Lithium ion transport and solvation in N -butyl- N -methylpyrrolidinium bis(trifluoromethanesulfonyl)imide-propylene carbonate mixtures,” *Journal of Physical Chemistry C*, vol. 118, no. 11, pp. 5742–5748, 2014, doi: 10.1021/jp5005264.
[141] L. Aguilera, S. Xiong, J. Scheers, and A. Matic, “A structural study of LiTFSI – tetraglyme mixtures : From diluted solutions to solvated ionic liquids

Tetraglyme (G4)," *J Mol Liq*, vol. 210, pp. 238–242, 2015, doi: 10.1016/j.molliq.2015.04.053.
[142] J. Lasse, J. Grondin, C. Aupetit, and P. Johansson, "Spectroscopic Identification of the Lithium Ion Transporting Species in LiTFSI-Doped Ionic Liquids," pp. 305–314, 2009, doi: 10.1021/jp806124w.
[143] A. Dumon, M. Huang, Y. Shen, and C. W. Nan, "High Li ion conductivity in strontium doped Li7La 3Zr2O12 garnet," *Solid State Ion*, vol. 243, pp. 36–41, 2013, doi: 10.1016/j.ssi.2013.04.016.
[144] J. Holtmann, M. Schäfer, A. Niemöller, M. Winter, A. Lex-Balducci, and S. Obeidi, "Boehmite-based ceramic separator for lithium-ion batteries," *J Appl Electrochem*, vol. 46, no. 1, pp. 69–76, 2016, doi: 10.1007/s10800-015-0895-z.
[145] X. Huang, "Separator technologies for lithium-ion batteries," *Journal of Solid State Electrochemistry*, vol. 15, no. 4, pp. 649–662, 2011, doi: 10.1007/s10008-010-1264-9.
[146] S. S. Zhang, "A review on the separators of liquid electrolyte Li-ion batteries," *J Power Sources*, vol. 164, no. 1, pp. 351–364, 2007, doi: 10.1016/j.jpowsour.2006.10.065.
[147] C. Roberts *et al.*, "HIGHLY POROUS CERAMIC FOAMS FROM MAGNESIUM OXIDE STABILIZED PICKERING EMULSIONS."
[148] A. G. Squires, D. W. Davies, S. Kim, D. O. Scanlon, A. Walsh, and B. J. Morgan, "Low electronic conductivity of Li7La3Zr2 O12 solid electrolytes from first principles," *Phys Rev Mater*, vol. 6, no. 8, Jul. 2022, doi: 10.1103/PhysRevMaterials.6.085401.
[149] Y. Song *et al.*, "Probing into the origin of an electronic conductivity surge in a garnet solid-state electrolyte," *J Mater Chem A Mater*, vol. 7, no. 40, pp. 22898–22902, 2019, doi: 10.1039/c9ta10269h.
[150] E. Rangasamy, J. Wolfenstine, and J. Sakamoto, "The role of Al and Li concentration on the formation of cubic garnet solid electrolyte of nominal composition Li 7La 3Zr 2O 12," *Solid State Ion*, vol. 206, pp. 28–32, Jan. 2012, doi: 10.1016/j.ssi.2011.10.022.
[151] H. Buschmann, S. Berendts, B. Mogwitz, and J. Janek, "Lithium metal electrode kinetics and ionic conductivity of the solid lithium ion conductors 'li 7La 3Zr 2O 12' and Li 7-xLa 3Zr 2-xTa xO 12 with garnet-type structure," *J Power Sources*, vol. 206, pp. 236–244, May 2012, doi: 10.1016/j.jpowsour.2012.01.094.
[152] M. Philipp *et al.*, "The Electronic Conductivity of Single Crystalline Ga-Stabilized Cubic Li7La3Zr2O12: A Technologically Relevant Parameter for All-Solid-State Batteries," *Adv Mater Interfaces*, vol. 7, no. 16, Aug. 2020, doi: 10.1002/admi.202000450.
[153] K. Shi *et al.*, "In Situ Construction of an Ultra-Stable Conductive Composite Interface for High-Voltage All-Solid-State Lithium Metal Batteries," *Angewandte Chemie - International Edition*, vol. 59, no. 29, pp. 11784–11788, Jul. 2020, doi: 10.1002/anie.202000547.
[154] X. Ping *et al.*, "Influence of sintering atmosphere on the phase, microstructure, and lithium-ion conductivity of the Al-doped Li7La3Zr2O12 solid electrolyte,"

Ceram Int, vol. 48, no. 18, pp. 25689–25695, Sep. 2022, doi: 10.1016/j.ceramint.2022.05.176.
[155] Y. Li, Z. Wang, C. Li, Y. Cao, and X. Guo, "Densification and ionic-conduction improvement of lithium garnet solid electrolytes by flowing oxygen sintering," *J Power Sources*, vol. 248, pp. 642–646, 2014, doi: 10.1016/j.jpowsour.2013.09.140.
[156] E. Ilina *et al.*, "Structural Features and the Li-Ion Diffusion Mechanism in Tantalum-Doped Li7La3Zr2O12Solid Electrolytes," *ACS Appl Energy Mater*, vol. 5, no. 3, pp. 2959–2967, Mar. 2022, doi: 10.1021/acsaem.1c03632.
[157] A. Logéat *et al.*, "From order to disorder: The structure of lithium-conducting garnets Li 7 - XLa 3Ta xZr 2 - xO 12 (x = 0-2)," *Solid State Ion*, vol. 206, pp. 33–38, Jan. 2012, doi: 10.1016/j.ssi.2011.10.023.
[158] V. Thangadurai, S. Narayanan, and D. Pinzaru, "Garnet-type solid-state fast Li ion conductors for Li batteries: Critical review," *Chemical Society Reviews*, vol. 43, no. 13. Royal Society of Chemistry, pp. 4714–4727, Jul. 07, 2014. doi: 10.1039/c4cs00020j.
[159] X. Tong, V. Thangadurai, and E. D. Wachsman, "Highly conductive Li garnets by a multielement doping strategy," *Inorg Chem*, vol. 54, no. 7, pp. 3600–3607, Apr. 2015, doi: 10.1021/acs.inorgchem.5b00184.
[160] X. Huang *et al.*, "Influence of La2Zr2O7 Additive on Densification and Li+ Conductivity for Ta-Doped Li7La3Zr2O12 Garnet," *JOM*, vol. 68, no. 10, pp. 2593–2600, Oct. 2016, doi: 10.1007/s11837-016-2065-0.
[161] J. D. Joseph, "Fatty Acid Composition of Commercial Menhaden, Brevoortia spp., Oils, 1982 and 1983."
[162] M. Rawlence *et al.*, "Effect of Gallium Substitution on Lithium-Ion Conductivity and Phase Evolution in Sputtered Li7-3 xGa x La3Zr2O12 Thin Films," *ACS Appl Mater Interfaces*, vol. 10, no. 16, pp. 13720–13728, Apr. 2018, doi: 10.1021/acsami.8b03163.